INVESTIGATION OF MATERIAL PROPERTIES OF SINTERED BLACK POINT-1 LUNAR REGOLITH SIMULANT

ADEBAYO OLUTUMBI OGUNYINKA

SpaceLab, Department of Electrical Engineering

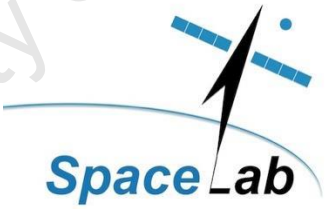

This dissertation is submitted in partial fulfilment of the requirements for the degree of Master of Philosophy in Space Studies

September 2019

SL19-010M

DECLARATION

I know the meaning of plagiarism and declare that all the work in the document, save for that which is properly acknowledged, is my own. It has not been previously submitted, in part or whole, to any university of institution for any degree, diploma, or other qualification. This dissertation has been submitted to the Turnitin module (or equivalent similarity and originality checking software) and I confirm that my supervisor has seen my report and any concerns revealed by such have been resolved with my supervisor.

Signed Signed by candidate

Date 13/09/19

ADEBAYO OLUTUMBI OGUNYINKA

Abstract

The quest for establishing a human presence and development beyond the Earth, especially on the moon has opened up opportunities for future plans for lunar bases and settlements. However, the cost of using resources outside the lunar environment can inhibit this form of expansion, therefore the need for In Situ Resource Utilization (ISRU). The aim of this research was to investigate the possible usage of in situ resources for lunar construction and other economic development.

The study evaluated different methods of material preparation using lunar regolith simulant for structural applications on the moon. The research employed the use of the regolith simulant known as Black Point-1 (BP-1). This research work presents the methodology used in developing lunar simulant and compares the properties of BP-1 regolith simulant to those of lunar soil, in terms of geotechnical and mechanical properties. Various laboratory analyses were carried out to determine these properties with the aid of thermal and analysis, particle size distribution, and XRD experiments. Our findings show that the particle size distribution and porosity of BP-1 are similar to that of the lunar regolith. The simulant was then sieved to produce four grades of powder (38 µmm, 106 µm, 212 µm and unsieved). The graded powders were then compressed to form a series of disc-shaped green compacts for sintering. The sintered samples were then subjected to compression testing. There were four different values of average compressive strength of the porosity materials ranging from lowest to highest porosity corresponding to the smallest to largest average grain sizes of 38 µm, 106 µm, unsieved and 212µm and they were 66.14MPa, 60.47MPa, 58.52MPa, 42.74 MPa, respectively. The particle size distribution was investigated on Black Point-1 simulant to determine the effect of the porosity while the bulk properties of the material were also examined for each of the four porosity grades, and this includes toughness, Poisson ratio, bulk modulus, Young's modulus of elasticity and compressive strength. When compared with other ISRU structural materials and published data for real lunar regolith it was observed that sintered BP-1 is sufficiently strong for lunar structural applications.

ACKNOWLEDGEMENTS

I would like to express the deepest appreciation to Almighty God for benevolent love and divine protection. I will like to show deep gratitude to my supervisor Professor Peter Martinez for his unflinching support and guidance during this research.

I also appreciate my wife, Rosemary, Associate Professor E.O. Falowo, Associate Prof Phil Janey, Sammy Anih, Abhijit Nath, Riddih Maharaj, Olusola Johnson and Agnes Olusola, Sunday Oladejo, Kufre Okop and my colleagues Spacelab students for their contributions. I do not forget the technical support of Mr. Jonathan in the Geosciences Laboratory.

TABLE OF CONTENTS

LIST OF FIGURES

LIST OF TABLES

LIST OF APPENDIXES

CHAPTER ONE INTRODUCTION

Since time immemorial, the Moon has occupied a prominent place in Man's view and understanding of the cosmos. Already in ancient times, the monthly cycle of the Moon's motion was well known, all based on naked-eye observations of the Moon

In 1903, the Russian rocket pioneer Konstantin Tsiokolsky published his rocket equation, which provided the basic theoretical framework for spaceflight, but at that time the technology could not achieve what was theoretically possible. Through the 1930s and 1940s, many rocket pioneers in Germany, Russia and the United States worked independently on the development of increasingly powerful rockets.

In 1950s cold war between the USA and the USSR, both superpowers developed ever more sophisticated rockets to deliver satellites into space. Following the launch of the first artificial satellite "Sputnik 1" in 1957, the Moon become a viable destination for space exploration. Not long after, the Soviets launched the space probes Luna 1 and Luna 3, which imaged the far side of the moon for the first time. To counter the spectacular achievements of the space programmes of the Soviet Union, on Sept. 12, 1962 President J.F. Kennedy of the USA pledged that his country would be land a man on the moon and return him safely to Earth before the end of the decade. Based on this pronouncement, the US sent a series of hard landers to the Moon in 1964-65. The US Ranger probes 7, 8 and 9 returned high quality images of lunar landscape. They were followed by the Surveyor missions that sent images of the lunar mare and highlands and provided data on the composition and physical properties of the Moon. The following year (1966), the USSR succeeded in safely landed the robotic explorer Lunar 9 on a mare plain. (Spudis, 2011)

The entire lunar surface was mapped out during these missions as part of the effort to find safe potential landing sites for the Apollo missions. The Apollo 11 mission became the first manned lunar landing in July 1969, where Neil Armstrong and Edwin Aldrin safely landed in Mare Tranquillitatis (Sea of Tranquillity) and brought lunar rock and soil samples back to Earth. In the three years that followed Apollo missions 12, 14, 15, 16 and 17 landed safely and collected mare basalt, emerald green glass (volcanic ash) and igneous rock samples respectively and returned them to the Earth. The Soviet Union was also pursuing a manned lunar programme, but abandoned it following the successful American landings on the Moon.

After the end of the US and Russian manned lunar programs, lunar exploration was mostly carried out from lunar orbit. Several missions continued using remote sensing to carry out the geological mapping on the Moon. Japan became the third nation to carry out a successful lunar mission. The USA Clementine and Lunar Prospector combined mission succeeded in surveying the polar region of the Moon to map minerals. In 2003 the European Space Agency (ESA) succeeded in launching a lunar orbiter SMART-1 (using a solar electric engine) to demonstrate and test innovative technologies for future deep space missions. This was followed in 2007 by the Japanese Kaguya (Selene) mission, which succeeded in mapping the Moon's gravity field.

Also, in 2007, China demonstrated their capability to carry out a deep space mission with Change's 1 to map out the Moon's topography, composition and lunar soil depth. In 2008, India demonstrated their deep space capability by using Chandrayaan-1 to detect various radioisotopes across the moon and establish a deep space radio telecommunication antenna. (Planetary Society).

In summary, approximately 382 kg of Moon rock was returned by the Apollo programme; the Soviet Union returned 300g of samples to Earth. These returned samples have great scientific value, because we know exactly where they were collected on the Moon's surface. In addition to these samples returned by the US and Soviet lunar programmes, there are many meteorites of lunar origin in museums and in private collections. These meteorites are the result of ejecta produced in bolide impacts on the surface of the Moon. We can infer their characteristic origin from the returned samples of known origin. All these samples together give us a very accurate picture of the composition of the moon.

When humans return to the Moon, it will be to stay. Moreover, the next humans to land on the Moon will do so with the benefit of half a century of unmanned and manned lunar exploration. The first human explorers had to make do with the cramped quarters of the Apollo Lunar Descent Module. While this may have been (barely) bearable for a few days at a time, it would be impractical for any missions of longer duration. Habitats will have to be built. This dissertation addresses the question of whether future astronauts might be able to turn lunar regolith (topsoil) into a structural material for building habitats and lunar infrastructure to support a permanent human presence on the Moon.

In this Chapter, we will review the milestones of human lunar exploration, past work on the potential in-situ use of lunar resources for habitat construction. We will also provide

a brief overview of the rationale for using lunar regolith simulants, and some past work in this regard.

1.1 Human exploration of the Moon

Human exploration of the Moon commenced with the landing of Apollo 11 on the Sea of Tranquillity on July 20, 1969. This was followed by five other landings, all from the Apollo programme. All told, 12 humans walked on the Moon from 1969 to 1972. In every decade since the Apollo programme ended in 1972, conceptual human missions for returning to the Moon have been proposed, but none have been carried out to date. Lunar exploration with robotic spacecraft has intermittently continued through the decades and has yielded global maps of lunar resources, including mapping of the polar regions, which are of interest for potential future human lunar settlements because of the presence of peaks of perpetual light and valleys of perpetual darkness.

The goals of lunar return are to acquire the space-derived knowledge, innovation, skill, and technologies required in moon exploration to support the new and growing spacefaring capabilities, not only for lunar settlement but also to reach other destinations in the solar system (Mars and beyond). Any sustained human presence on the moon will require the ability to extract and utilize lunar resources. Much research has focused on the collection of water ice and other volatiles collection at the polar regions, but the challenge is operating in the extreme temperature environment while preserving the sample components that are very volatile in a vacuum environment and with heat produced during drilling. The European Space Agency (ESA) is studying a lunar drill of a few centimetres in diameter for sample collection to a depth of 2 m. This drill would be designed to minimise heat and also deliver samples to scientific instruments for analysis. The Chinese and Japanese space agencies are also researching lunar drilling technology.

The Lunar polar regions would be an ideal place to establish solar power arrays for a power colony while also providing water sources and other volatiles resources

Helium-3 gas obtained from lunar regolith will serve as a fusion energy source for reactors that could sustain a lunar industrial sector for a thousand years. The light metals (titanium, beryllium, aluminium and magnesium) could be used to manufacture structural components for lunar infrastructure and for developing lunar industrial sectors (mining and manufacturing industries). Other materials, such as silica could be used for

glassmaking that would shield against the craters and micro-meteorite. The far side of the moon, shaded from all the Earth's radio signals, would be an excellent location for a radio astronomy observatory installation. In additional lunar tourism activities have been envisaged by several authors that take advantage of the lunar environment and conditions. (Peter Christoforou, 2014)

Moreover, the Moon will serve as a long-term (2030+) private investment-driven exploitation that would demonstrate technical capability and commercial potential thereby attracting privately-funded operations, which will be a vanguard to the commercialisation of the lunar and cis-lunar market (Greg Sadlier, 2016). The table below show the collection of lunar products obtained for space industrialisation and tourism during human and robotic mission.

Table 1.1 Potential lunar products for space industrialization and tourism

Source	Product	Use in Space
Mare regolith; lunar polar volatiles	Inorganic reagents (e.g. H_2SO_4)	Chemical Processing
Lunar silicon	Solar PV cells	Power system and glass fibre
Mare and highland lunar regolith Extraction.	Raw materials (Iron, and Aluminium, Magnesium, Thorium and Silicon,)	Construction of large structural platforms; Power system and glass fibre.
Recycled products; primary products	Food; manufactured goods	Earth orbit tourist facility
Regolith; ilmenite; polar ice deposits	Recovery of volatiles such as Propellant; H_2, O_2 for life support	Space transportation, station-keeping for orbital assets; life support consumables; energy storage (e.g. fuel cell reactants)
Lunar polar volatiles; recycled space industrial wastes	Organic constituents (e.g. plastics)	Manufactured parts for use in space
Lunar Regolith	Interlock paves, bricks and block	Road construction and structural habitat
Mare regolith; lunar polar volatiles	Inorganic reagents (e.g. H_2SO_4)	Chemical Processing

Lunar silicon	Solar PV cells	Power system and glass fibre

The robotic mission mapped out the entire moon with a high-resolution picture, shown the features of craters and its Copernicus, boulder, lunar regolith, potential landing site that certified the safety of all the lunar missions. About 382kg of genesis (rock) and lunar soil were brought by Astronaut during the Apollo Missions. But to mention a few, the overview of the outcome of the robotic mission were shown in the table below.

Table 1.2 The outcome of robotic Mission.

The outcome of robotic mission	
Luna 3 (1959)	Moon Far side highlands- Magmas, silicate minerals, potassium (K), rare Earth elements (REE), and phosphorus (P), scandium and yttrium and lanthanides.
Ranger 7 (1964)	Mare Nubium.
Surveyor (1,2,3,4 and 5) 1966-1967	lunar surface that showed the dark Mara enriched in iron, and a highland richer in aluminium minerals composition
Apollo 11 (1969)	High-Titanium basalts, Extrapolation data on Mare Tranquillitatis Helium-3, Hydrogen (Solar wind)
Apollo 12 (1969)	low-Titanium basalts
Apollo 16 (1972)	Lunar highland: minerals Silicon, Iron, Oxygen Magnesium, Calcium and Titanium, Thorium and uranium
SMART-1 (2003)	Orbit the Moon and carried out the geological mapping, while the pyroxene and olivine minerals were taken.
Japan-Selene	Mapped the gravity of the far side of the Moon, shown the shadow of internal crater and also shown The nearside lowlands, where nearside features such as large area of low-Ca pyroxene on the nearside observed by
Chang'e-1 Mission (2007)	Geological structures e.g. minerals elements mapping and Helium-3
Chandrayaan-1 Mission (NASA's Moon Mineralogy Mapper-2008)	Lunar-nearside-water discovered (b) Lunar magnetic anomalies at Southerner and Northerner hemisphere were also shown.

Grail Mission (NASA's Gravity Recovery and Interior Laboratory mission) employed the Lunar Reconnaissance Orbiter Camera (LRO) to show the mineralogy composition of the Moon- olivine, pyroxene., anorthositic, plagioclase, and ilmenite that dominate the region of lunar highlands and Mare basalts.

1.2 Use of in-situ resources for building lunar habitats and infrastructure

Any sustained human presence on the moon will lead to the need to build structures for human habitation and other purposes. To build a habitable structure constructed on the lunar surface, one must be able to draw on construction materials that are locally sourced. These materials must be workable in the lunar environment to produce structural elements with material properties that are up to the task. Such properties include durability, low coefficient of thermal expansion, and high tensile and compressive strength. These structural elements (bricks, columns, shells, slabs, paving blocks, tiles, arch segments, and beams blocks) would most likely be manufactured from lunar regolith.

The fabrication of bricks will allow speedy construction of habitats, laboratories and industrial facilities on the lunar surface. Glass made from the melt of regolith could be used to produce structural components because of its extreme strength (even stronger than alloy steel) and durability. (Spudis, 2011). The ability to produce durable tiles and interlocking pavers stones would enable astronauts to construct smooth surfaces like roads, pathways and parking areas and landing pads that would improve traction for fast-moving wheeled vehicles and minimize the amount of lunar dust generated from human and vehicular motions and rocket take-offs/landings near a lunar habitat. (Ruess, Schaenzlin and Benaroya, 2006)

1.3 Past work in the field lunar ISRU

Many researchers have addressed the challenge of lunar ISRU for infrastructure development from several angles. These works fall into two broad categories, namely attempts to produce lunar concretes, attempts to sinter regolith, and attempts to use regolith in sintering and additive manufacturing (3D printing) applications. We will provide a brief overview of work done in each of these categories.

1.3.1 Lunar concretes

On Earth, concrete is a widely used construction material because of its high compressive and moderate tensile strength when reinforced and its capability to withstand extreme environments. Various investigations have been made of the potential to utilize lunar regolith to produce concrete for building purposes, as well as sintered regolith for manufacturing of structural components. These materials can be used in support of ISRU as an alternative to building an infrastructural habitat in the Moon.

Water has been used as a liquid reagent for producing concrete on Earth, but in a vacuum environment water evaporates rapidly unless the concrete sets in a pressurised environment (Wilhelm and Curbach, 2014). Therefore, the ability to cast concrete without using water would be the preferred solution for a structural component on the lunar surface.

(Grugel and Toutanji, 2008) conducted an experiment on sulphur-based concrete for a lunar application, based on the availability of the sulphur substance in the form of mineral troilite (FeS) on the moon. The sulphur concrete sample was prepared from JSC-1 lunar regolith simulant mixed with SiO_2 powder (aggregate). When tested it was observed to have a high compressive strength, but due to the phase transformation of sulphur and effect of pressure and temperature this has led to loss of binder and crack formation on the concrete surface. Thus, it could not proffer a solution to vacuum and temperature differentials on the moon.

(Davis, Montes and Eklund, 2017) experimented with the geopolymer concretes, where alumina-silicate was mixed with alkali ions, to form geopolymer structures based on the silicon-Aluminium ratio of the content. A high compressive strength and a fine grain microstructure were obtained. However, when the geopolymer structure was exposed to vacuum and a high-temperature environment, the materials lost its compressive strength, and this restricted its application for lunar structures.

(Wilhelm and Curbach, 2014) investigated using Calcium Oxide (from anorthositic rock) to produce a reinforced lunar concrete. However, exposure to a vacuum environment led to extensive water loss and a highly porous sample with limited applicability in practice.

(Benaroya, Bernold and Chua, 2002) proposed to use cast basalt (abundant in the Mare) for a prefabricated construction component (arch segments, blocks, shells, columns,

slabs and beams) due to its high comprehensive and moderate tensile strength which is more than that of terrestrial concrete, however, the brittleness of this material has limited its application.

To summarize, the various experiments with candidate lunar concrete materials have all shown that the sublimation and evaporation of the binder have limited the utility of concrete on the lunar surface. Moreover, additional forming work with sealants to produce prefabricated concrete samples have also increased the cost of manufacturing components out of these lunar concretes.

1.3.2 Sintering and additive manufacturing techniques

Several methods have been employed in manufacturing process of different structural components such as microwave sintering, additive technology of 3D printing but here a sintering method was applied to sinter the structural materials where heat was used to transform the lunar regolith materials into solid structures However, the structural member produced through this sintering process have been hampered due to the effect of porosity thereby reducing the strength and rendering it incapable for fully utilisation.

(Meurisse *et al.*, 2018) investigated on the concept of using ISRU in structural building was carried where a 3D technology was used to print the bricks and interlocking elements using sunlight to fuse the grains of regolith (Fateri, Meurisse and Sperl, 2017) more so, the presence of low gravity and vacuum environment was suitable for this process. Hence, it can be applied to produce a fiberglass and tools parts (Avchare *et al.*, 2014). All these are sustainable manufacturing methods for space engineers. They are very easy and highly scalable.

The diagram below shows the tools and block made from 3D printing with lunar and Martian dust.

Figure 1.1 Successful 3d printing activities in Aachen using a lunar and Martian regolith simulants (Morris A, 2017).

The figure 1.1 above show the tools and block made from 3D printing with lunar and Martian dust. This activity was carried out by an additive manufacturing expert (Aachen) which employed the locally sources materials (ISRU) to construct and maintain the extra-terrestrial outpost. The technology has provided a breakthrough tremendously for high quality, strength and costs effective of structural materials for space explorers.

(Cole D.M., Taylor L.A., 2010) conducted a series of experiments on regolith simulant NU-LHT and lunar highlands plagioclase grains where the size, shape and surface morphology were characterized, and mechanical testing was carried out to evaluate the normal and shear contact behaviour. It was observed that the regolith simulant NU-LHT were free from microstructural flaws and there was variation between the shear's properties of lunar highland plagioclase and simulant.

1.4. Regolith Simulants for Investigating ISRU

Because of the limited quantity of lunar regolith returned from all lunar sample return missions is less than 400 kg, and these samples are very valuable to scientists, the lunar ISRU community must make do with several terrestrial regolith simulants sourced from

a variety of locations worldwide. The simulants have a variety of different geophysical properties, and the right simulant must be used for each application.

Various types of these simulants are being produced worldwide. Therefore, standardisation becomes necessary in the engineering environment to limit and avoid the failure of system design due to the wrong choice of the regolith simulant. The use of regolith simulants has helped scientists and researchers in the assessment of the performance of current technology, choice of designs for failure risk reduction. However, no lunar simulant will mimic real lunar soil due to the difference of geological formation and environmental differences between the surface of the Earth and the surface of the Moon. For example, the absence of nanophase iron in simulants is a significant difference for certain investigations, including sintering. Thus, any engineer or scientist must have a comprehensive knowledge of existing and current lunar geological research, as well as the geophysical properties of regolith simulants to understand how the differences between them would interact with a given set of experimental conditions.

1.5 Past work by others with simulants and ISRU

A few groups have used regolith simulants from a wide variety of applications, ranging from development of wheeled vehicles to the production of glasses and photodiodes. In this brief review, we will highlight just some of the more recent works.

(Indyk and Benaroya, 2017) quantified the material properties of unrefined sintered JSC-1A simulant for low and high porosity of 1.44% and 11.78% samples. They compared the mechanical properties of these two porous grades and the low porosity of 1.44% was recommended for lunar structural material applications. (Faierson *et al.*, 2010),investigated the design of a Voussoir dome through the geothermite reaction processes, where a mixture of JSC1A, JSC 1AF and Aluminium powder was used for structural fabrication. (Mpagazehe *et al.*, 2014)conducted an experimental study on JSC 1AF simulant to determine the potential effect of erosive lunar dust. The result showed a decrease in direct transmittance and total reflectance of optical components. Hence it was concluded that lenses and mirrors are susceptible to damage during lunar landing due to lunar dust particle impingement. (Zheng *et al.*, 2009)considered CAS-1 regolith simulant as a replicate of the Apollo 14 samples having investigated its geotechnical properties. They also performed mechanical and thermal analysis and concluded that CAS-1 is a suitable simulant to use for planning a future Chinese lunar landing mission.,

(Reis, 2014) processed JSC 1 simulant with the aim of extracting metals and developing a glass for fixing nuclear waste on planetary bodies.

1.6 Research Motivation

In recent years, a few space agencies and space companies have presented plans for human exploration of the Moon. The viability of future for lunar development depends on in-situ resource utilization (ISRU), not only for construction of infrastructure but also for energy generation and minerals exploration, thereby complementing and expanding the economic sphere of humans beyond the surface of planet Earth. Cost is being a controlling factor of evaluating the choice of materials in many applications either by weighing what it takes in conveying the prefabricated structural component to the moon or using a derived material of ISRU onsite for building a lunar habitat. Therefore, it is important to assess the viability of using lunar resources for various structural material purposes, beyond just simply piling up lunar regolith into mounds, but rather assessing its potential as source material for manufactured structural elements.

One of the methods of manufacturing these structural components onsite is by employing the sintering process that can impart strength and integrity into loose regolith particles to produced construction bricks, blocks, and other shapes. However, the major problem encountered during this process is the prevalence of defects (porosity and cracks) that have an adverse effect on the mechanical performance of structural components and their reliability during the service condition. Therefore, this study will evaluate various methods of material preparation using lunar regolith simulant for structural building on the Moon.

1.7 Research Goals

The goal of this dissertation is to investigate the feasibility of applying sintering methods to regolith as a way of processing it to produce structural elements, such as bricks, poles and tiles etc. Because of the very limited quantities of regolith available for research, we will use a regolith simulant called Black Point – 1 (BP-1), which has geotechnical properties similar to that of lunar regolith. The investigation carried out in this research will determine the viability and reliability of ISRU structural materials in the lunar surface.

BP-1 has geotechnical properties similar to other lunar simulants such as MLS-1, (Minnesota lunar simulant 1), JSC-1, JSC-1A (Johnson Space Centre 1), GRC-3 (Glenn

Research Centre 3), NU-LHT-2M and Chenobi. BP-1 has a broad particles size distribution with a relatively high fraction of fine grains and coarse particles and when compared with other simulants.

The specific gravity of BP-1 lies within the range of 2.45-2.80, which is lower than lunar regolith (2.90-3.25) and other simulants, except that of GRC-3(2.63) (Eduardo et al 2014). It is very reactive, both with acid (HCl) and an oxidising agent (fluorine, boron trifluoride). It has a granular white colour, light grey and reddish odourless particles ranging in different size from powder to boulders.

Its particle size distribution is within the range of $\pm$1 standard deviation of lunar regolith and the stiffness slightly increases with an increase in relative density (Zeng et al., 2010).

In terms of handling, the usual precautions should be taken when handling fine powers. Human exposure to BP-1 simulant can affect the respiratory organs and this can cause acute silicosis. Similar measures of precaution should be applied to handling lunar regolith dust.

1.8 Scope of this dissertation

The scope of the work presented in this dissertation will entail the use of the regolith simulant known as Black Point-1 (BP-1), the sintering process of transforming the compact regolith simulant, conducting the experiments in a vacuum furnace, investigating the various material properties of sintered BP-1 with the aid of mechanical and thermal analysis, evaluating the achieved properties, and devising strategies to mitigate defects and improve performance. Based on our findings, we will be able to prescribe recommendations for the best use of regolith in developing a permanent lunar base and overcoming the environmental challenges.

1.9. Structure of the Dissertation

The remainder of this dissertation is structured as follows:

Chapter 2 provides an extensive literature review on the geotechnical properties of lunar soil and lunar soil simulants.

Chapter 3 gives comprehensive details of the sintering process, the factors to be considered in sintering, and the process of sintering in the lunar surface. It also describes the materials tests to be performed on lunar regolith simulant BP-1 samples.

Chapter 4 provides a detailed description of BP-1 simulant and its geotechnical characterization, and uniqueness and compares its geotechnical properties to those of other simulants and lunar soil. The chapter also describes the design of the experiment and sample preparation procedures.

Chapter 5 presents the test results from the mechanical and thermal analysis.

Chapter 6 provides general conclusions and recommendations for further work.

CHAPTER TWO LUNAR REGOLITH AND REGOLITH SIMULANT

In this chapter we will discuss the formation and properties of lunar regolith, and then we will discuss the various regolith simulants that are available for research applications.

2.1. Lunar Regolith Formation and Properties

In this chapter, the formation and properties of lunar regolith and regolith simulants for research applications will be discussed.

Lunar regolith consists of layers fragmented rock that overlays the Moon's surface. It is produced as a result of countless impacts of a meteoroids/micrometeoroids, asteroids and constant bombardment of highly energetic solar particles over billions of years. All of these processes have given rise to the formation of regolith grain particles. The combined effects of heat, pressure, atomic particle bombardment, lava eruptions and meteor impacts constituted the formation of lunar regolith. Fig 2.1 illustrates the physical processes involved in the formation of lunar regolith. Regolith particles include agglutinate glasses, crystalline rock and breccia fragments. The depth of the regolith varies from ~5m in the mare regions to ~10m in the highland regions.

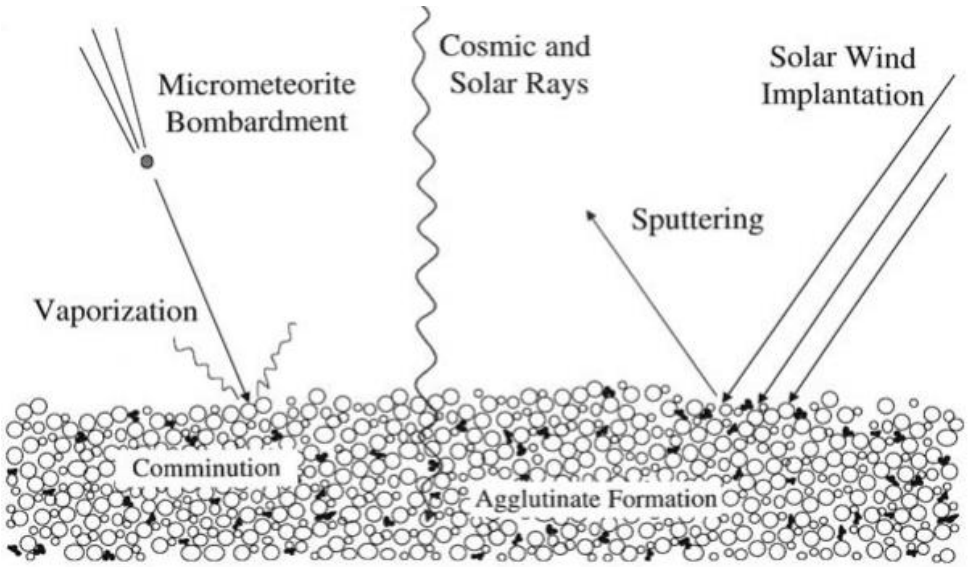

Figure 2.1 Impacts and formation of lunar regolith: Adapted from Michael Küppers et al., (2011)

The formation and evolution of the lunar regolith occurred during the constant bombardment of micrometeorites on the lunar surface, forming a loosed fragmentation of materials. The larger impacts have more penetrating power and lead to excavation of the fresh bedrock (exposed) that forms agglutinates and glasses, while the constant solar

wind implants a large quantity of hydrogen, helium and trace elements in the surface layers of regolith. Natural degradation of the surface rocks due to huge temperature differences between day and night has also contributed to the formation of the lunar regolith. The composition and texture of regolith varies from the Maria to the Highland regions, while the bulk density consisted of fine grains soil.

Unlike terrestrial surfaces, lunar regolith does not experience natural weathering since there is no water and atmosphere on the Moon. Therefore, regolith particles have a rough, irregular agglutinate shape and the accumulation of this increased as more impacts occurred while the small impacts caused the agitation and comminution of the surface layers, leading to the increase in regolith thickness with time (Küppers and Vincent, 2011).

2.1.1 Regolith Composition

The impact crating, tectonism and volcanism are the geological processes of the Moon and it is through these medium that the rocks were formed on the Mare and highland surface however, on conducting the chemical analysis on the rock's minerals, the temperature and pressures at which they formed would be determined while the gases and chemical elements present in the lava or molten magma would be identified (depends on the depth and location). Therefore, the lunar Maria consist of minerals such as silicate, ilmenites, pyroxene, olivine, anorthite and titanium element, while the Highlands consist of anorthite with high percentage of plagioclase. During the regolith formation, many volatiles gases such as hydrogen, oxygen, nitrogen, carbon, sulphur, chlorine, and fluorine were produced. The Moon has a distinctive characteristic which differs from the Earth. It has no water-based minerals structures like clay and mica. Also, it is chemically reduced rather than being oxidised and this is due to constant bombardment of impact with energetic protons from the solar wind as well as iron nuclei that combine with oxygen to form nanophase iron oxide particles Fe^{0} and Fe^{2+} oxide.

2.1.2 Uniqueness lunar regolith - nanophase Fe^{0}

Lunar regolith contains nanophase iron, which is formed in reduction reactions in impact melts, where the iron (II) oxide reacts with high energy particle of H^{2+} from solar wind leading to the formation of nanophase iron and water. The presence of nanophase particles of Fe^{0} in lunar regolith is a characteristic that distinguishes it from terrestrial

regolith simulants. The presence of nanoparticles is a direct function of surface area and they more evident in the finest grain sizes (<10μm). As the grain size of regolith particles increases, the percentage of nanophase iron in the regolith reduces greatly. The presence of nanoparticles makes the regolith to be an agglutinitic glass and have magnetic susceptibility. It also affects the spectral reflectance and other the optical properties of regolith (Taylor *et al.*, 2001).

2.2 Regolith Simulants

The use of regolith simulant is essential for scientific research in space exploration because the cost of using a real lunar regolith is quite expensive and unaffordable. In order to achieve a successful and safe extended mission and establish a lunar outpost, the knowledge and understanding of the lunar environment, geological formation and mechanical properties of regolith in the lunar surface is paramount, and the more comprehensive our understanding of the properties and behaviour of lunar regolith, the more effective and economical we can be in our designs. Furthermore, with an expectation of returning to the Moon, a number of regolith simulants have been developed worldwide for various research applications, where these simulants have served as a test bed for laboratory studies that need to simulate the conditions that may likely be encountered on the lunar surface. With the advent of a large number of regolith simulants, each with its particular characteristics, has it has become necessary for standardisation in an engineering environment, to limit and avoid design system failure due to the wrong choice of the regolith simulant.

Table 2.1 List of lunar regolith simulants.

Simulant name	Type	Information
GCA-1	Low-Ti mare (geotechnical)	Goddard Space Centre
CSM-CL	Geotechnical	Colorado School of Mines - Colorado Lava. Unpublished

DNA-1	Low-Ti mare (general use), similar to JSC-1, higher MgO content.	
BP-1	Low-Ti mare (geotechnical).	1KSC/ Arizona Black point quarry waste (basalt); used for large excavation exercises with BLADE. Rahmatian.
ALS	Low-Ti mare (geotechnical)	Arizonal Lunar Simulant
GRC-1 & GRC-3	Geotechnical: Standard vehicle mobility Lunar simulant	Glenn Research Centre (Sandy, clay mixture used in SLOPE Facility for mobility/ excavation.
GSC-1		Goddard 'simulant"; material from local site that is being used for drilling testing
JSC-1	Low-Ti mare (general use).	Johnson Space Centre.
JSC-1A, JSC-1AF, JSC-1C	Low-Ti mare (general use). Produced from the same source material as JSC-	Orbitec created under a NASA contract.
MKS-1	Low-Ti mare (intended use unknown)	

MLS-1*	High-Ilmenite mare (general use)	Minnesota Lunar Simulant
MLS-1P	High-Ti mare (experimental, not produced in bulk although small quantities were distributed	Minnesota Lunar Simulant
MLS-2	Highlands (general use)	Minnesota Lunar Simulant
NU-LHT-1M, NU-LHT-2M, NU-LHT-1D, NU-LHT-2C	Highlands (general use)	NASA/USGS. Highland type simulant (chemical/Mineralogical & physical properties)
CAS-1	Low-Ti mare (general use)	China (Chinese Academy of Sciences) a basic simulant made to represent Apollo 14
CLRS-1	Low-Ti mare (general use).	Chinese Lunar Regolith Simulant. Chinese Academy of Sciences (2009)
CUG-1	Low-Ti mare (geotechnical)	China
CLRS-2	Low-Ti mare (general use).	Chinese Academy of Sciences (2009).

NAO-1	Highlands (general use).	National Astronomical Observatories, Chinese Academy of Sciences.
TJ-1, TJ-2	Low-Ti mare (geotechnical	China (Torgji University); a basaltic ash feedstock with olivine and glass
OB-1	Highlands (general use geotechnical)	Canada, Olivine-Bytownite.
FJS-1 (type 1), FJS-1 (type 2), FJS-1 (type 3),	Low-Ti Mare, Low-Ti Mare, High-Ti Mare, (general use)	Fuji Japanese Simulant.
Oshima base simulant	High-Ti mare (general use)	Syeyoshi
KOHLS-1	Low-Ti mare (geotechnical	Korea. Koh Lunar simulant.
CHENOBI	Highlands (geotechnical)	Canada (physical a& chemical properties simulant)
Kohyama base simulant	Intermediate between highlands and mare (general use).	

Adapted from(Sibille, 2013)

https://ntrs.nasa.gov/archive/nasa/casi.ntrs.nasa.gov/20130011598.pdf

Table 2.2 Types of Simulants and Minerals Compositions.

Minerals composition	**Simulant**					**Apollo sample 14**
Oxide	JSC-1	CAS-1	FJS-1	MKS-1	BP-1	Avg. Soil
SiO_2	47.71	49.24	49.14	52.69	47.2	48.1
TIO_2	1.59	1.91	1.91	1.01	2.3	1.70
Al_2O_3	15.02	15.80	16.23	15.91	16.7	17.4
Cr_2O_3	0.04	-	-	-	-	0.23
Fe_2O_3	3.44	-	-	-	5.9	-
FeO	7.35	11.47	13.07	12.28	6.2	10.4
MnO	0.18	0.14	0.19	0.22	0.21	0.14
MgO	9.01	8.72	3.84	5.41	6.5	9.4
CaO	10.42	7.25	9.13	9.36	9.2	10.7
Na_2O	2.70	3.08	2.75	1.9	3.5	0.7
K_2O	0.82	1.03	1.01	0.58	1.1	0.55
P_2O_5	0.66	0.3	0.44	0.14	0.52	0.51
CO_2	-	-	-	-	0.05	-
H_2O^+	-	-	-	-	0.41	-
H_2O^-	-	-	-	-	0.11	-
LOI	0.71	0.52	0.43	0.5	-	-
Total	99.65	99.46	98.14	100	99.90	99.8

Adapted from(Zheng *et al.*, 2009) (Stoeser, Wilson and Rickman, 2010)

2.3. Evaluations of lunar regolith simulants

Over the years. many lunar simulants of different types have been created for various research applications. (Indyk and Benaroya, 2017) investigated the material properties of sintered JSC-1A simulant. They determine the compressive strength which, when

compared with lunar regolith and terrestrial concrete, was found to be excellent. They concluded that this material could be used to produce structural elements (slabs, bricks and beams) for a lunar outpost.

(Cardiff and Hall, 2008) employed a Fresnel lens as a solar concentrator to sinter the JSC-1A / JSC-1AF lunar regolith simulant into a melt, thereby creating a hard, dust-free surface. In their experiments they observed that the Fresnel lens sintered the simulant at a maximum rate of ~13cm^2/min, 2.5cm maximum depth, under a low vacuum environment. These sintering experiments were carried out in the Earth's atmosphere, but the process will perform excellently in the exosphere where the solar intensity will be greater, and this method can be employed in additive technology for 3D printing of structural elements (paving stone, and edge-butting or interlocking tiles) or for building the structure of a habitat.

(Oravec, Zeng and Asnani, 2010) investigated GRC-1 (Glenn Research Centre-1) simulant to carry out an assessment for the tractive performance of lunar vehicles in exosphere and this was done to confirm penetration measurements acquired during the Apollo missions. Admittedly the test was neither a full representation of lunar terrain nor, did it replicate the mineralogical composition, but the GRC-1 simulant was developed specifically for geotechnical, and engineering applications.

(Jiang, Li and Yang, 2013) examined the deformation behaviour of lunar soil was examined where a Tongji-1 (TJ-1) regolith simulant was subjected to principal stress rotation of a hollow cylindrical apparatus model and the result produced a homogeneous sample of a wide grain distribution of simulant. This study became necessary in determining the bending moment of retaining wall so as to avoid unsafe design of structural foundation of a lunar outpost as well as provide a safe landing for astronauts.

2.4. Suitability of simulants for researching potential lunar construction techniques

The physical and mechanical properties of BP-1simulants have been investigated by many researchers, such as. (Suescun-Florez *et al.*, 2015)(Sibille *et al.*, 2006); and (Laila A. Rahmatian1, 2 and Philip T. Metzger and 1School, 2010). These properties are important because of their influence on the stability of engineering structures being constructed on the lunar surface as well as the installation of any equipment. BP-1 was found to have similar properties to other simulants such as JSC-1A, NU-LHT-1M OB-1, FJS-1 MLS-1and CHENOBI, and it has superior performance for both mechanical

and geotechnical applications.(Stoeser, Wilson and Rickman, 2010) examined the mineralogy, chemical composition and particles size distribution of BP-1 using X-ray diffraction analysis to determine the mineral content for exploration. The broad particle distribution of BP-1 is relatively high in the number of fine grains and coarse particles and this makes BP-1 exceptionally applicable for structural habitat. (Mueller *et al.*, 2018) advocated for employing the use of BP-1 for the construction of hollow cone and Ogive dome structures.

However, the thermal analysis behaviour of BP-1 simulant subjected to high temperature during the construction of structural facilities has not yet been investigating and such information will be very useful when carrying out heat exchange, thermal control and sintering processes.

CHAPTER THREE SINTERING PROCESS CONSIDERATIONS

Any use of regolith for lunar habitat construction will require material processing of some form or another. In this chapter we discuss the relevant processes, ranging from simple compaction to sintering. This provides a theoretical basis for interpreting some of the test results that we will present in Chapter 5.

3.1. Compaction

Particles size affect many properties of lunar regolith and is a valuable indicator of quality and performance. It helps in determine the surface finishing (appearance) of lunar structures as well as the strength of lunar concrete, the size and shape distribution of a glass bead (from lunar regolith) impacts the reflectivity while the particle size distribution of a metals influence the powder behaviour during the compaction and sintering.

Therefore, lunar regolith can be incorporated in construction processes in a variety of ways, ranging from simply bulldozing mounds of regolith to cover thin-walled structures, or compaction, for forming lunar concretes or for producing sintered structural components, which is the focus of this dissertation.

Any structural components (slabs, columns, tiles, and beams) prepared from this material must be designed to meet the performance requirements of the structure into which it is planned to be incorporated, under lunar loading conditions, which in turn depends on the bulk material properties. The strength and stability of any structure and its individual elements made of regolith would only be guaranteed when it withstands the environmental forces. For this to occur, adequate soil compaction and consolidation must take place so as to improve the load bearing capacity of the soil (Kodikara, 2019). Compaction is necessary because it increases the densification of the material, reduces void ratio and porosity, and also increases the stiffness and load bearing capacity of the un-sintered “green” compact, thereby establishing its suitability for construction applications.

Furthermore, during the compaction process, the loose soil particles stick together due to the cohesion force that exist among the grains (*Soil Compaction Theory Compaction*, 2018). Compaction can be employed to improve the soil strength where the soil grains are closely packed thus increasing the shear strength and at the same time reduce the soil

compressibility, permeability and soil settlement which can have an adverse effect on structural stability.

Compaction will only provide adequate strength to sustain the shape of the component during the sintering process. It is the sintering process that leads to the increase in strength. The physical process of sintering that brings about this significant increase in strength is discussed in Section. 3,2 below.

3.1.1 Compaction-induced defects

Defects can develop during the compaction process and usually create a weak zone after sintering, which is undesirable. These defects can be characterised as voids and cracks. Both affect the material strength and quality of the sintered products.

Voids

When compaction takes place in an atmosphere, voids occur after filling of powder into the compression mould due to air entrapment. Adequate soil consolidation (such as sieving) and sintering will reduce the effect of voids.

Cracks

Cracks in the compacted green body become noticeable during handling and is usually occur when stress is built up in the compact while it is in the mould, and then released when the compact is removed from the mould. End-capping is a crack defect that occurs from the top or bottom edge of the compact to the centre. This can cause material on the edge of the front or rear face to break off, either shortly after the green compact is removed from the mould, or subsequently during sintering. Die friction also alters the density gradient leading to slippage failure (powder failure stress) in a green compact.

3.2 Physics of Sintering

Sintering is a manufacturing process employed for fabrication of structural components. In essence, it is thermal treatment that is employed to bond the mineral particles together into a solid structure. Many articles and products have been developed through this process, ranging from dinnerware to automotive structural parts (German, 2013). The oldest evidence of sintering of ceramics dates back to the Stone Age, for making tools. Sintering usually takes place below the melting point of the material being worked. When compared with melting processes, sintering gives a high dimensional precision to structural components and less wastage. Sintering produces a homogeneous

microstructure in the three-dimensions with isotropic bulk properties and an excellent surface finish.

During the sintering process, each mineral particle is thermally activated and transforms into a stable and thermal equilibrium state, thus forming a bonded (cohesive) solid structure with neighbouring particles (Introduction and Olevsky, 2011). At a certain stage during the sintering cycle, the system energy reduces while the solid structure increases in strength. The geometric shapes of pores that form between the particle's changes in size. As the temperature increases the sample become densified and subsequently shrinks. When this occurs a reduction in surface energy takes place at the grain boundary, while diffusion develops at the contact area between adjacent particles. When the sintering occurs, the free energy becomes lower (driving force) at the curvature of the particle surfaces due to the externally applied force and the chemical reaction that has taken place.

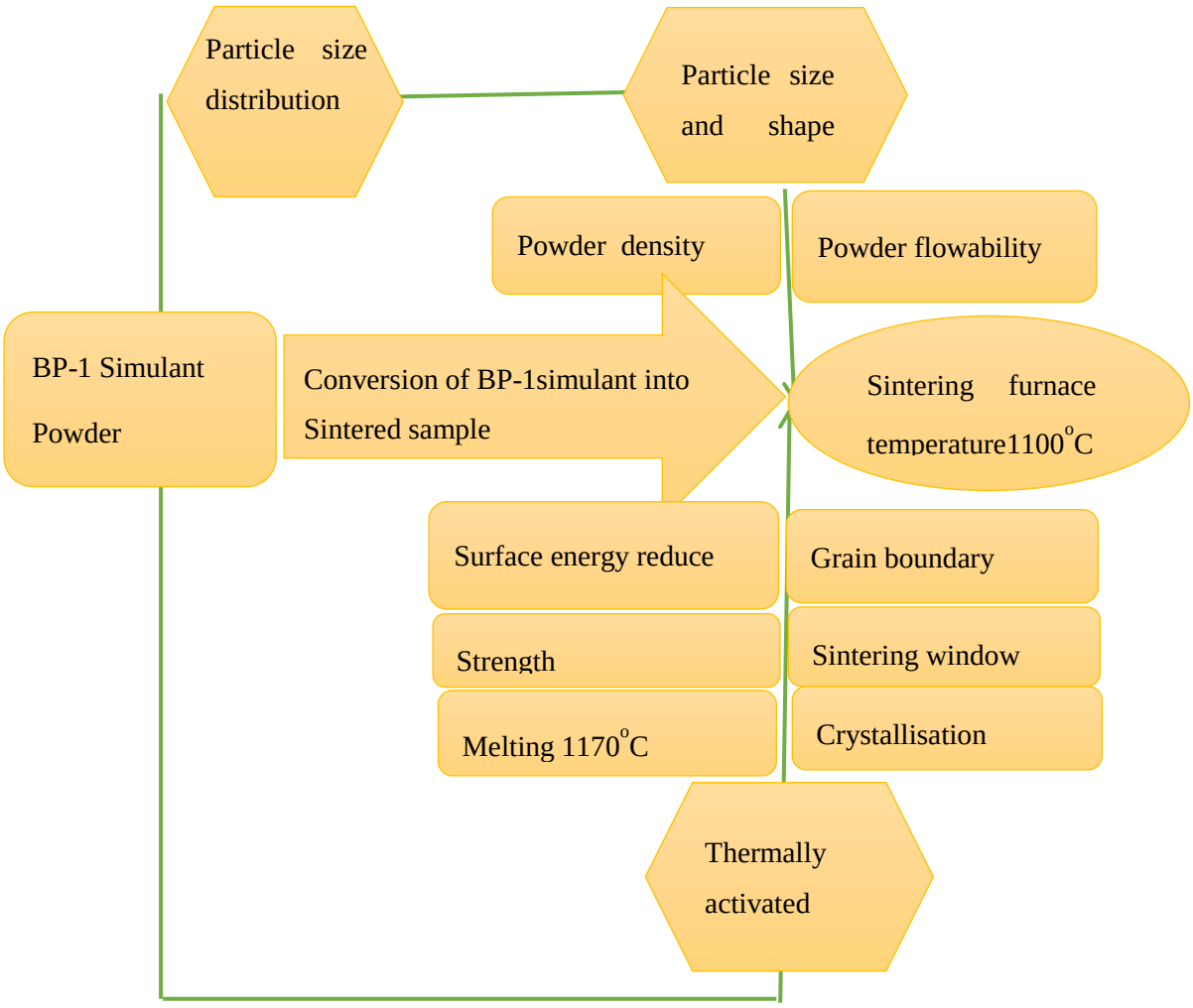

Figure 3.1 Critical properties for a BP-1 simulant during furnace sintering at a temperature 1100ºC

The number of pores and their size will reduce causing the sample to shrink due to a reduction in the total surface area. The sintering process produces a homogeneous microstructure, with a high purity. This sintering process produces a sample of controlled and uniform porosity with homogeneous and isotropic properties and requires much less energy than forming the same material by melting it (Derlet, 2017). Also, sintering equipment is typically less bulky and requires less space than casting equipment. Both attributes make sintering very advantageous for lunar applications compared with casting.

3.3 Types of Sintering

Solid state sintering:

The solid phase of the compact sample present at the sintering temperature will remain in the solid state (powdery form). At this point, the particle shapes begin to change, the particles rearrange, and the adjacent particles diffuse to form a neck region. This leads to a reduction in surface area and increase in strength of the samples. The particles remain bonded together while the porosity decreases until the pores are finally closed. In other words, in solid state sintering, the powder remains in a solid state while it is densified at the sintering temperature.

Liquid phase sintering:

In contrast to solid-state sintering, liquid phase sintering occurs when the liquid phase is present in the powder compact during sintering. Liquid phase sintering is applicable to refractory metals (tungsten carbide, silicon carbide) and this occurs in three stages namely; rearrangement, solution-precipitation and final densification. The initial stage begins with the formation of a liquid phase that followed by solubility process, which provides the capillary force required to pull the solid grain together before a final stage occurs where the solution-precipitation was formed until the particles diffuse and become densified at the grain boundary (Johnson, 2010).

Viscous sintering

Viscous sintering occurs at the interface between the liquid phase and solid-state sintering; the liquid forms of the early stage of the sintering will later disappear as the sintering proceeds until densification of a solid structure is formed.

Sintering processes undergo various stages, ranging from rearrangement and repacking of particles, initial stage growth, intermediate and final stage. The particles in the green

body will rearrange themselves in a way such that they have a body contact with each other in a random orientation until an initial stage has taken place, where the inter-particle contact increases with density until the neck and grain boundary forms with a smooth surface. The intermediate begins as the temperature increases. Particle bonding increases with density while the porosity along the grain boundary reduces. The final stage appears as the temperatures reduce gradually while grain growth becomes elongated along the grain boundary until the pores become closed.

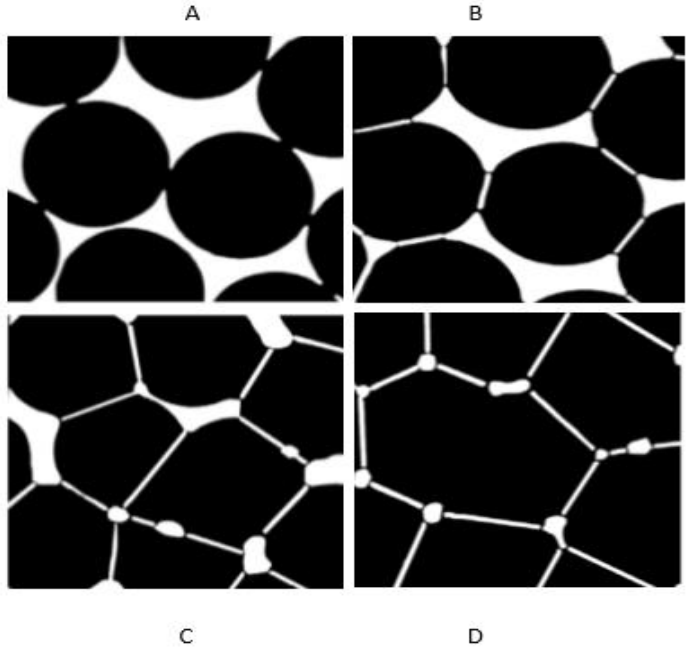

Figure 3.2 The various phases of the sintering process: (a) rearrangement and repacking of grains particle bond growth (b) initial stage growth (c) Intermediate (d) final stage.

3.4. Factors to consider during the sintering process.

There are many factors that affect the sintering process - the quality of the sintered product, sintering time, temperature, the furnace atmosphere and the particle size distribution.

The quality of the sample influences the process of sintering to a great extent. Particle size is also important. An increase in the mean size of the particles of simulant will promote greater productivity of the sintering machine and save energy consumption, but the strength of the sintered product reduces. On the other hand, an excessively fine grain size will reduce the granulation efficiency, thus decreasing the permeability and consequently lowering the production rate of sintered components.

The percentage of mineral content (silica/alumina) also affects the sintered product, therefore, these constituents must be kept to a minimum level. The particles size distribution has a great effect on sintered permeability and subsequently affects the sintering process.

The sintering time is dependent on the manufacturing process and materials. For example, refractory materials would require longer time to be sintered because of their high melting temperature properties. The holding time of the sintering process will depend on the temperature required, porosity, pore shapes and stress resistance or pressure (convectional sintering). A key consideration is to minimise the shrinkage as the porous body (Satyendra, 2013). Sintering processes carried out at a high temperature can cause a decrease in bed permeability, which might affect the mechanical properties of a sintered product.

The furnace atmosphere also has a great influence on the sintering. A controlled inert atmosphere such as argon or nitrogen will prevent oxidation, surface diffusion, and the unwanted chemical reactions that might occur during sintering process and which may affect the quality of the finished product.

3.5 Physical Attributes of the Samples.

(Mckay *et al.*, 1994) mentions the particle size distribution as one of the base properties of lunar soils and soil classification systems that give us knowledge of the engineering properties of soils which is imperative for construction and engineering design. These include the compressibility, shear strength, volume change behaviour, thermal properties as well as coefficient of uniformity and chemical properties of regolith due to wide distribution of the particle size.

The shape of lunar soil particles may vary from spherical to angular (Mckay *et al.*, 1994) with an elongation of ~1.35 in a preferred orientation, thereby making soil to be in an anisotropic form and this has characterized its cohesive behaviour while the dense packing of soil particles increases the shear strength of the lunar soil. This would allow the excavation of a stable trenches under low lunar gravity. The absence of an atmosphere on the moon serves to increase the coefficient of friction of the grain particles and to enhance the firm contact of grain particles (fine or coarse) due to friction, which leads to improved traction for wheeled vehicles.

Adequate compaction and consolidation of the lunar soil should be carried out before any construction so as to avoid differential regolith settlement that would cause structural failure. The density of lunar soil increases due to the vibration caused by passage of numerous shock waves through the material. Therefore, any increase in bulk density will lead to an increase in shear strength, volumetric stability, heat capacity, abrasion resistance and porosity reduction. Micrometeorite impacts would reduce the voids between particles of regolith and consequently improve adhesion and bonding between them.

3.6. Sintering in the lunar environment

The sintering process in the lunar environment will be affected by the lower gravity, and by the lack of an atmosphere. During the sintering operation, the dimensions of the samples in the furnace decrease and become distorted due to gravity reduction. This slumping effect will be reduced in the lower lunar gravity. Also, gravitational settling of heavier minerals will happen more slowly in a sintering process on the moon. Lastly, as there is no atmosphere, all heat transport is by conduction through the base of the sample and by radiation from its exposed surfaces. As heat is being generated in the sample the energy will be lost through the surface radiation.

3.7 Published studies on sintering of regolith simulants

A number of authors have investigated the behaviour of regolith simulants undergoing sintering. Here we provide a brief series of references to a selection of investigations reported in the literature.

advocate for using a 3D-printing technique to manufacture a space frame structure through a direct extrusion where a JSC-1A regolith simulant was sintered in the air and hydrogen environment thereby producing toughened micro-trusses.

(Fateri *et al.*, 2014)investigated the fabrication of lunar glass using a selective laser melting process where soda lime powder was sintered and subsequently optimised to produce a glass of good surface finish.

(Balla *et al.*, 2015)used Laser Engineering Net Shaping to carry out a direct sintering process (in a freeform environment) on JSC-1AC simulant. The laser beam was used to melt the lunar simulant JSC-lAC until the structural elements were produced with a good surface finish.

(Goulas *et al.*, 2016)investigated powder bed fusion, where a laser melting technique employed JSC-1A lunar simulant to produce multi-layer structures. This additive technology was used as a potential on-site manufacturing process for structural components. Mechanical tests were performed on the manufactured samples to determine their reliability during the service conditions. These tests indicated that this process had potential for future applications of lunar settlement.

CHAPTER FOUR CHARACTERIZATION AND PREPARATION OF SINTERED BP-1 SIMULANT COMPACTS

This chapter presents a detailed description of BP-1simulant and a comparison of its detailed geotechnical properties to those of lunar soil and other simulants. In the second half of the chapter, we will discuss the preparation of the green compacts and the sintering of the compacted samples.

4.1 Origin and general characterization of BP-1 regolith simulant

The Black Point-1 simulant is obtained from a rock quarry of in a volcanic field in northern Arizona. Its major elemental chemical composition approximates that of a low-Ti mare regolith.

The modal mineralogy of BP-1 includes Hematite, Quartz, Labradorite, Calcite, Augite, Olivine and Magnetite. BP-1 basalt has a high total alkali of Na_2O and K_2O, with a high Fe and Mg (a hygroscopic solid mineral) content relative to most basalts. Table 4.1 lists the mineral composition of BP-1.

The quarry site of BP-1 basalt (Fig 4.1) contains other deposits of silt which have geotechnical properties similar to the Chenobi and NU-LHT-2M regolith simulant. The BP-1 simulant was classified as a silt sand according to the USCS ASTM D2487 standard (Carrier, 2003). Because of its derivation from basalt, it has a similarity with lunar Mare soil and its plagioclase content is relatively high

Figure 4.1 Black Point basalt lava flow. Source: D.B. Stoeser, and S. Wilson (2010)

Figure 4.2 BP-1 simulant. Source: Stoeser, D.B and Wilson S. (2010)

Table 4.1 The constituent of minerals element BP-1simulant. (Stoeser & Wilson, 2010)

Mineral	**Weight %**	**Property**	**Value**
Olivine	6.2	Peak angle of friction	39.51^0
Calcite	2.7	Maximum density	$1.86g/cm^3$
Quartz	1.7	Minimum density	$1.43g/cm^3$
Augite	23.7	Cohesion	0-0.2KPa
Hematite	2.0	Specific Gravity	2.81
Labradorite	60.7		
Magnetite	3.0		

Table 4.2 The constituent oxides of BP-1simulant. Source: Stoeser & Wilson (2010)

OXIDE	W 172158	W172154
Al_2O_3	16.7	16.4
SiO_2	47.2	46.9
Fe_2O_3	5.9	8.2
FeO	6.2	3.7
CaO	9.2	9.6
TiO_2	2.3	2.2
MgO	6.5	5.6
MnO	0.21	0.21
Na_2O	3.5	3.4
K_2O	1.1	1.1
P_2O_5	0.52	0.51
CO_2	0.05	0.26
H_2O^+	0.41	0.69
H_2O^-	0.11	0.51

The BP-1simulant has a resemblance to the lunar soil samples collected by Apollo 17 astronaut Harrison Schmidt, both in composition (e.g. silicate, phosphate and pyroxenes) and geotechnical properties such as bulk density, particle size distribution, and shear strength etc.

BP-1simulant is available in large quantities, does not require large-scale processing and is consequently inexpensive to produce; therefore, it can be used to carry out lunar research (Everingham, et al., 2008).

4.2 Test procedures employed for characterization of BP-1

4.2.1 Particle size distribution

The particle size distribution was analysed using a Horibar Laser Scattering machine to determine the range of particles size in each sample.

A sample of unsieved BP-1 (as received) was fed into a RETSCH PT100 Sample Divider. A 30.00g sample was fed into a circulation system with distilled water before agitating it for 30 seconds until a homogenous mixture was achieved. A 1.0 ml mixture was taken out at three different depths of the bucket after it has been stirred thoroughly, while a Horiba laser scattering PSD LA-950 Analyser was prepared by feeding it with water and agitated continuously before 5.0% sodium hexa-metaphosphate (5%NaHP) was added however. Then, a portion of 1.0ml diluted samples was fed into the analyser before carrying out alignment, blank and ultrasonic process for three minutes. The experiment was conducted three times in order to obtain a large accuracy before the result were compared. The outcome of the experiments is presented in Chapter 5.

4.2.2 Surface Area

The sample of lunar regolith BP-1 simulant was carefully prepared and exposed to inert gas at liquification temperature (77.35K) thus, removing the weakly adsorbed molecules. The gas molecules randomly move to the surface of the sample and are then attracted by surface energy. As the pressure increases, the number of molecules striking the surface per unit time increases and this corresponds to the quantities adsorbed. At the equilibrium point, the molecules were adsorbed and there was a loss of heat adsorption, which later desorbs at the surface. Therefore, the rate of condensation of molecules was equal to the rate of desorption. When this occurred, the multiple layers of molecules that cover the free surface were more while the pore walls were filled. But as soon as the adsorption reaches the final target at the saturation pressure, the desorption process takes place, where the gas is progressively withdrawn until the initial state is reached while ignoring the lateral interactions of adsorbed molecules since the heat of adsorption occurred for a few second; therefore, each layer that was produced was equal to heat of liquefaction.

4.2.3 The Isothermal mechanism

The process of physical adsorption occurs when the molecules from the gas phase strike the surface of the sample, and at the point of equilibrium, the molecule will adsorb and lose the heat of adsorption. The Isothermal mechanism will display a both monolayer and multilayer adsorption on the walls of mesopores (2-50nm) and macro pores. As the gas pressure increases, the formation of monolayer will be created along the capillary wall. Further increase in gas pressure will bring about the formation of multilayer sorbent to the surface, which eventually condenses (below the saturation pressure) that gives rise to the Isotherm. Furthermore, as the layer formation continues the pressure increases until it approaches a constant value while the density becomes constant. Then the amount of gas adsorbed or desorbed at standard temperature and pressure was generated through the software as well surface area, total volume of pores and pore size.

4.2.4. X-ray fluorescence (XRF) analysis

When the glass disc sample of BP-1 simulant (as received, 212, 106 and 38μm) was prepared, it was loaded directly into a P-Analytical Axios Max Equipment (XRF with 60 kV X-ray tube). As the XRF machine was in operation, the beam of X-ray radiation was incident on the samples. The sample atoms become ionized to absorb some energy while others were dispersed due to a decrease in binding energy of the electron orbital. The energy release was later analysed quantitatively by the machine to determine the compositional elements in the sample and this process fulfilled the condition of Bragg's Law and last for 2.07minutes.

Bragg Equation: $n\lambda = 2d \sin \theta$ where n= 1, 2, 3. Where reflected angle θ, while the integer number of wavelengths ‘n’ and (λ) measure the wavelengths of the incident wave, at a distance ‘d’ between the crystal atoms.

Figure 4.3 PANalytical Axios Max Equipment used for XRF analysis.

4.2.5 XRD analysis.

2.0g of unsieved Black Point-1simulant powder was mixed with approximately 10.5% of a corundum Al_2O_3. The analysis of the powder simulant was carried out in a

P-Analytical Pert diffractometer with a Cobalt X-ray source equipment

4.2.6. Particle morphology

The morphology of the particles was investigated using electron microscopy. A small size of 5 samples of a Black Point - 1 powder was coated with graphite and then mounted on a sample holder. The sample surface was charged when scanned with an electron beam before performing a microanalysis on each specimen using a Nova Nano-SEM of 5.00Kev energy and at a working distance of 5.8mm. The images acquired have a resolution of 100, 20 and 10µm respectively.

4.2.7 Thermogravimetric measurements

41.65mg of unsieved BP-1simulant was measured and poured into Aluminium crucible (covered with the lid). Both the sample and reference crucible that calibrate the baselines were loaded into the sample carrier of a Simultaneous Thermal Analysis STA 409/ TGA/DSC equipment while the furnace provides a homogeneous temperature zone required for the experiment.

Then a 5psi of gas pressure was released three times to expel the oxygen gas in an evacuating system while the sample crucible was in contact with the heating sensor.

The software system connected to the TGA/DSC equipment measured the temperature and the heat flow while at the same time generating the TGA/DSC graph. The technique was operated in an environment of an argon gas with 20ml/min^{-1} purging rate.

The TGA measured the amount of evaporation of the sample of BP-1 (weight loss) while the DSC measured the melting temperature at 1179^{o}C of BP-1 simulant during heating.

The used of BP-1simulant to carry out the TGA/DSC experiments was necessary in determining the phenomenon of heat transport within the lunar regolith such as emissivity measurement, thermal conductivity distribution, thermal optical properties and as well as the suitability of a thermal-based additive technology such as laser sintering and industrial 3D printing for the construction of structural components in the lunar base.

4.3. Glass preparation

The crucible and mould were placed on the heating chamber of M4-fluxer equipment where it was pre-heated for five minutes before the actual fusion activities started.

The glass preparation began when the 2.0g of sample powder of Black Point -1 simulant was thoroughly mixed with a lithium borate flux. Then the mixture was poured into the crucible and then heated until all the flux is melted, as the temperature is progressively increased to 900^{o}C the sample dissolved into the molten fluxes thereby forming a melt. As the arm of the fluxer M4 is rotated the melt was poured into the mould and then left to cool at room temperature 23^{o}C.

4.3.1 The study of the suitability of sintering in an inert atmosphere versus air

The vacuum furnace is ideal equipment that would be suitable for manufacturing of structural elements in the Moon because of high temperature required for reducing unexpected contaminant and heat loss through the convection. Since the lunar environment is a vacuum, strictly speaking the most accurate simulation of lunar sintering would be done using a vacuum furnace. However, as we did not have ready access to a vacuum furnace, we considered sintering in an inert atmosphere, and most simply, in a normal air atmosphere. Moreover, we were concerned about outgassing contamination of vacuum equipment by the green compacts we were to sinter. Therefore, an inert or air atmosphere was sought.

Sintering in an atmospheric inert furnace will protect the sample from effects of oxidation and decarburization with flowing inert gases (nitrogen, argon) that will negatively affect the test pieces appearance and properties hence, to maximise the energy efficiency the furnace chamber was surrounded with a high thermal efficiency of ceramics material (alumina fibre-insulation).

Moreover, based on the experiment performed on TGA/DSC analyser in the air and argon environment the results obtained is relatively similar to each other as shown in the graph below. Since there was not much difference, this necessitates the sintering process to be conducted in a muffled furnace.

4.4 Sieving the samples

The first step in sample preparation was carried out using sieve BS410-1 to separate out particle grains of different size 38, 106, 212μm and Unsieved (as received). When the sieve analysis was performed a homogeneous porosity across the sample of BP-1 simulant was obtained.

4.5 Pressing of the green compact samples

In order to make the green compacts, 20g powder of each grade of sieved material was measured before pouring into a cylindrical mould of 1.21cm height x 30cm diameter. The samples were uniaxially compressed with a pressure of 308.9 N/mm^2 (44, 80 psi) under a high-pressure using Carver Laboratory Manual Press Model 46273002 at room temperature thus, forming a 'green compact'. The soil grains of each sample were adequately packed with sufficient cohesion to allow handling while the initial densities

of each compact range of 1.94 - 2.32 g/cm^3. In all, four samples set of fourteen each was produced with different grain size as mentioned above.

Figure 4.4 Production of green compact from uniaxial compression.

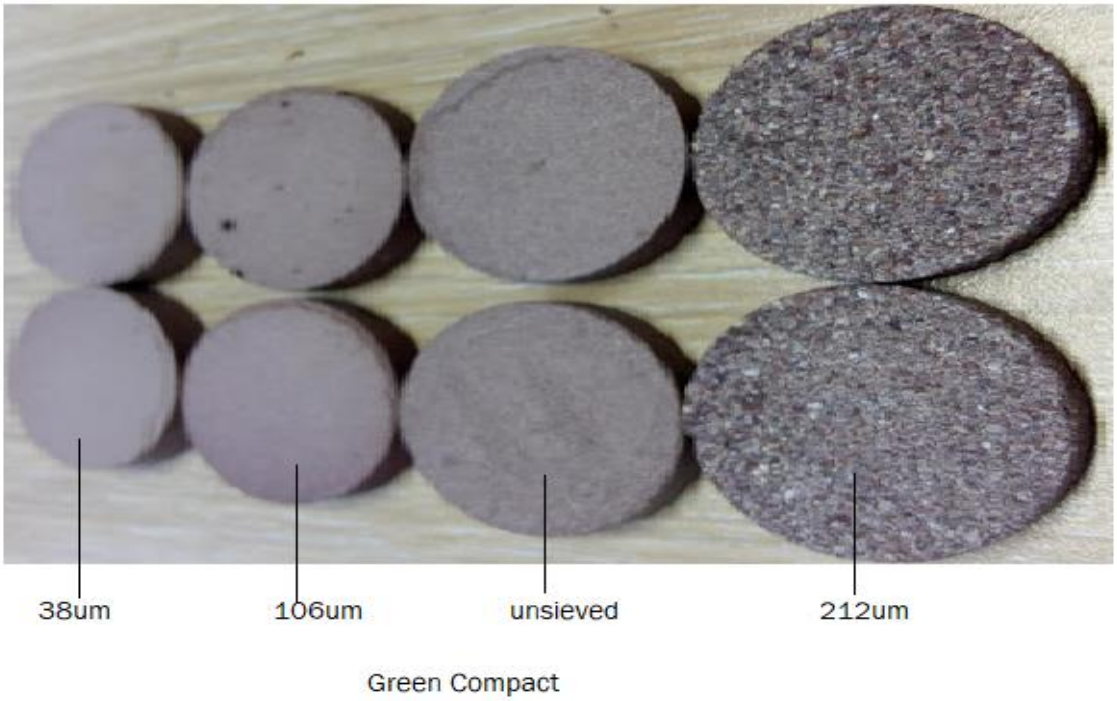

Figure 4.5 Green compacts (measure -micrometre) produced from the bulk unsieved BP-1 and sieved samples of 38μm, 106μm and 212μm.

The second step involved the removal of each sample from the mould, which was very difficult in handling because of frequent breakage due to adhesion force between the particles and the mould surface, as a result, it was very fragile during the transportation to the furnace.

4.6 Sintering sample production

A laboratory benchtop muffle furnace Amalgams H30210.4F model with a volume of 420 x 540 x 570mm was used. Molybdenum heating elements were embedded on top and both sides of the furnace and this provided temperature uniformity with a maximum working temperature of 1200°C.

The green compact (grey colour) of each sample was placed in the laboratory Muffle Furnace where it was heated to 1100^0C. In the first test run the sample was left for 60 minutes to allow it to be sintered.

An experiment was carried out to determine the conditions of environment under which sintering take place; hence the compressive strength of simulated brick was examined based on the effect of temperature, microstructure, compaction and heating time.

The samples of each green compact were heated in the furnace at a temperature of 1100^0C for one hour five minutes (1:05hrs). Between 1097-1104^{o}C the temperature began to fluctuate due to thermal inertia that exceeded the maximum allowable temperature.

Furthermore, the samples were left in the furnace during sintering process for 90.0 minutes. After the furnace cooling was allowed to occur for 16.00 hrs however, it was observed that the temperature remains steady at 1100^{o}C for 10 minutes. Finally, all the samples were removed from the furnace.

Four batches of the sample of different grain size-212, 106, 38μm, and unsieved (as received) were produced from BP-1 simulant and was subjected to sintering process for 90 minutes at a temperature of 1100^{o}C.

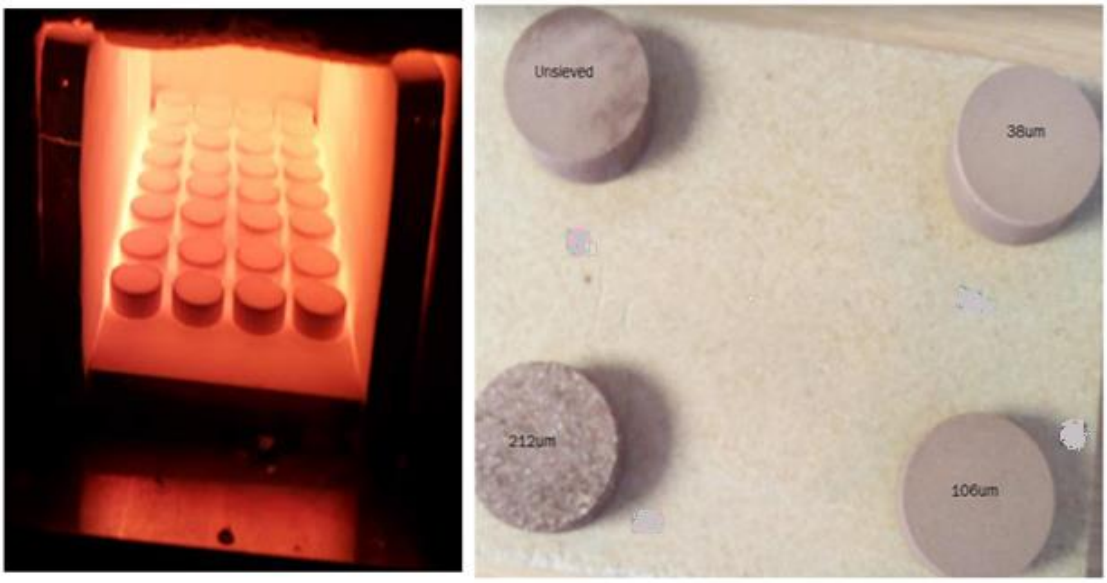

Figure 4.6 (*Left)* Samples being heat treated in the furnace (*Right*) Sintered samples of different particle size grades after removal from the furnace (temperature 1100ºC, for 90.00 minutes each)

The average samples (figure 4.6 above) of the lowest grain size of 38µm, had a mass of 18.55g with a height of 12.253mm and a diameter of 30.94mm. The medium particle size sample with 106 µm had a mass of 19.06g, a height of 12.23mm and a diameter of 30.82mm. The samples with the largest grain size, 212 µm, had a mass of 19.43g, a height of 11.75mm and diameter of 30.79mm. The compact made of unsieved BP-1 had a mass of 19.31g, a height 11.47mm, and diameter of 30.97mm. After sintering all the samples retained their shape – i.e. no slumping was noted. Each sample produced shows a strong, tough and coherent brick with uniform texture.

After sintering, there were very few visible differences observed in each of these specimens.

One such difference was that cracks were observed in the observed in the surface of some of these samples except for the 212µm sample, and this an indication of thermal stresses that were build up at a high temperature in the furnace hence, the specimen shows a high degree of particle bonding at the circumference.

As the sample heat was been generated in the furnace and passed into the body of each sample, a change in temperature was observed and this led to shrinkage and subsequently a reduction in mass due to heat flux that builds up during the heating process.

4.7. Experimental Apparatus and Test Procedures

A Zwick Roell X-force HP Compression Testing Machine (SN 755571), capable of producing a maximum compression force of 250 KN, was used to perform compression tests in all the sintered samples. The data were logged and pre-processed by the test-Xpert III testing software system.

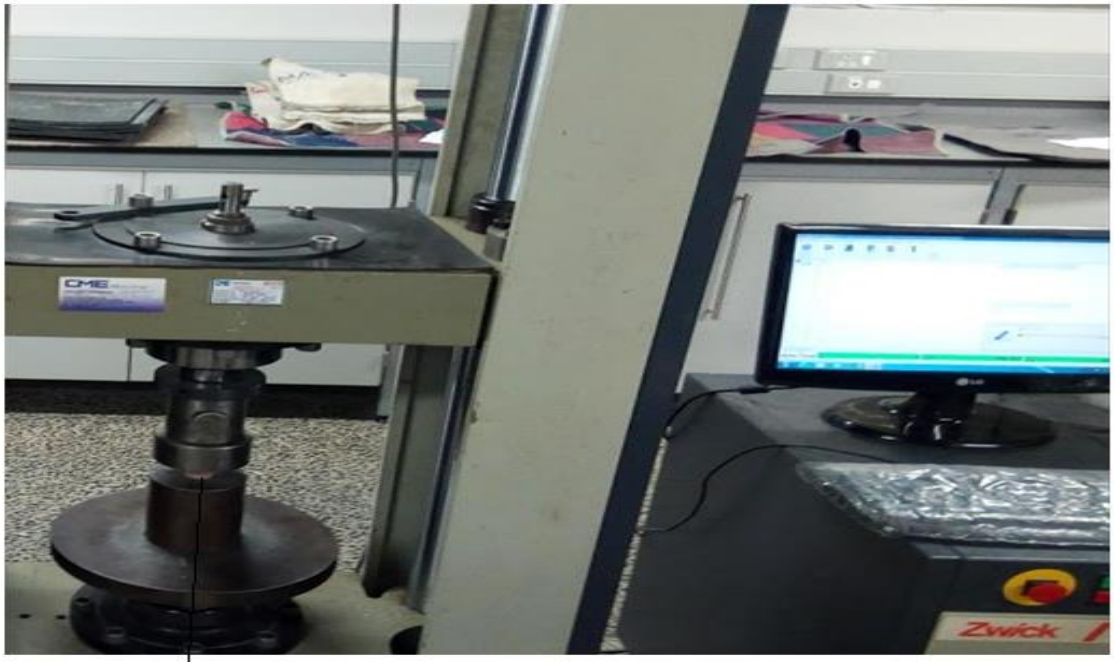

Figure 4.7 Green compact in a compression machine connected with software in order to determine the measurement

Each sample of low, medium and high porosity was placed in the tester in between the upper and lower compression plates before applying a gradually increasing force until specimen failure was detected, at which point the compression of the sample was stopped abruptly. The data was recorded at 5 points per second and measured the applied load in KN and resultant displacement of the crosshead in millimetre (mm). This experiment was conducted at ambient room temperature (23^{o}C) and pressure.

Table 4.3 Sample physical dimension statistics for the porosity set of different grain size after sintering.

The Physical dimension statistics of sample porosity sintered at 1100°C for 90minutes				
Sample number µm	Mass (grams)	Average Height (mm)	Average diameter (mm)	Average density/cm^3
38A	18.570	12.490	31.000	1.967
38B	18.650	12.250	30.800	2.043
38C	18.913	12.030	30.900	2.096
38D	18.080	12.240	31.080	1.947
Mean	18.5532	12.2525	30.945	2.014
Variance	0.0907	0.026	0.011	0.003
STD	0.312	0.163	0.105	0.059
106A	19.333	12.130	30.080	2.242
106B	19.417	12.480	31.000	2.061
106 C	19.240	12.070	31.010	2.253
106D	18.283	12.250	31.180	1.954
Mean	19.068	12.232	30.820	2.128
Variance	0.209	0.025	0.186	0.016
STD	0.458	0.157	0.432	0.126
212A	19.450	12.000	30.010	2.291
212B	19.527	12.010	31.000	2.154
212 C	19.383	11.490	31.180	2.209
212D	19.350	11.500	31.000	2.229

Mean	19.427	11.750	30.800	2.221
Variance	0.0046	0.651	0.212	0.003
STD	0.0067	0.255	0.461	0.050
Unsieved A	19.313	11.050	31.000	2.315
Unsieved B	19.340	12.340	31.080	2.065
C Unsieved	19.317	11.260	31.000	2.273
Unsieved D	19.273	11.250	30.800	2.2991
Mean	19.311	11.475	30.970	2.238
Variance	0.001	0.2564	0.011	0.010
STD	0.024	0.5064	0.103	0.101

CHAPTER FIVE DISCUSSION AND RESULTS

5.1 Particle size distribution analysis

A Horiba PSD LA-950 laser scattering analyser was used to carry out particle size

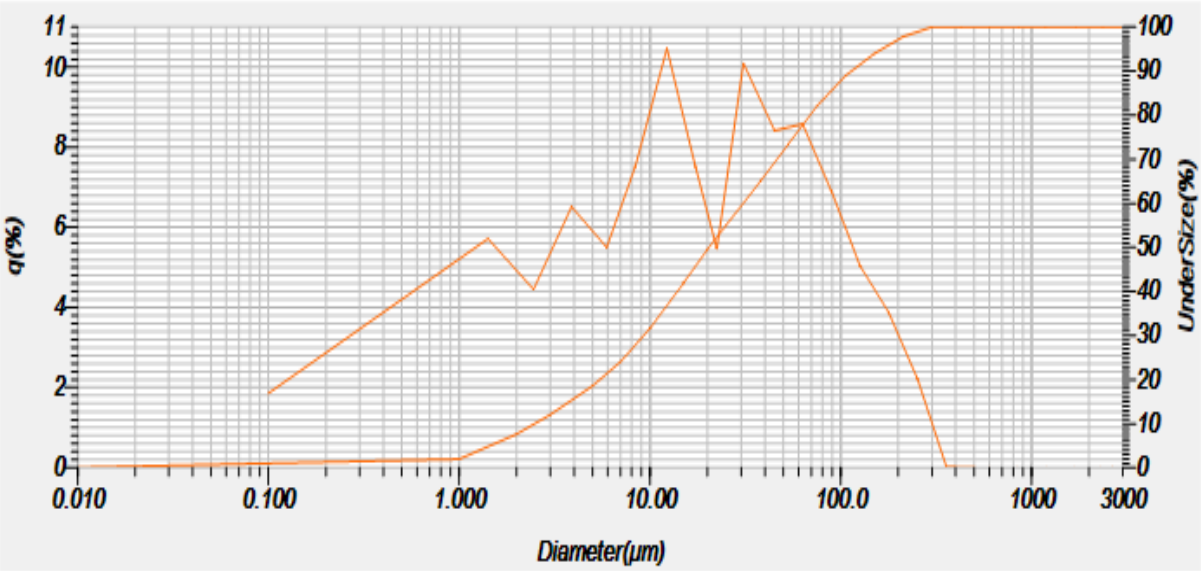

Figure 5.1 The graph of a grain size distribution of a BP-1simulant ranging from 0.01-30μm (micrometre) using a laser diffraction for particle analyser

distribution studies on the BP-1 powder. The measurements were conducted three times for each grade (i.e. unsieved, 212 um, 106 um and 38um) in order to average out sampling variations in each grade.

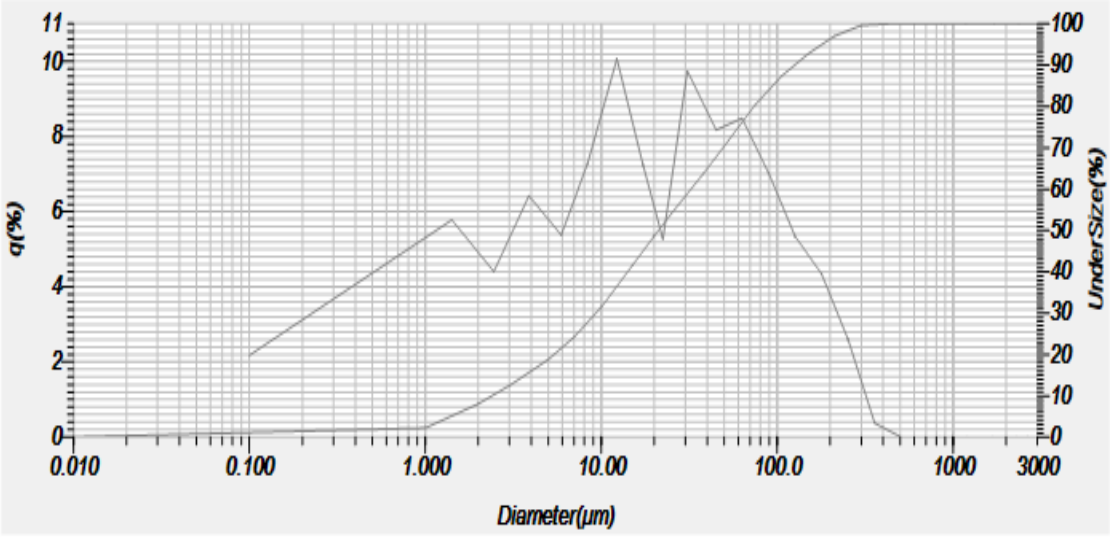

Figure 5.2 The graph of a grain size distribution of the BP-1simulant ranging from 0.01-30μm (micrometre) using a laser diffraction for particle analyser

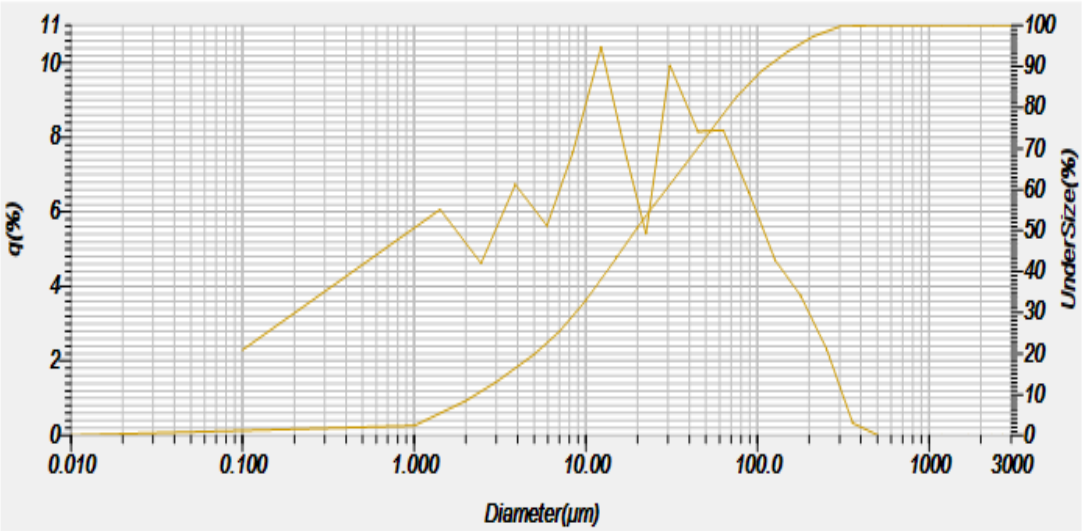

Figure 5.3 The graph of a grain size distribution of the BP-1simulant ranging from 0.01-30µm (micrometre) using a laser diffraction for particle analyser

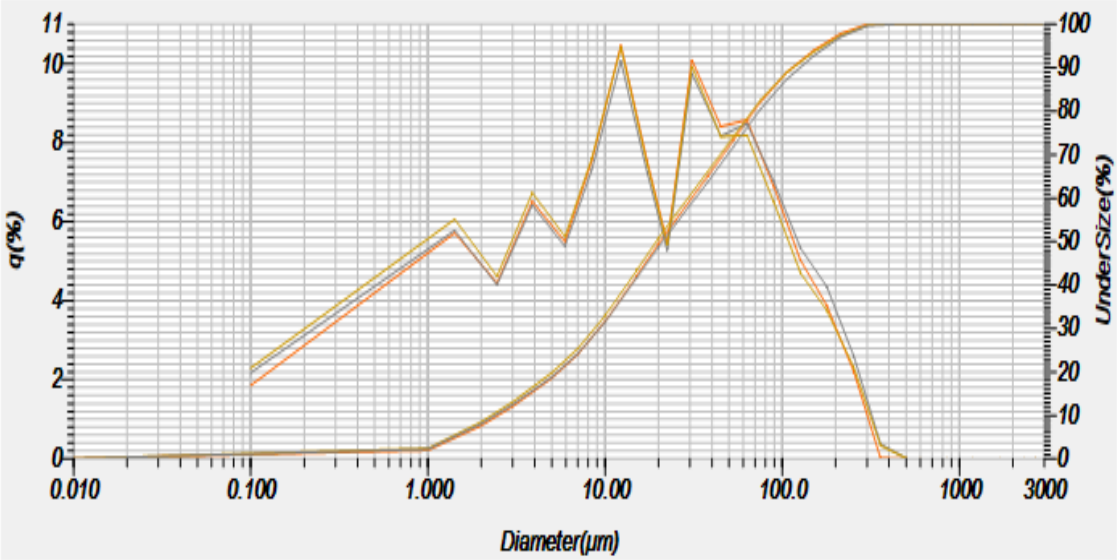

Figure 5.4 The graph of a grain size distribution of the BP-1simulant ranging from 0.01-30µm (micrometre) using a laser diffraction.

The figure (5.1, 5.2,5.3. and 5.4) above show the size distribution of particles where a volume-based distribution was plotted against the particle sizes, the samples were examined for shape distribution using aspect ratio as the morphological descriptor. The dynamic image measured hundreds of thousands of single undersize and oversize of particles in the bulks of BP-1 simulant. A field of view was covered shown a large representation of sample volume and each measurement took approximate 156 seconds. The oversize particles create scratches on the surface while the undersize adhesively

bonded to the abrasive grains on the substrate therefore, an exact information on every single particle of the simulant with specific characteristics were revealed showing the true particle projections at every segment while various dimension of irregular particles shaped were determined and this ranges between 0.01-30µm (micrometre) and from circularity, sphericity, symmetry, compactness, roundness, to convexity. The particles shape affects the soil shear strength while the soil gradation and grain size affect the shear resistance of the soil i.e. the angular grains would provide adequate interlocking, thereby increasing the shear strength of the soil. In addition, the three graphs resemble each other thereby shown a homogeneous mixture. The particles size distribution reveals how well a soil is graded in bulk of soil mass and this helps in soil classification and avoid differential regolith (soil) settlement.

Summary Report of a Black Point-1(BP-1) simulant.

Table 5.1 The Anaslysis of surface area for a BP-1 simulant

Measurement	**Relative Pressure (P/Po)**	**BET**	**Single point adsorption total pore volume less than**	**BJH Adsorption**	**BJH Desorption**
Surface Area	P/Po= 0.175166632: 3.3843 m^2/g	Surface Area: 3.4654 m^2/g		Cumulative surface area of pores between 17.000 Å and 3,000.000 Å width: 1.741 m^2/g	Cumulative surface area of pores between 17.000 Å and 3,000.000 Å width: 1.8829 m^2/g

Pore Volume			3,823.617 Å width at P/Po = 0.994934733: 0.003534 cm^3/g	Cumulative volume of pores between 17.000 Å and 3,000.000 Å width: 0.002848 cm^3/g	Cumulative volume of pores between 17.000 Å and 3,000.000 Å width: 0.002970 cm^3/g
Pore Size		Adsorption average pore width (4V/A by BET): 40.7955 Å		average pore width (4V/A): 65.439 Å	average pore width (4V/A): 63.084 Å

5.1.2 Porosity

Porosity was determined by measuring desorption of a gas on the surface of the pores in the grains. Many reactions occur at equilibrium point; the molecules were adsorbed, loss of heat adsorption was observed while the pore walls were filled with multilayer of molecules before the whole surface was covered. In addition, the number of molecules taken up by the surface depend on temperature, pressure, surface energy distribution and surface area. Therefore, the value of surface areas was determined from the Brunauer–Emmett–Teller (BET) equation.

$$V = \frac{V_m C P}{(P_0 - P)\{1+(C-1)(P/p_0)\}} = \frac{P}{V(P_0 - P)} = \frac{1}{V_m C} + \frac{(C-1)x^2}{V_m C}\frac{P}{P_0} \quad (1)$$

$$\text{Surface Area } (S_{total}) = \frac{V_m N_s}{V} \quad (2)$$

$$\text{Specific Surface Area } (S_{BET}) = \frac{V_m N_s}{Va} \qquad 3$$

V_m is the monolayer adsorbed gas quantity while C is the BET constant, N is Avogadro's number, s the adsorption cross section of the adsorbing species, V is.

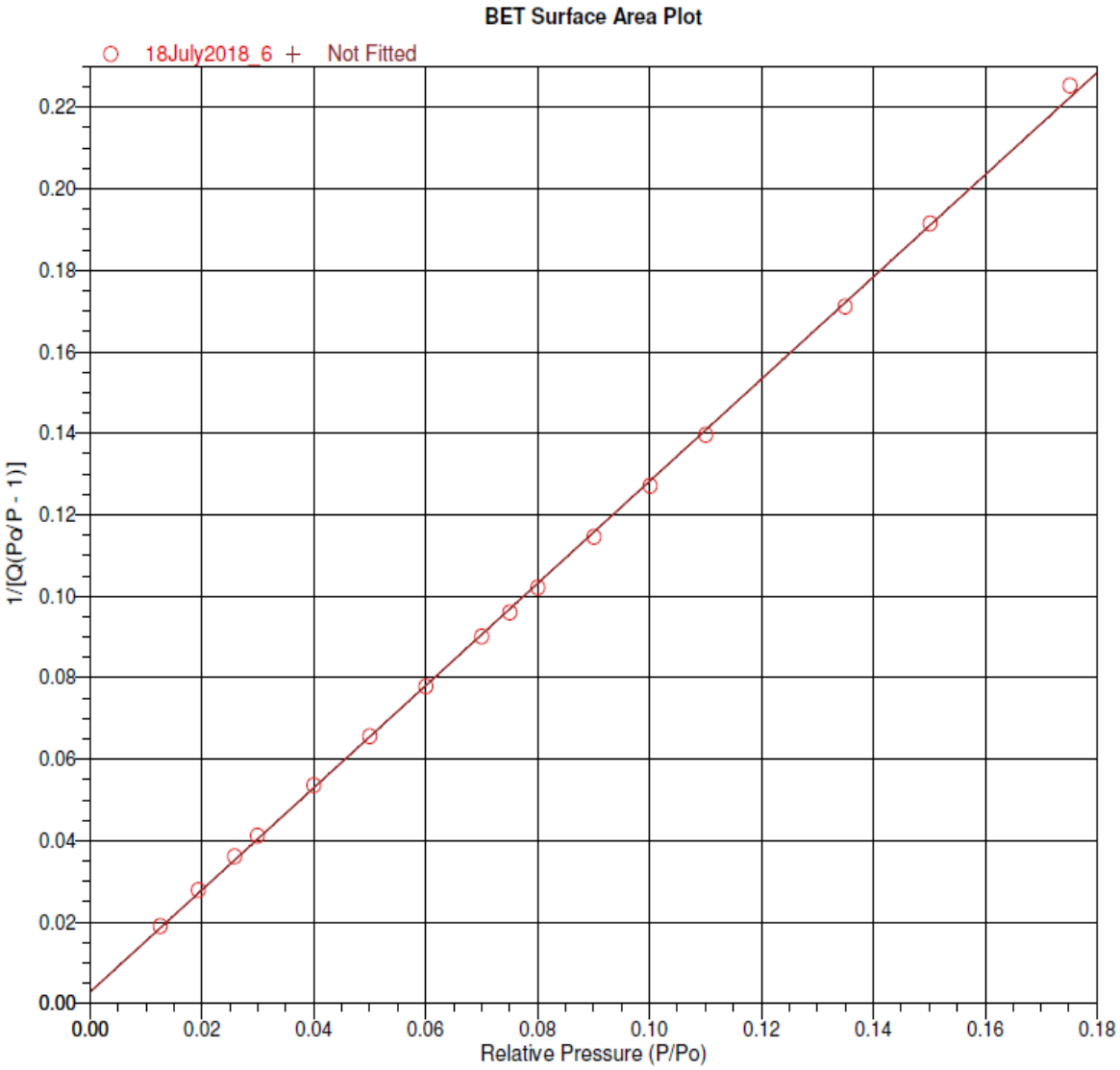

Figure 5.5 Volume of nitrogen plotted as a function of relative pressure BET Surface Area.

the molar volume of the adsorbate gas, and a the mass of the solid sample or adsorbent.

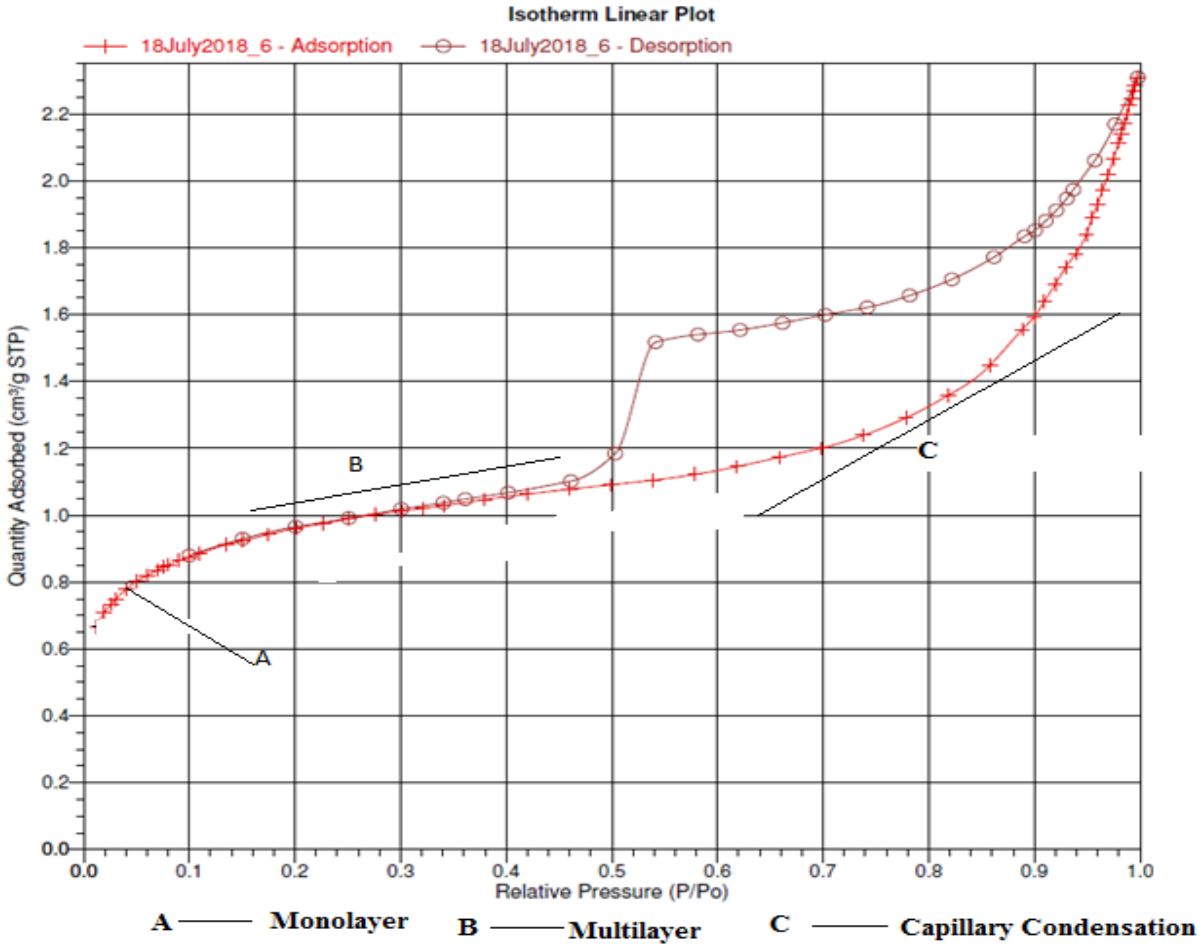

Figure 5.6 Various layers from monolayer, multilayer and capillary condensation as well as isotherm in the relative pressure P/P^0.

The process of physical adsorption occurs when the molecules from the gas phase strike the surface of the sample and at the point of equilibrium, the molecule adsorbs and loses the heat of adsorption. The Isotherms mechanism displayed both monolayer and multilayer adsorption on the walls of mesoporous (2-50nm) and macro pores. As the gas pressure increased the formation of monolayer were created along the capillary wall. Further increase in gas pressure brought about the formation of multilayer sorb to the surface and eventually the adsorbate condenses (below the saturation pressure) this give rise to Isotherm.

The total pore volume was estimated as shown in Figure 5.6 where various layers from monolayer, multilayer and capillary condensation as well as isotherm in the relative pressure P/P^0 range 0.4-0.54 due to tensile strength effect. Furthermore, as the layer formation continues the pressure increases until it approaches a constant value (1) while the density becomes constant. Then the amount of surface area, total volume of pores

and pore size, gas adsorbed or desorbed at standard temperature and pressure were generated through the software system

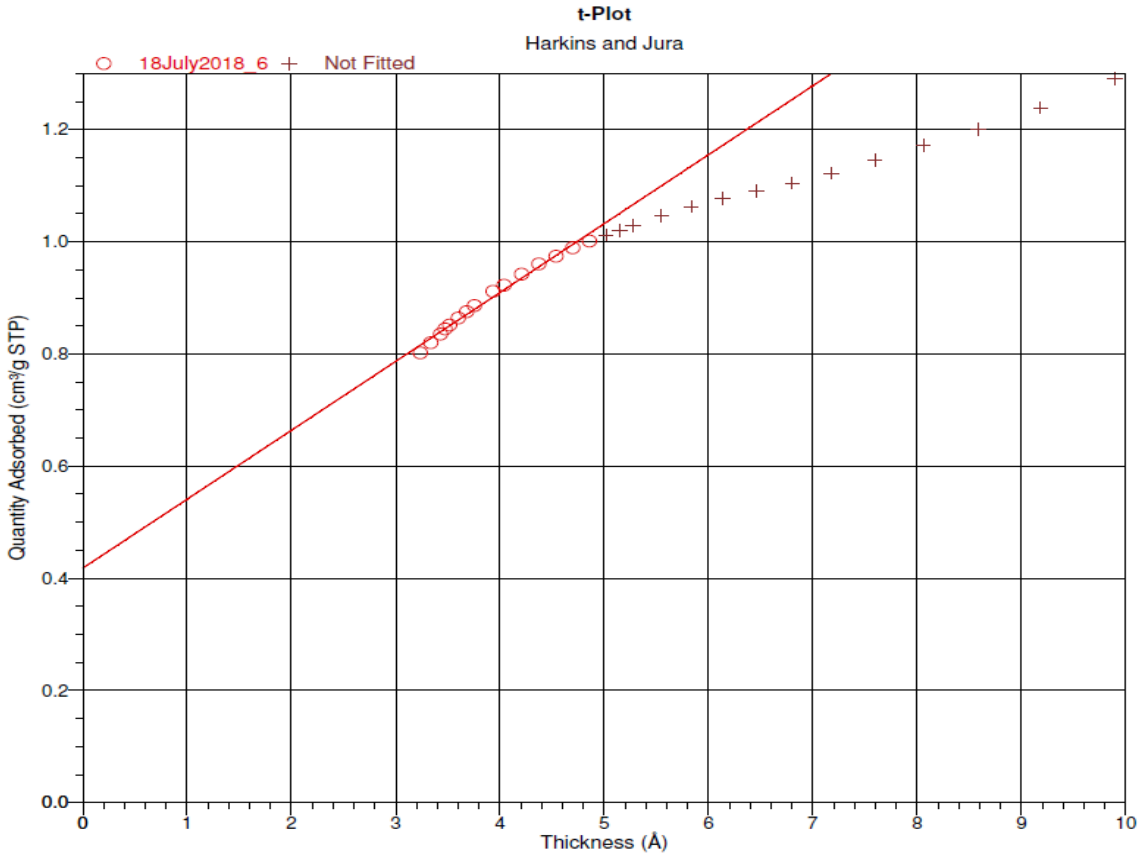

Figure 5.7 The graph of quantities adsorbed at STP versus thickness was plotted as shown.

The graph shows the adsorption isotherms that reveals the volume adsorbed versus thickness (t) for every value of P/P^0. The volume adsorbed is plotted against the corresponding value of thickness and this gives a straight line and the slope shows the external surface area and area of micro-pores. Hence, the y-axis intercept yields the micro-pore volume to be $0.415 m^2/g$ thence, the linear range lies between the monolayer and capillary condensation. Therefore, the use of probe molecules is essential for obtaining an accurate micro and mesopore analysis as well as surface area.

5.2. XRF analysis

Major oxides are measured on fused disks which were prepared from ignited powders, (except for H_2O^- and LOI). The water (H_2O) in the table above shows the amount of weight lost when heating the sample powder at 110° overnight, while the *loss on ignition* (LOI) reveals the amount of weight change when heating the sample to 800°C for 4 hours. Therefore, samples can gain weight during ignition if they have little

water and abundant ferrous iron (which oxidizes to ferric iron oxide, Fe_2O_3), thus, up-taking oxygen. The limit of detection of major oxides is 0.01 wt. %, therefore any oxides below this limit would be too low to be quantified.

Major element composition of BP-1 was compared with published data for other regolith simulants JSC-1, FJS-1, MKS-1 and with Apollo 14 lunar regolith, as shown in the Table 5.3 below

Table 5.2 The major element and oxide composition of BP-1 simulant.

Major Elemental composition of BP-1 was compare with JSC-1 simulant and Apollo 14 lunar regolith							
Sample	Weight %						
	SL-212	SL-106	SL-38	SL-unsieved	Unsieved Corrected		
SiO_2	44.82	46.02	44.25	33.57	44.66	47.71	48.1
TiO_2	2.07	2.13	1.86	1.59	2.11	1.59	1.7
Al_2O_3	15.87	15.13	15.80	11.69	15.55	15.2	17.4
Fe_2O_3	12.12	13.39	10.64	9.59	12.76	10.79	10.4
MnO	0.17	0.19	0.16	0.13	0.18	0.18	0.14
MgO	6.44	7.23	5.32	4.56	6.07	9.01	9.4
CaO	9.83	9.51	10.93	7.74	10.30	1.42	10.7
Na_2O	3.44	3.26	3.39	2.58	3.44	2.7	0.7
K_2O	0.97	0.99	1.07	0.76	1.01	0.82	0.55
P_2O_5	0.41	0.35	0.44	0.30	0.40	0.66	0.51
SO_3	0.02	0.02	0.03	0.02	0.02	-	-
Cr_2O_3	0.01	0.03	0.01	0.01	0.01	-	-
NiO	0.02	0.02	0.01	0.01	0.02	-	-
H_2O	0.14	0.27	0.44	0.21	0.28	-	-
LIO	1.57	1.93	3.43	2.38	3.17	0.11	-
Sum	97.90	100.46	97.76	75.16	100.00	99.01	99.6

XRD analysis was performed on the BP-1 material. The mineralogy contains quartz, calcite, hematite, pyroxene and ilmenite. The plagioclase composition are more than other minerals.

Table 5.3 Adapted from CAS-1 lunar soil simulant by Zheng et-al.

Major element composition of CAS-1 and compared with JSC-1, FJS-1, MKS-1 lunar soil simulant, and Apollo 14 lunar regolith

	SiO_2	TiO_2	Al_2O_3	FeO	MnO	MgO	CaO	Na_2O	K_2O	P_2O_5	LOI	Total
Apollo 14	48.1	1.7	17.4	10.4	0.14	9.4	10.7	0.7	0.55	0.51	–	99.6
CAS-1	49.24	1.91	15.80	11.47	0.14	8.72	7.25	3.08	1.03	0.3	0.52	99.46
JSC-1	47.71	1.59	15.02	10.79	0.18	9.01	10.42	2.7	0.82	0.66	0.11	99.01
FJS-1	49.14	1.91	16.23	13.07	0.19	3.84	9.13	2.75	1.01	0.44	0.43	98.14
MKS-1	52.69	1.01	15.91	12.28	0.22	5.41	9.36	1.9	0.58	0.14	0.5	100
14163	47.3	1.6	17.8	10.5	0.1	9.6	11.4	0.7	0.6	–	–	99.6

Apollo 14, average chemical composition of lunar regolith sampled by astronauts at Apollo 14 landing sites. Data of Apollo 14 and 14163 were cited from Heiken et al. (1991), data of JSC-1 was cited from McKay et al. (1993, 1994).

5.3. XRD Analysis

XRD analysis was performed on the BP-1 material. The mineralogy contains quartz, calcite, hematite, pyroxene and ilmenite. The plagioclase composition are more than other minerals

Table 5.4 The mineral content of BP-1 identified with XRD.

Serial Number	Minerals	Weight %
1	Olivine	5.4
2	Magnetite	3.2
3	Calcite	2.8
4	Augite	23.7
5	Hematite	1.8
6	Labradorite	61.2
7	Quartz,	1.9

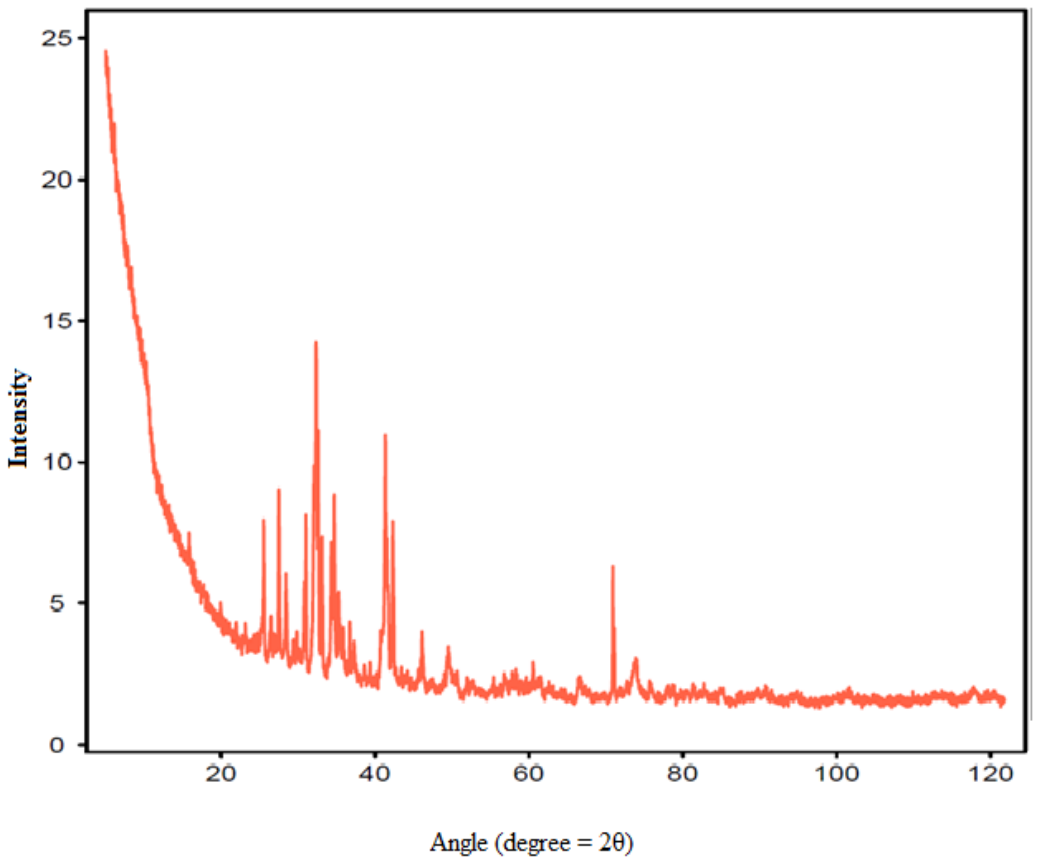

Figure 5.8 The intensity of the reflected X-rays at a rotational angle of 2θ.

As the sample and the X-ray detector is rotated around the path of a collimated beam, the intensity of the reflected rays was recorded (Fig 5.8), and later converted to count rate by software.

The X-ray diffraction techniques was used for the identification of crystalline phases of Black Point-1 simulant while the quantitative analysis reveals the modal amount of minerals contents in the sample thereby describing the three-dimensional atomic structure of crystalline. The two regions of diffuse scattering observed lies between 20-90^{o} (Figure 8) featuring the amorphous basalt glass. More so, variations of minerals compositions (Table 5.4) of olivine contents (0.2-5.4%), labradorite [(61.2%) plagioclase feldspar-(Ca, Na,) Al_2 Si_2O_8) 60.09] Augite crystal structure containing (20.69-23.7%) minerals constituent [(Ca, Na), (Mg, Fe, Al) $(Al, Si)_2O_6$] thus revealing a greenish brown colour resulted in altering the melting point of the regolith. And after few days of experiment a diffraction peaks indexed of quartz SiO_2, with other trace elements were observed.

5.4. Micrography Analysis

Scanning Electron Microscope images of the BP-1 powder reveal characteristic particle morphologies and textures Fig 5.10. The images in figure 5.10 (a) and (b) shows a clump of bonded particles with some aggregate of loose particles attached to each other. While figure (e) reveals the magnifications of BP-1 particles shape that ranges from angular to sub-angular.

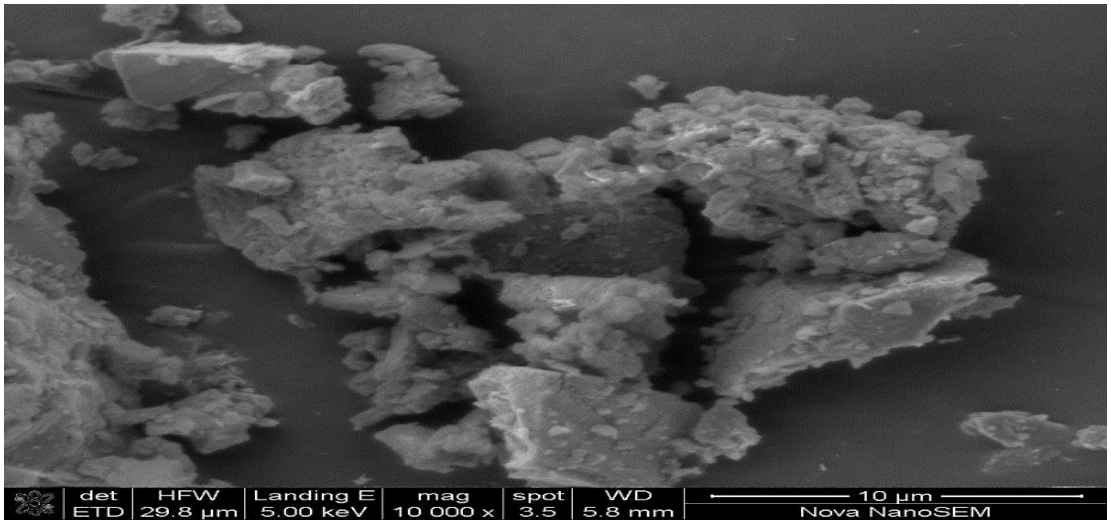

Figure 5.9 (a) shows the clump of bonded particles of BP-1 simulant with particulate of aggregate embedded in the outer layer that contains Mg and Fe

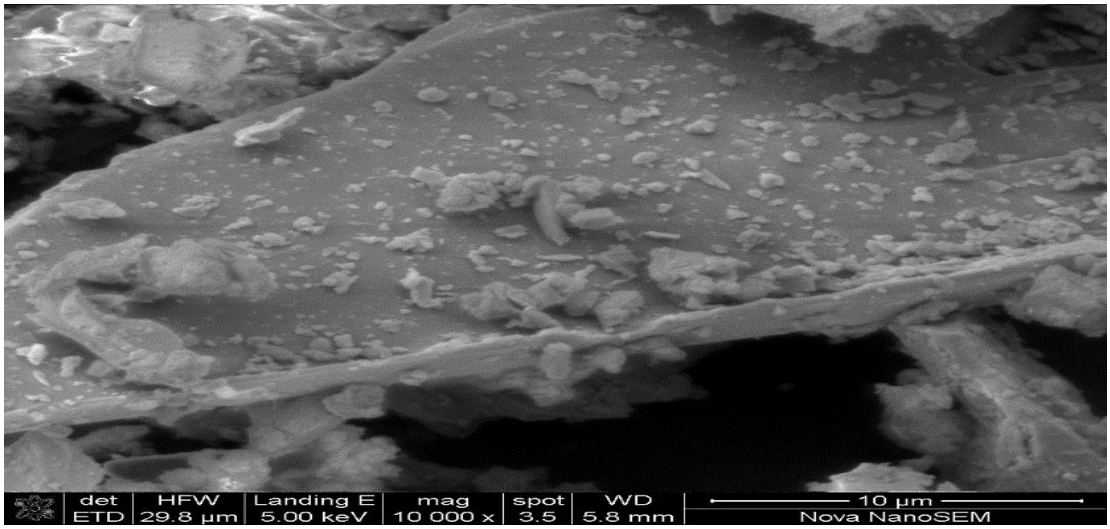

Figure 5.9 (b) shows the clump of bonded particles of BP-1 simulant with particulate aggregate embedded in the layers.

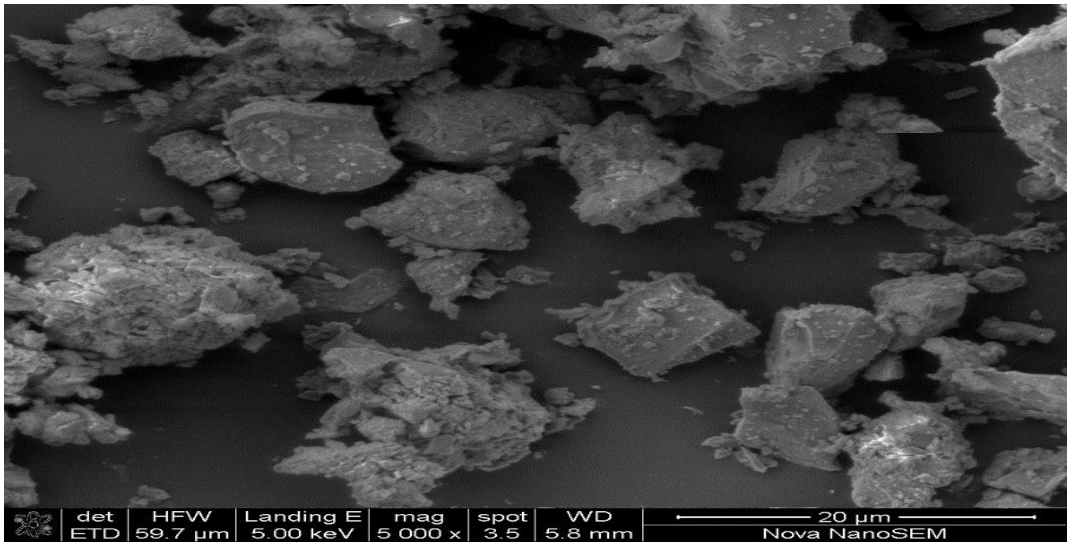

Figure 5.9 (c) The aggregate of loose particles attached to each other embedded with Al and Si Al (darker region) and Mg and Fe (light area).

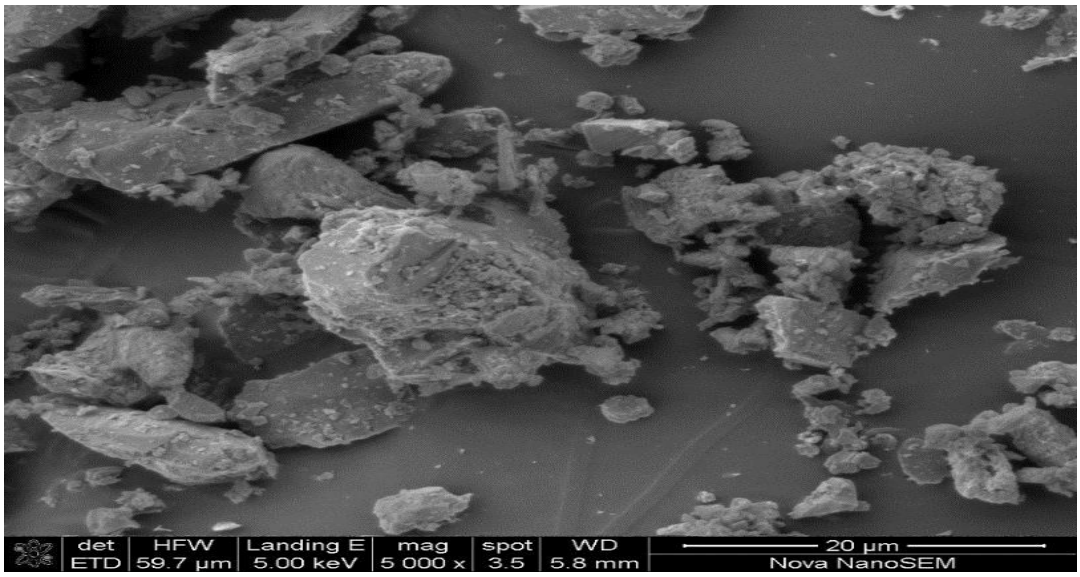

Figure 5.9 (d) The aggregate of loose particles embedded in the outer layer with Mg and Fe.

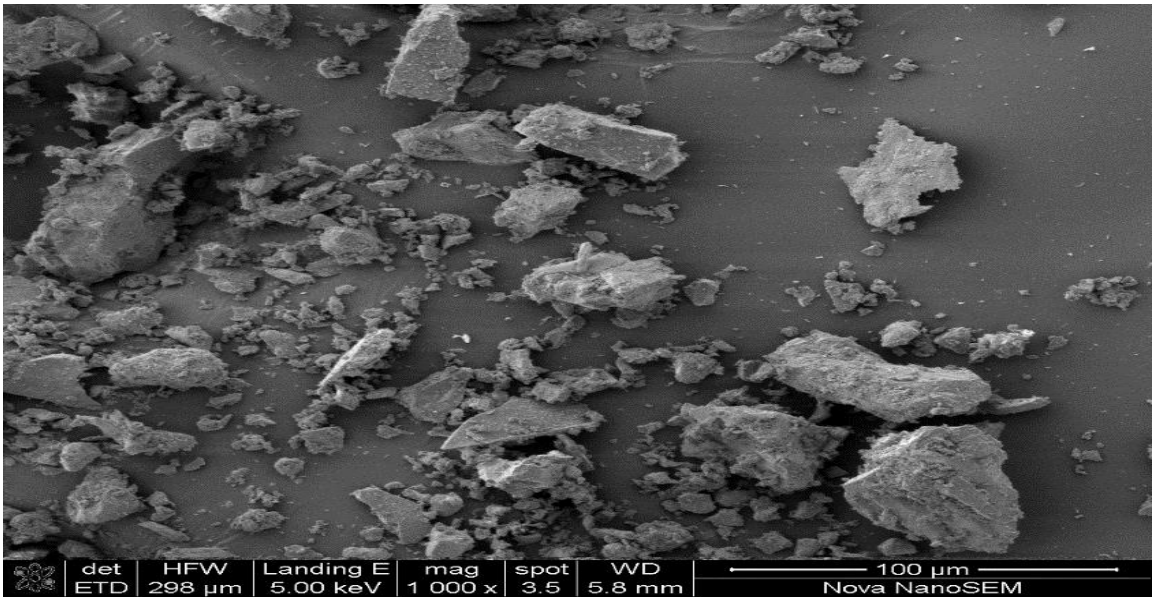

Figure 5.9 (e) reveals the magnifications of BP-1 particles shape that ranges from angular to sub-angular.

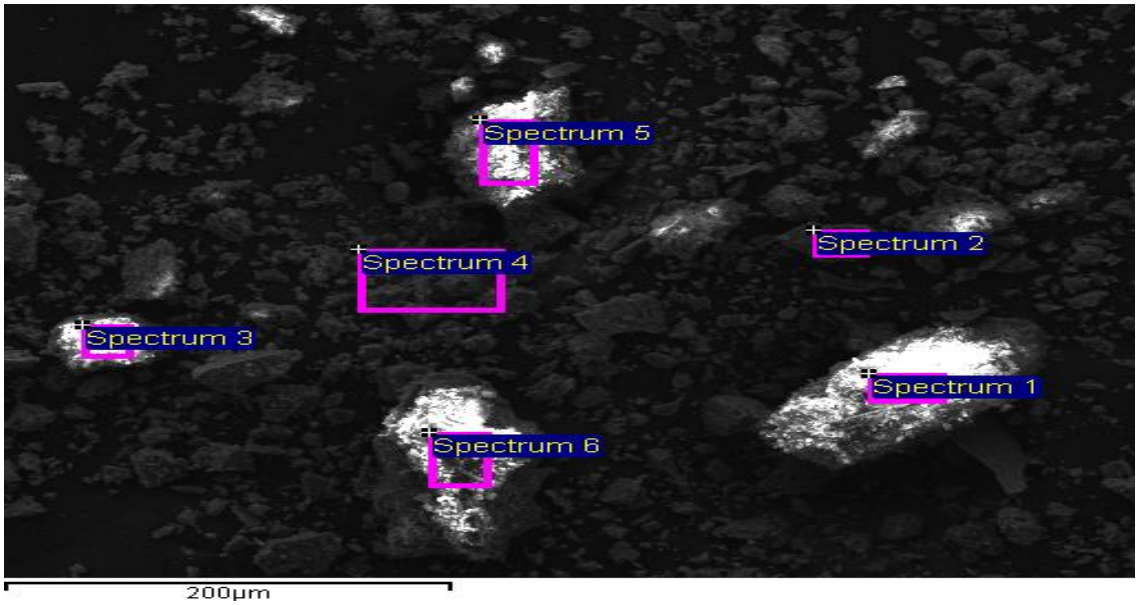

Figure 5.10 show the locations where elemental compositions listed in table 5.5 were measured

Table 5.5 Processing option: All elements analysed (Normalised) and weight in percentage

Spectrum		Major Element											
Spectrum	In stats.	C	O	Na	Mg	Al	Si	P	K	Ca	Ti	Fe	Total
Spectrum 1	Yes	11.95	54.93	5.12	0.33	7.23	15.2	0.6	1.94	2.17		0.55	100
Spectrum 2	Yes	9.17	42.38	2.53	2.9	4.99	14.9	0.9	1.08	2.96	2.2	16.1	100
Spectrum 3	Yes	11.43	53.14	3.23	0.36	8.18	18.5		2.04	2.59		0.54	100
Spectrum 4	Yes	43.68	40.98	1.04	1.3	2.49	6.22		0.38	2.1		1.82	100
Spectrum 5	Yes	24.92	46.34	2.35	0.47	5.51	12.4	0.9	0.85	4.87		1.48	100
Spectrum 6	Yes	10.88	55.34	5.31		8.04	17.6		1.24	1.6			100
Max.		43.68	55.34	5.31	2.9	8.18	18.5	0.9	2.04	4.87	2.2	16.1	
Min.		9.17	40.98	1.04	0.33	2.49	6.22	0.6	0.38	1.6	2.2	0.54	

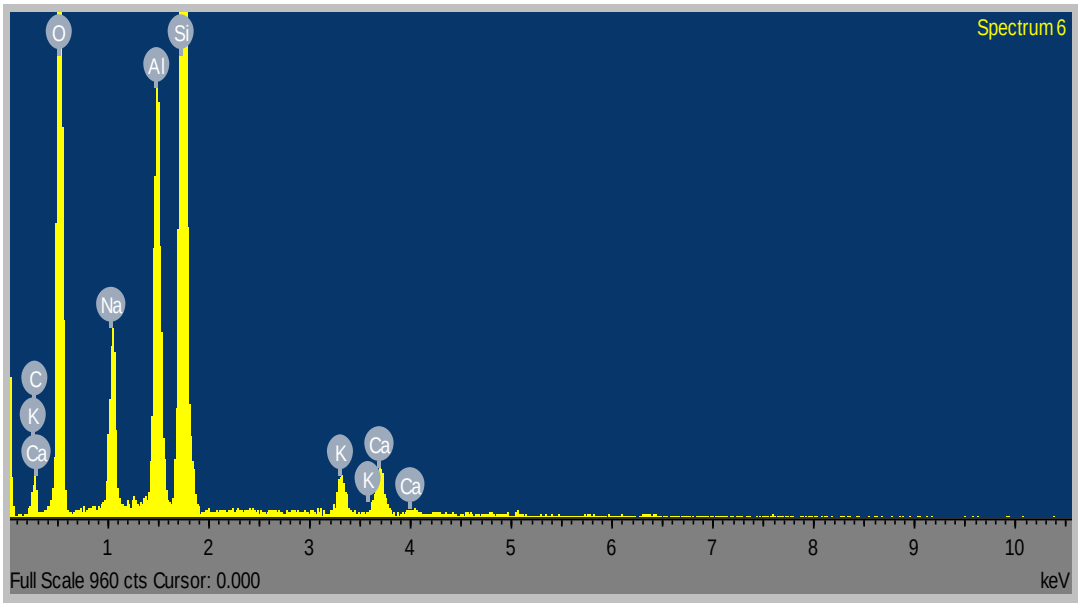

Figure 5.11 above shows the spectrum of BP-1 that contains six (6) major elements, Alkali-Earth metals, carbon, oxygen, Aluminium

5.5. Thermogravimetric Analysis (TGA)

Thermogravimetric Analysis (TGA) data for BP-1 reveals the minimum amount of weight loss of 1.47%, which was recorded at a temperature of 925^{0}C and is an indication

of evaporation of moisture that was absorbed when exposing the sample in the air at ambient temperature 23ºC.

A 0.5% weight gain was recorded due to the oxidation reaction of FeO compounds present in the BP-1simulant from XRF analysis, showing that the simulant is essentially thermally stable.

TGA data for the BP-1 could not show the minimum amount of weight loss recorded at a temperature of 678^0C indicating the evaporation of water molecules that had been absorbed while exposing the sample in the air at ambient temperature.

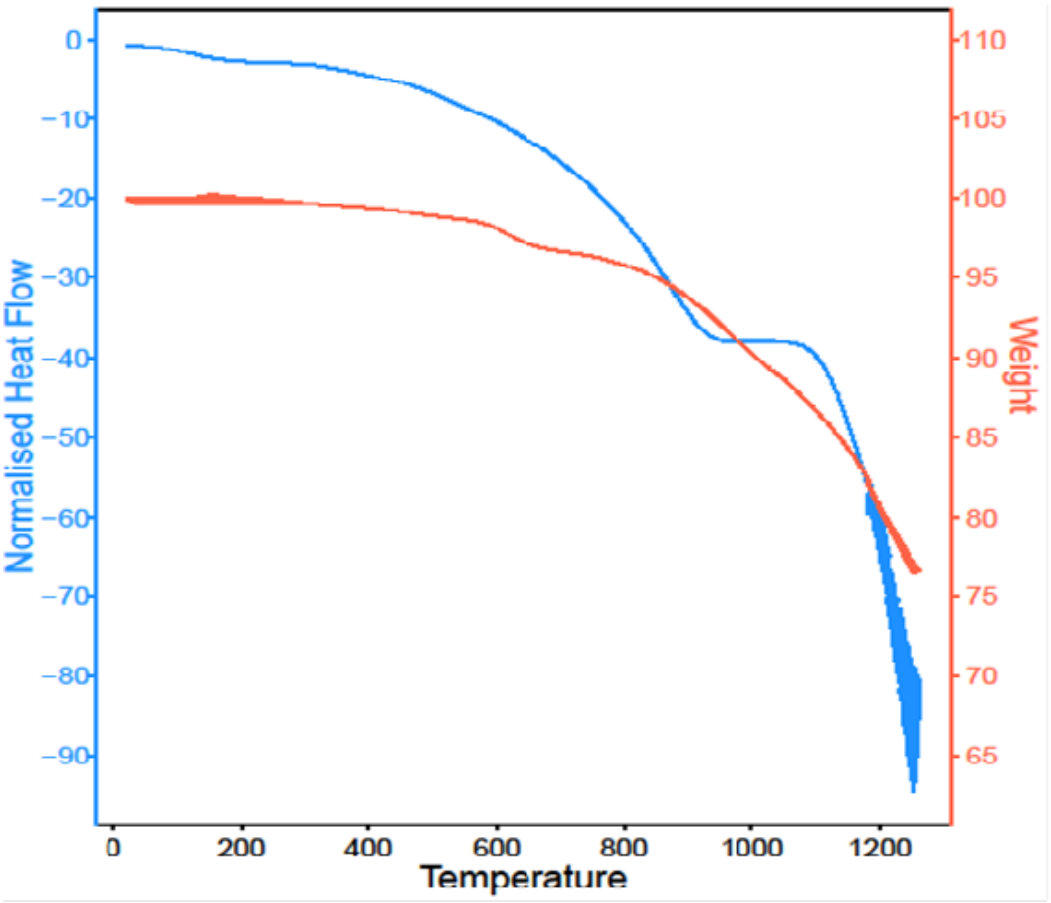

Figure 5.12 shows the heat flow and weight loss of sample at a high temperature.

Calorimeter data reveals the melting behaviour of BP-1 simulant over a range of thermal profile. The result shows both exothermic and endothermic behaviour of the simulant which is associated with a glass transition, phase transformation and melting over a range of temperature.

The BP-1 simulant shows a basaltic glass temperature of 804°C together with multiple endothermic peaks, indicating a melting temperature at 1179°C

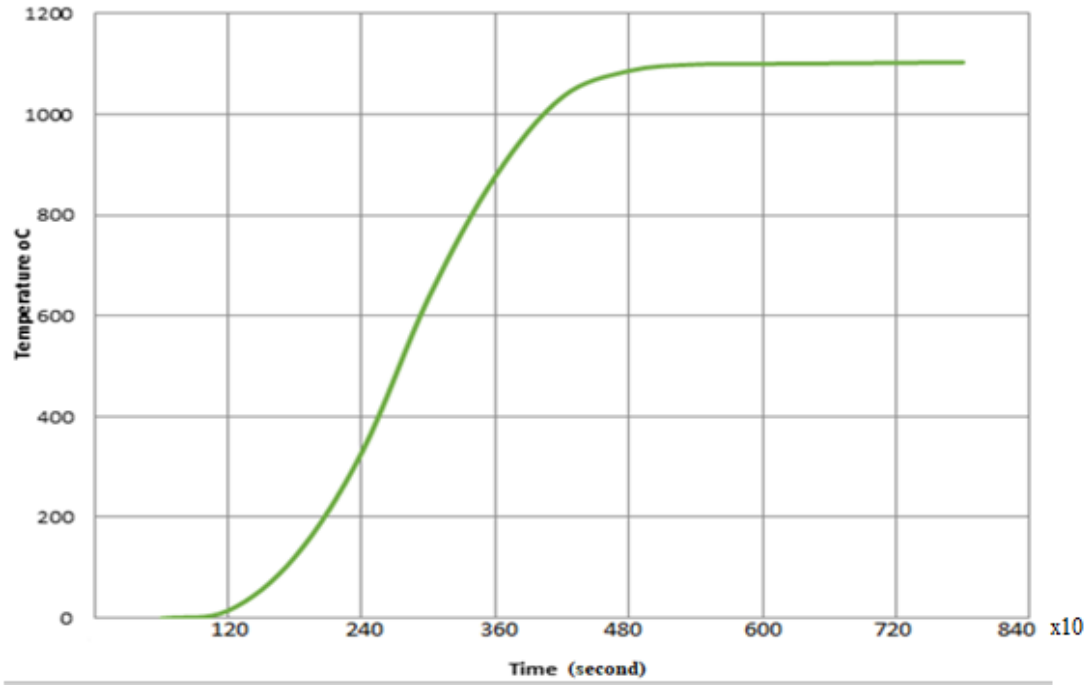

Figure 5.13 The sintering temperature profile for all the samples of BP-1 simulant at 1100°C for 90 minutes.

Table 5.6. Sintering Temperature profile for all the samples of BP-1 simulant at 1100°C for 90 minutes.

Powder size µm	Sintering Time min	Sintering Temperature °C
Unsieved	90	1100°C
212	90	1100°C
106	90	1100°C
38	90	1100°C

5.6 Glass Preparation

Results indicated from the table above shows that 0.14, 0.26, 0.48, and 0.21% of moisture content dried off at 110°C and is negligible. Thereafter the sample was heated to a temperature of 900°C to burn off the organic matter (shown in the above table). The latter test shows that the organic matter represents 1.71, 2.20, 2.41, and 2.59% respectively which is less than 3% by mass

Table 5.7 The dryness of moisture content and organic matter from the simple preparation of glass disc

Black Point -1 simulant

	Sample A(µm)	**B**	**C**		**D**			**E**	**F**		
	Grain size (µm)	Crucible	Crucible +sample	Weight (g) of samples	Dried at 110^0C Crucible +sample	Weight (g) of dry samples at 110^0C	% evaporation of samples at 110^0C	Heated-at 850-1100^0C Crucible +sample	Weight (g) of Dry sample at 900^0C	Weight(g) loss after at 900^0C	% evaporation of samples at 900^0C
2	212	20.69	22.76	2.07	22.76	2.07	0.14	22.73	2.04	0.04	1.71
3	106	20.13	22.19	2.07	22.19	2.06	0.26	22.15	2.02	0.04	2.20
4	38	20.04	22.05	2.01	22.05	2.00	0.48	22.01	1.96	0.05	2.41
5	Unsieved / As received	15.22	17.31	2.09	17.31	2.09	0.21	17.26	2.04	0.05	2.59

This result was compared with the investigation carried out on BP-1 simulant by Suescun-Florez *et al.* (2015) where 0.8% moisture content was evaporated at 105^0C, while 0.1% organic matter was burnt off at 400^{o}C

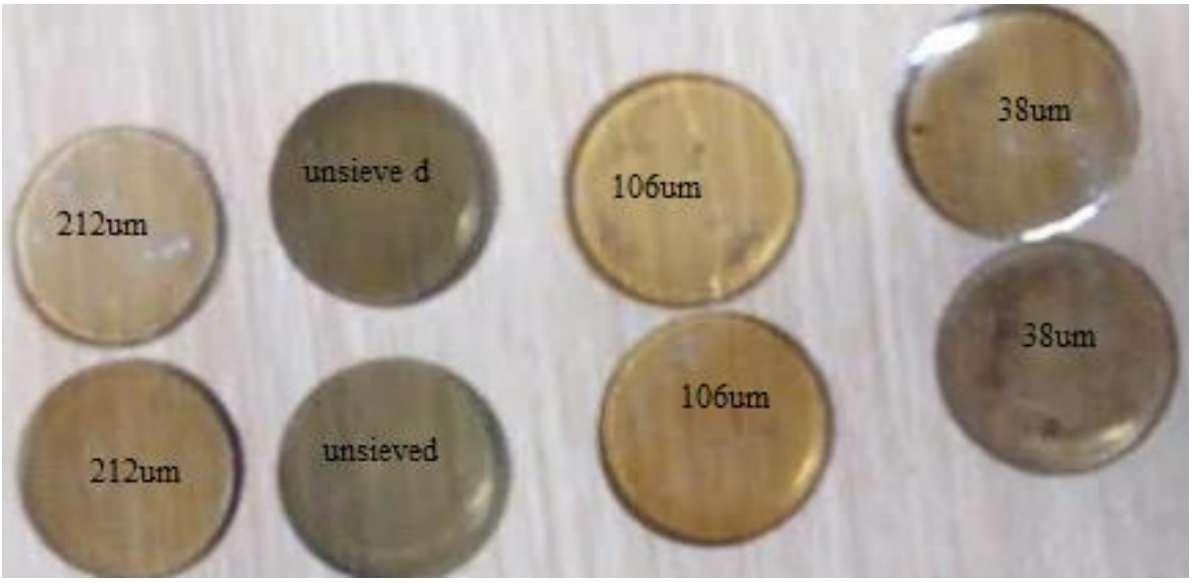

Figure 5.14 Sample of the glasses produced with BP-1 of different grain size.

The glass discs produced from the sample. The 38µm 106µm and unsieved samples underwent complete glass formation without any impurities. The 212µm sample had small impurities at the base. The unsieved and 212µm glass disc break when the cooling process was almost completed, this indicate an in-built energy was released at the compressive side of external surface of the glass during solidification simultaneously the centre portion of interior part of the glass experience cooling restriction; thus, leading to the effect of tension on the glass. The colour of the sample for low porosity 38 µm, and 106µm were transparent than 212µm while the unsieved shows a dark greenish colour.

5.7. Compression test Analysis

The dimensions of all the test pieces were measured before the compression tests were performed. Fig 5.16 below show the compression behaviour recorded for four samples of the 38µm sintered disks. Key points in the graph are labelled. Point W denoted the beginning of the test, where the initial load was applied. At this point the specimen was not yet firmly gripped in the test unit, so there was no measurable increase in the load as the face plates moved closer to one another. This stage represents the initial force required to hold the specimen in place. Point X is the stage where the specimen was firmly gripped in the test unit. Beyond this point, as the load increased. The sample was compressed. The sample showed a linear compression response

with increasing load until Point Y, at which failure occurs. Point Z denotes the stage at which the operator terminated the test. The failure loads for these four specimens ranges from 40kN to 60kN.

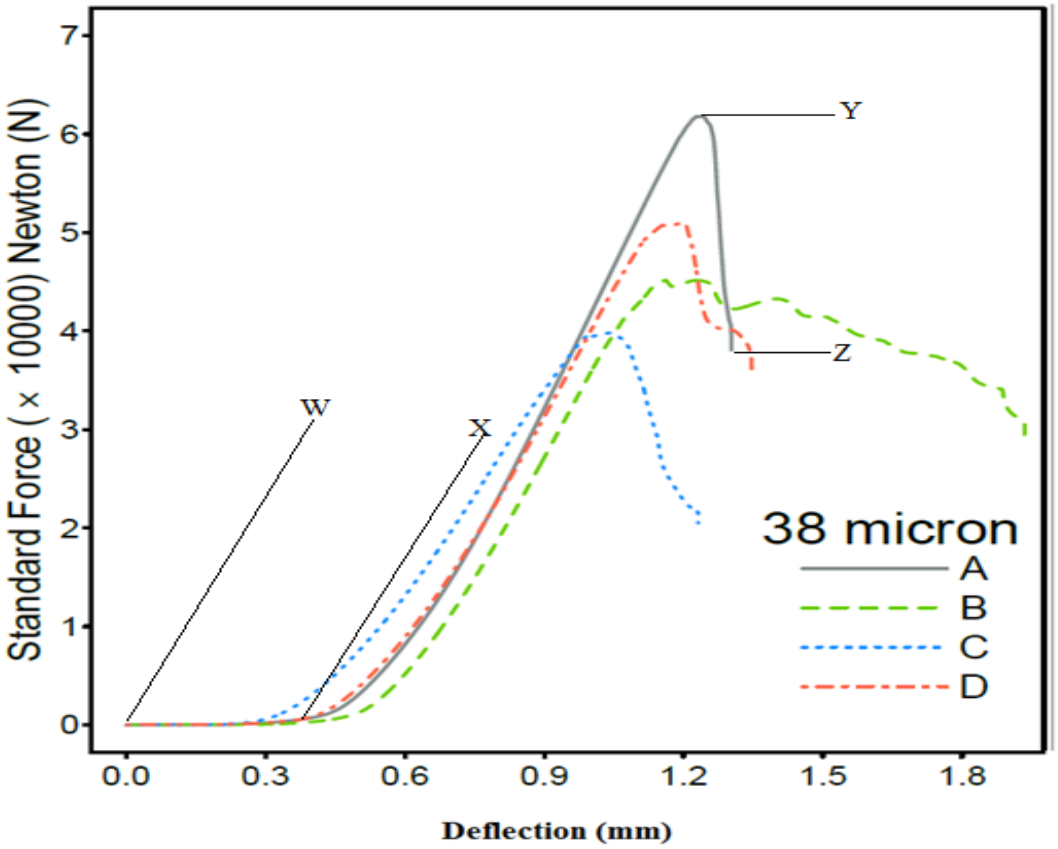

Figure 5.15 Load versus deflection recorded for four sintered disks of the 38µm sample grade while the remaining graphs are shown in the Appendix three (2).

The compression tests of the four sample grades allowed us to study the effects of porosity differences on the compression strength of the samples. The average maximum load for the low porosity (38 µm and 106 µm,) and high porosity (212µm and unsieved) were 49.78 ± 0.82kN, 45.51 ± 0.90 KN and 32.62 ± 0.95 KN, 44.02 ± 1.15 KN, respectively.

In previous published compression tests of sintered regolith simulants (e.g. JSC-1A (Indyk, and Benaroya, 2017), premature partial failure was observed in some specimens. We were curious to see whether our specimens would also display such premature failures. Out of the sixteen samples tested (samples A, B, C, D in each of the four sample grades), premature failures were observed only in sample B of the 38 µm grade, samples A and C of the 106 µm grade and sample B of the unsieved grade, while all other samples reached their maximum load without premature failure.

In addition, the average maximum pressure can be calculated from the loads and known dimensions of each sample and they are determined to be 66.14 ± 10.74 MPa, 60.47 ± 12.13 MPa, 43.74 ± 12.38 MPa, 58.52 ± 15.67 MPa.

Our results show that for the lowest porosity (38μm) and highest porosity (212 μm) was 66.14 ± 10.74 MPa and 43.74 ± 12.38 MPa respectively, which means a difference in compression strength of 22.4MPa and this implies that the lowest porosity can withstand a pressure three times higher than the highest porosity grade.

Table 5.8 Maximum failure loads and deflections for the four tests (A, B, C, D) conducted for each of the four different porosity grades.

Test(μm)	Load initial KN	Load 0.2 mm (KN)	Load initial failure	Load final x10KN	Deflection initial mm	Deflection mm	Deflection final(mm)
38A	0.00	0.00	0.00	61.8	0.00	0.00	1.24
38B	0.00	0.00	3.90	38.8	1.00	0.00	1.04
38C	0.00	0.00	0.00	51.0	0.00	0.00	1.02
38D	0.00	0.00	0.00	47.5	0.00	0.00	1.20
Mean	-	-	3.90	4.97	1.0	-	1.12
Variance	-	-	0	6.8	0.00	-	0.01
STD	-	-	0	8.2	0.00	-	0.10
106A	0.00	0.00	4.15	44.1	1.24	0.48	1.29
106B	0.00	0.00	0.00	60.0	0.00	0.00	1.21
106 C	0.00	0.00	2.70	39.8	1.00	0.00	1.09
106D	0.00	0.00	0.00	36.4	0.00	0.00	1.24
Mean	-	-	3.42	45.1	1.12	0.48	4.83
Variance	-	-	0.53	8.2	0.0144	0.00	13.13
STD	-	-	0.72	9.0	0.12	0.00	3.62
212A	0.00	0.00	0.00	28.3	0.00	0.00	1.00

212B	0.00	0.00	0.00	25.1	0.00	0.00	1.01
212C	0.00	0.00	0.00	28.2	0.00	0.00	0.98
212D	0.00	0.00	0.00	48.9	0.00	0.00	1.10
Mean	-	-	-	32.6	-	-	1.02
Variance	-	-	-	9.0	-	-	0.46
STD	-	-	-	9.4	-	-	0.46
Unsieved A	0.00	0.00	0.00	41.9	0.00	0.00	1.23
Unsieved B	0.00	0.00	3.91	41.4	0.90	0.00	1.02
Unsieved C	0.00	0.00	0.00	30.5	0.00	0.00	1.08
Unsieved D	0.00	0.00	0.00	62.3	0.00	0.00	1.24
Mean	-	-	3.91	44.0	0.9	-	1.14
Variance	-	-	0.00	13.2	0.00	-	0.01
STD	-	-	0.00	11.5	0.00	-	0.10

5.8 Stress, Strain and Modulus of Elasticity

Stress-strain tests are of great value to any engineering materials because such tests measure the physical properties of materials and give information about their behaviour during the service condition or operation. The stress is a measure of how much force an object experiences in a given area, while strain is a measure of the amount of a material that can be stretched or compressed. It is usually determined by calculating the change in length of the original length and its unit is dimensionless, hence through this medium ductility and plasticity of materials can be measured.

However, during the investigation, the sample produced experience slight changes therefore, a little deformation on the specimen will produce small deflection. When tested, no measurement was recorded in the cross-sectional area which was minimal. Similarly, to this engineering stress-strain is the Elastic modulus which defines stiffness of materials or measures the

resistance of materials against elastic deformation. The modulus of elasticity can be calculated from the engineering stress-strain equation.

$$\sigma A = F \quad (4)$$

$$\varepsilon = \frac{\Delta L}{L} \quad (5)$$

$$\sigma = E\varepsilon \quad (6)$$

Stress σ , Area A, Force F, length L and Modulus of elasticity E.

The stress-strain for the duration of the test was calculated for each sample while the average dimensions were measured before the testing was conducted at the initial lengths. The graph for each test was plotted

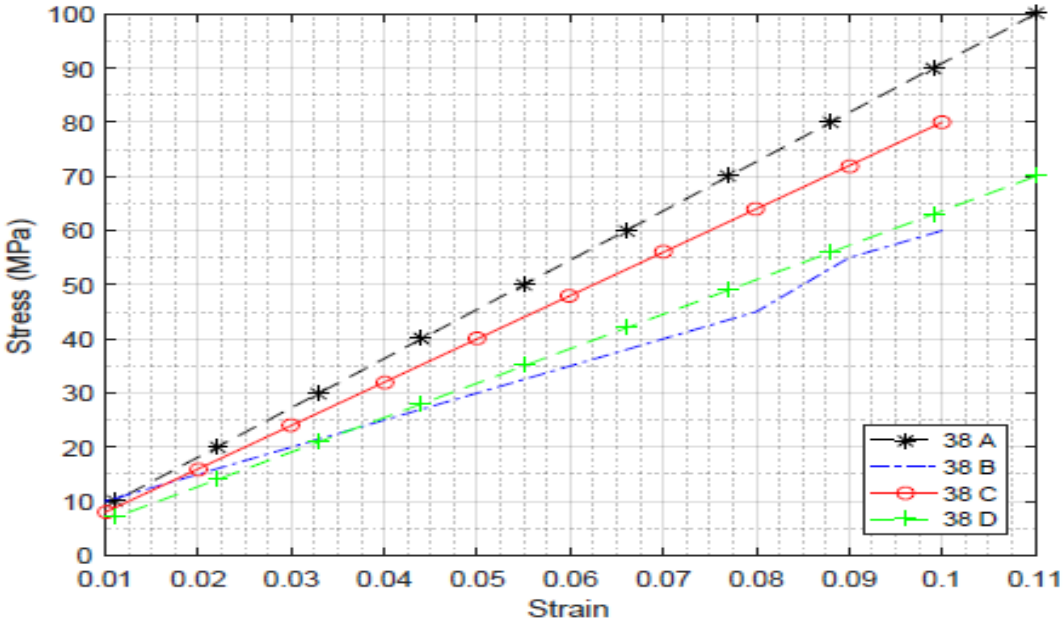

Figure 5.16 shows the stress-strain graph for the lowest porosity (38µm) test sample.

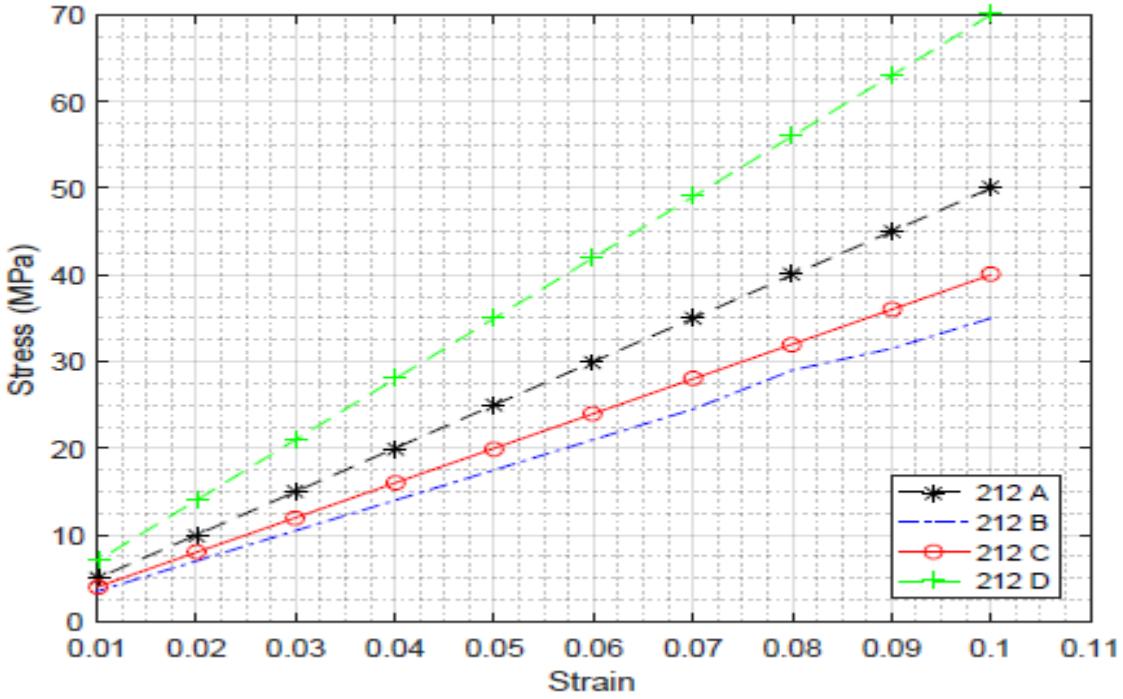

Figure 5.17 shows the stress-strain graph for the lowest porosity (212 µm) test sample while the remaining graphs are shown in the Appendix 3.

Several tests reached the local maximum compressive strength while the elastic modulus was computed for each sample from the slope of the stress-strain graph using the MATLAB. However, maximum failure was used to obtain the best-fit linear equation as shown in the table below.

Table 5.9 reveals the description of particle grain size of compressed samples.

Porosity(µm)	Description
Lowest porosity **38 µm**	This grade has significantly different behaviour than the porosity grades because it compressed much quicker making it denser than the other porosity grades. Based on this, it displays a denser packing arrangement of grains contact per unit volume. In addition, the bulk density increased due to large contact area of grains particles per unit volume which subsequently leads to increase in cohesion force and frictional resistance. Hence, it became mechanically the strongest among other grades after compression over a given time.

Low porosity **106 µm**	This sample compressed more and faster than the 212 µm and unsieved grades, but less than the 38µm grade. It was mechanically stronger the 212µm and unsieved grades after compression in the mould. It also displayed higher shear strength than the 212 µm and unsieved samples.
Highest Porosity **212 µm**	When the 212µm was compared to another particles size it did not appear to be stronger. This shows that it has lesser strength in a given bulk density. Therefore, the grains were not fully compressed due to large grain size in this sample. This shows that the 212 µm grains are mechanically weakest of all the sieved grades.
Medium porosity **unsieved**	The unsieved grade compressed quicker making it denser than the 212 µm grade and less dense than the 38 µm and 106 µm grades because of less packing arrangement of grains contacts per unit volume because of large grains of 212µm present in the feedstocks. This shows that its grains are mechanically weaker when compressed.

Table 5.10 The stress versus strain linear equations for each test carried out on the samples of different porosity

Porosity (µm)		Equation
Lowest **38**	A	Y= 909.09x 3.56 x 10^{14}
	B	Y= 548.48x +3.33
	C	Y= 800x
	D	Y= 636.36x – 7.12 x 10^{14}
Low **106**	A	Y= 636.36 x – 7.12 x 10^{14}
	B	Y=958.58x +0.21
	C	Y= 548.485x + 3.3

	D	Y= 456.78x + 0.28
Medium	A	Y= 457.07x + 3.33
Unsieved	B	Y= 548.48x + 3.33
	C	Y= 500x
	D	Y= 833x - 5.98x 10^{14}
Highest	A	Y = 500x
212	B	Y= 353x – 0.0667
	C	Y= 400x
	D	Y= 700x – 2.1532x 10^{14}

A plot of the best fit line of each test can be found in the Appendix A1 and the result of the slope from each set of the stress-strain linear equation was averaged and a standard deviation was calculated (Table 5.11). The Young's modulus for the lowest porosity grade was estimated to be 723.48 ± 105MPas, low porosity 650.05 ± 189MPa, high porosity 488.25 ±133MPa, highest porosity 584.64 ±147MPa.

5.9 Toughness

In addition, other mechanical properties can also be determined from the stress-strain graph such as toughness and this can be estimated at the area curves of the stress-strain diagram. The ability of a material to resist fracture or absorb energy when plastically deformed is due to the combination of strength and ductility, this property is essential when designed structural components. The toughness can be calculated by integrating the area under the stress-strain curves.

$$\int_0^x \sigma d\varepsilon = \frac{\text{Energy}}{\text{volume}} \qquad 7$$

$$\varepsilon - \text{ strain}, \qquad \sigma - \text{ stress}$$

The integration of this test was performed numerically via the trapezoid methods of MATLAB with the trapezium and the plot was shown in appendix.

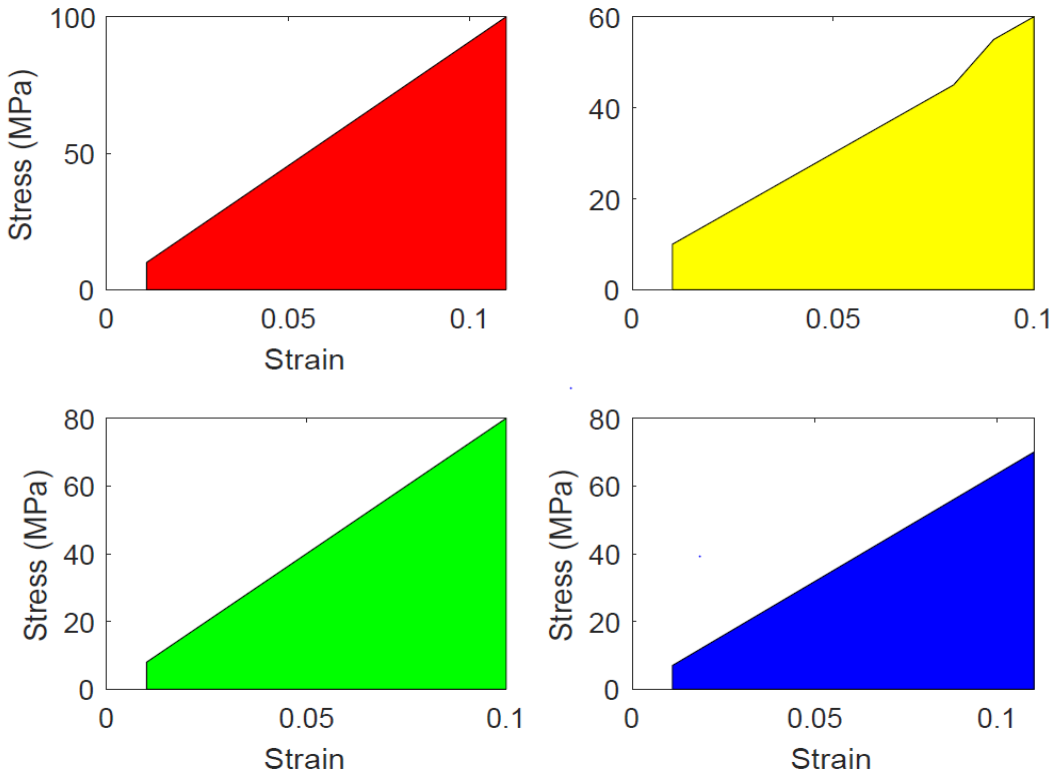

Figure 5.18 shows the area under the stress-strain curve for the lowest porosity 38µm graph was calculated with numerical integration to determine the toughness of the material.

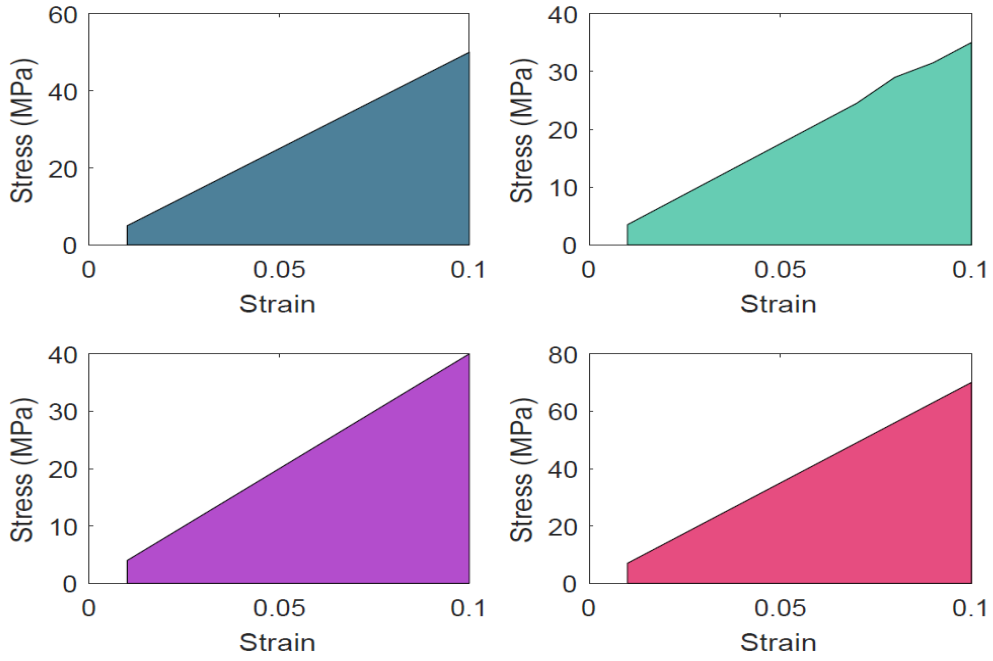

Figure 5.19 shows the area under the stress-strain curve for the highest porosity 212µm while the remaining graphs can be found in Appendix four (4).

Table 5.11 shows the comparison of calculated toughness for each sample.

Porosity (µm)	Toughness	
	Test	MJ/m^3
Lowest	A	5.44
38	B	3.00
	C	3.96
	D	3.81
Mean		4.05
STD		0.88
Low	A	3.81
106	B	5.94
	C	3.00
	D	2.71
Mean		3.87
STD		1.26
	A	2.47
Highest	B	1.74
212	C	1.98
	D	3.46
Mean		3.22
STD		1.04
	A	3.60
High Unsieved	B	3.00
	C	2.47
	D	5.15

Mean		3.56
STD		1.00

5.10 Compressive strength

Compressive strength is defined as the maximum stress that a solid material can withstand under a uniaxial (applied) load without fracture and is usually estimated as the ratio of maximum load to original cross-section area of a sample being investigated in a compression test. Some materials experience fracture at the limit of their compressive strength while others deformed irreversibly, therefore, it becomes a key value for structural designs. Table 5.13 shows the compressive strengths measured in the tests.

It is instructive to compare the compressive strength of the four porosity grades investigated in the present study with the compressive strength of common terrestrial construction materials (Table 5.14).

Table 5.12 shows the compressive strength of the entire specimen tested at initial failure and maximum failure.

Porosity		**Compressive Strength**			
		Initial failure (MPa)	Initial failure (psi)	Maximum failure (MPa)	Maximum failure (psi)
Lowest porosity	38 µm Mean			66.14	9,593
				115..35	16,723
	Variance			10.74	1,558
	STD				
Low Porosity	106µm Mean	47.06	6,825	60.47	8,770
		256.32	37,173	147.14	21,335

	Variance STD	16. 01	2,322	12.13	1,759
Highest Porosity	212 µm Mean Variance STD			43.74	6,344
				153.26	22,234
				12.38	1,796
High Porosity	Unsieved Mean Variance STD			58.52	8,488

Table 5.13 shows the compressive strength required for concrete structural members used in terrestrial construction**.**

Types or location of concrete construction	Specified compressive strength, (MPa)
Concrete fill	< 14
Basement and foundation walls and slabs, walks, patios, steps and stairs	17-24
Driveways, garage and industrial floor slabs	21-28
Reinforced concrete beams, slabs, columns and walls	21-48

Precast and prestressed concrete	27-48
High-rise buildings(columns)	69-103

Table 5.14 shows the tensile strength and compressive strength values for both lunar concrete and terrestrial concrete.

Structural Member	Tensile strength		Compressive strength	
	MPa	(psi)	MPa	(psi)
Lunar sulphur [1]Concrete	-	-	31	4,500
[2]Lunar Concrete	8.3	1,200	74	10,000
[3]Terrestrial Concrete (residential)	-	-	17	2,500
[3]Terrestrial concrete (commercial)	-	-	28	4,000
[3]Terrestrial Concrete (high strength)	-	-	70	10,000

[1]Husam and Mohsen, 1994, Lin[2] National[3] Adapted from Advances in Manufacture of Moon Crete a review by Markandeya Raju Ponnada et al., 2014.

The comparisons among the tables 5.12, 5.13 and 5.14 for compressive strength of test piece, terrestrial structures and lunar concrete respectively can be made. The sample set of the lowest porosity has a high range of compressive strength (38µm) 66.16 MPa (9,59psi) is twice that of (a) lunar sulphur concrete and (b)Terrestrial commercial

concrete and four times the terrestrial residential concrete. In addition, it can be used for reinforced concrete beams, slabs, column and walls as well as precast and pre-stressed concrete.

Furthermore, if all else is equal, and an individual sample test was considered, the sample 38A (Table 5.0) with a compressive strength of 81.87MPa (11,87psi) will be suited for high rise buildings (columns). However, the tensile strength was not conducted since the material is a ceramic product and this is liable to break because of its high fragility. Therefore, the sample must be reinforced before it can be used for tensile strength. Hence, further research needs to be conducted. Our results suggest that sintered lunar regolith could meet the functional requirement for lunar structures.

5.11 Bulk Modulus

Bulk Modulus is a measure of resistance of a material to a uniform compression There will be change in a volumetric strain during compression in all sides

It is a ratio of a confine pressure to the volumetric strain

$$\text{Bulk Modulus K} = \frac{\text{Pressure}}{\text{Volumetric Strain } \varepsilon V} = \frac{P}{V0-Vn/V0} \quad = K = -\frac{P}{\varepsilon V} \qquad 8$$

Table 5.15 shows the average values of bulk modulus, means and standard deviation.

Porosity		**Bulk Modulus**
Lowest Porosity		Maximum Failure (MPa)
38µm	Mean	732.51
	STD	95.30
Low Porosity	Mean	614.27
106µm	STD	126.97
Highest Porosity	Mean	496.35
212µm	STD	108.68
High Porosity	Mean	567.30
unsieved	STD	129.33

In this research the bulk modulus was calculated from the applied pressure (as earlier determined) to the sample and an equation that relates the measured diameter and the

engineering strains from maximum deflection of each sample were computed as shown in Table 5.16 above.

The bulk modulus obtained from this research assumes the diameter almost remains the same throughout the experiment except for the changes that occurred in the height of the sample thereby, causing the changes in volumetric strain.

The lowest porosity exhibited the largest bulk modulus at the maximum failure while the highest porosity experienced the lowest bulk modulus, and this shows that porosity is one of the factors affecting a sintered lunar simulant. Therefore, adequate knowledge of loads and materials properties like bulk modulus will help the structural engineer in the design and structural analysis of lunar habitats.

5.12 Poisson's Ratio

Poisson's ratio is the ratio of the transverse to the longitudinal strain and it occurs when a material is subjected to axial stress within the elastic range and is very useful when considering a linear isotropic elastic homogeneous solid and in the study of the behaviour of material properties and in the design of a structural member. However, the structural material being investigated here is an isotropic material where Poisson's ratio (have a minus sign) is relevant especially in determine the elastic properties while the Young's modulus takes preeminent therefore it is practically useful in the lunar environment for construction and design of bridge, lava tube, and crater tunnel etc.

$\upsilon = \frac{(3K - 2G)}{6k+2G}$	9
$E = 2G\ (1 + \upsilon).$	10
$E = 3K\ (1 - 2\ \upsilon).$	11
$\frac{K}{2G} = \frac{2(1 - \upsilon)}{3(1-2\upsilon)}$	12

Poison ratio (υ), Young's modulus(E) and Bulk Modulus (K), and shear modulus (G).

5.13 Shear Modulus

The modulus of rigidity or shear modulus (G) is a measure of resistance of a material to shearing forces; it is a ratio of shear stress to shear strain.

The structural material been investigated is isotropic materials and it has elastic properties and is independent of any direction, therefore it is practically useful in the lunar environment.

Table 5.16 shows a computed Poisson ratio, bulk modulus and shear modulus and stiffness ratio (K/G).

Grain size µm	Poisson's Ratio	Young's Modulus (E) MPa	Bulk Modulus (K) Maximum (MPa)	Shear Modulus (G)	Stiffness ratio K/G
Lowest Porosity (38µm)	0.33	723.48	732.508	272	2.693
Low Porosity (106 µm)	0.32	650.05	614.27	245	2.507
Highest Porosity (212 µm)	0.34	488.25	496. 349	182	2.727
High Porosity Unsieved	0.33	584.64	567. 305	220	2.579

CHAPTER SIX CONCLUSION AND FUTURE WORK

The main aim of this thesis was to investigate the potential utilization of lunar in situ resources for construction and manufacturing which will also allow for large-scale production of structural components on the moon. From the review of literature, it was identified that the use of in-situ resources is more viable in terms of cost and risk effectiveness, for construction and physical development in the lunar environment.

We approached the problem by using a the regolith simulant BP-1 for geotechnical and mechanical properties through quantifying the materials properties of sintered lunar simulant as an analogue material to real sintered lunar regolith.

Various analyses were carried out to determine the geotechnical and mechanical characteristics of the regolith simulant BP-1 used for this research. BP-1 reveals the minimum amount of weight loss 1.47% which was recorded at a temperature of 925^{o}C and an indication of evaporation of moisture that was absorbed when exposing the sample in the air at ambient temperature. A 0.5% weight gain was recorded due to the oxidation reaction of FeO compounds present in the BP-1 simulant from XRF analysis showing that the simulant is thermally stable. Calorimetry results show both exothermic and endothermic behaviour of the simulant over a range of temperatures, which is associated with a glass transition, phase transformation and eventual melting. The BP-1 simulant shows a basaltic glass temperature 804^{o}C together with multiple endothermic peaks, indicating a melting temperature at 1179^{o}C.

In order to study the effects of porosity, we sieved the material to produce four porosity grades, 38 µm,106 µm, 212 µm and unsieved. In terms of grain size, there were few differences observed in each of these specimens, the finest grain size was recorded for the lowest porosity samples, 38 µm, 106 µm, and unsieved, while the largest grain 212µm remained coarse. The particle size distribution reveals how well a soil is graded in bulk of soil mass and this will help in soil classification. Based on this information the suitability of the soil for road construction can be determined, while assessment of permeability can be carried out. The particles shape does affect the soil shear strength while the soil gradation and grain size affect the shear resistance e.g. the angular grains would provide adequate interlocking thereby increase the shear strength of the soil The analysis results presented in chapter 4 showed that the BP-1 simulant has both in compositional and geotechnical properties resembling the lunar soil samples returned by the Apollo 17 mission and thus can be used for construction of lunar structural habitat.

Given that we determined the melting point of BP-1 is 1179^{o}C, we sintered the samples at 1100^{o}C for one hour. The sintered specimens were then subjected to compression testing. There were four different values of average compressive strength of the porosity materials ranging from lowest to highest porosity corresponding to the smallest to largest average grain sizes of 38 µm, 106 µm, unsieved and 212µm and they were 66.14MPa, 60.47MPa, 58.52MPa, 42.74 MPa, respectively. Additional material properties were also examined which includes stress-strain, toughness, bulk modulus, compressive strength and Poisson ratio.

In summary, this work carried out on BP-1 simulant has shown it to be consistent with the attributes and mechanical performance of real lunar regolith and other regolith simulants.

Further research can be carried out on samples tested in this research to investigate the effect of sintering time on material properties and to improve strength and the cost effectiveness of better production. Our investigations considered only compressive loading. Further investigation could be carried out for reinforcing the sintered lunar material so that it can be applied for tensile loading.

Future Outlook

Recently, various concepts have been investigated in the context of building the Moon Village using ISRU. Regarding this, laser sintering, microwave sintering, contour crafting and powder binder bond printing etc. are among the most investigated additive manufacturing techniques.

The manufacturing of sintered structural components investigated in this research could be carried out with an autonomous lunar rover that contains a built-in sieve to grade the regolith to desired porosity, a press to make the powder compact, and a furnace to sinter the compacts (Fig. 6.1).

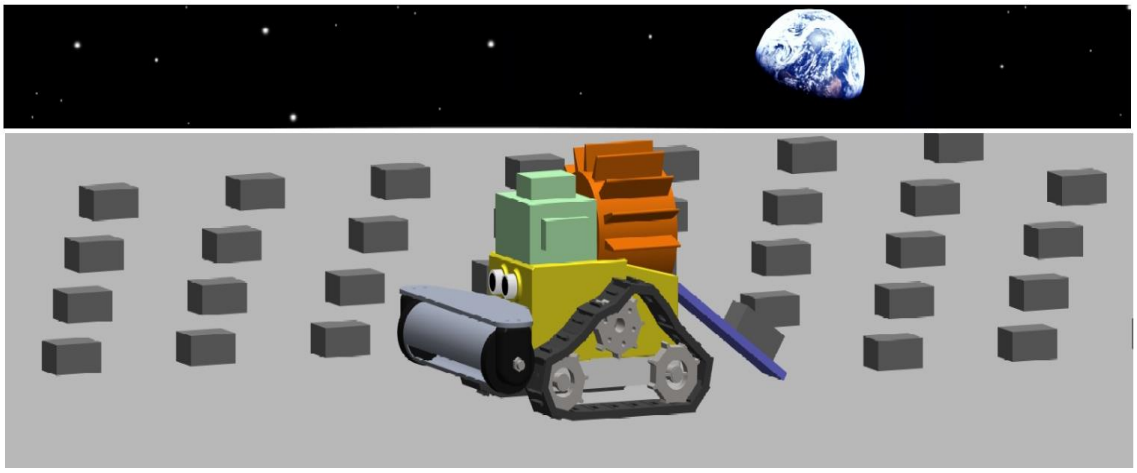

Figure 6.1 above shown a lunar rover that can produce sintered structural components.

The lunar regolith would be scooped up off the lunar surface as the rover moves across the landscape. Once sieved, will be conveyed into the compaction chamber where it will be compacted (under a uniaxial press) to form green compact before being sintered at a high temperature. The high temperature for sintering could either be provided by an on-board nuclear power source, or by a large solar concentrator. The advantage of having a nuclear power source would be that the rover could continue its operations during the local lunar night time. Such an autonomous rover could begin making the building blocks for a future lunar settlement even before human astronauts arrive at the location of the settlement, so that a habitat could be rapidly constructed from the already finished building blocks awaiting the arrival of astronauts or other autonomous construction vehicles.

REFERENCES

Morris A, (2017) New Method for 3D Printing Extraterrestrial Materials, Engineering News. Available at: https://www.mccormick.northwestern.edu/news/articles/2017/04/new-method-for-3d-printing-extraterrestrial-materials.html.

Avchare, K. R. *et al.* (2014) 'Space manufacturing Techniques', 4(4), pp. 1–10.

Balla, V. K. *et al.* (2015) 'First demonstration on direct laser fabrication of lunar regolith parts'. doi: 10.1108/13552541211271992.

Benaroya, H., Bernold, L. and Chua, K. (2002) 'Engineering, design and construction of lunar bases', ... *of Aerospace Engineering*, (April), pp. 33–45. doi: 10.1061/(ASCE)0893-1321(2002)15:2(33).

Cardiff, E. H. and Hall, B. C. (2008) 'A dust mitigation vehicle utilizing direct solar heating', Joint Annual Meeting of Lunar Exploration Analysis Group-International Conf. on Exploration and Utilization of the Moon-Space Resources Roundtable, (Dmv).

Cole D.M., Taylor L.A., Y. L. and M. A. H. (2010) 'Grain-scale mechanical properties of lunar plagioclase and its simulant: Initial experimental findings and modeling implications. D.M.', *Earth and Space 2010: Engineering, Science, Construction, and Operations in Challenging Environments © 2010 ASCE*, pp. 74–83.

Davis, G., Montes, C. and Eklund, S. (2017) 'Preparation of lunar regolith based geopolymer cement under heat and vacuum', *Advances in Space Research*, 59(7), pp. 1872–1885. doi: 10.1016/j.asr.2017.01.024.

Derlet, P. M. (2017) 'Sintering theory'. Available at: https://lmc.epfl.ch/wp-content/uploads/2018/06/PowderTech-11.pdf.

Faierson, E. J. *et al.* (2010) 'Demonstration of concept for fabrication of lunar physical assets utilizing lunar regolith simulant and a geothermite reaction', *Acta Astronautica*, 67(1–2), pp. 38–45. doi: 10.1016/j.actaastro.2009.12.006.

Fateri, M. *et al.* (2014) 'Experimental investigation on Selective Laser Melting of glass', *Physics Procedia*, 56(C), pp. 357–364. doi: 10.1016/j.phpro.2014.08.118.

Fateri, M., Meurisse, A. and Sperl, M. (2017) 'Solar sintering for additive manufacturing on the Moon', *EPSC Abstracts*, 11(EPSC2017-475–1). Available at: https://meetingorganizer.copernicus.org/EPSC2017/EPSC2017-475-1.pdf.

German, R. M. (2013) ‘History of sintering: empirical phase’, Powder Metallurgy, 56(2), pp. 117–123. doi: 10.1179/1743290112Y.0000000025.

Goulas, A. *et al.* (2016) ‘Investigating the additive manufacture of extra-terrestrial materials’, (November).

Greg Sadlier (2016) ‘Economic impacts of an international lunar exploration endeavour’. Available at: https://www.slideshare.net/Stellvia/economic-impacts-of-an-international-lunar-exploration-endeavour.

Grugel, R. N. and Toutanji, H. (2008) ‘Sulfur “concrete” for lunar applications - Sublimation concerns’, *Advances in Space Research*, 41(1), pp. 103–112. doi: 10.1016/j.asr.2007.08.018.

Indyk, S. J. and Benaroya, H. (2017) ‘A structural assessment of unrefined sintered lunar regolith simulant’, *Acta Astronautica*, 140(April), pp. 517–536. Available at: https://www.sciencedirect.com/science/article/pii/S0094576517305404.

Introduction, B. and Olevsky, E. A. (2011) ‘Sintering Theory’.

Jiang, M., Li, L. and Yang, Q. (2013) ‘Experimental investigation on deformation behavior of TJ-1 lunar soil simulant subjected to principal stress rotation’, Advances in Space Research, 52(1), pp. 136–146. doi: 10.1016/j.asr.2013.02.001.

Johnson, J. L. (2010) ‘Sintering of refractory metals’, Sintering of Advanced Materials. Woodhead Publishing, pp. 356–388. doi: 10.1533/9781845699949.3.356.

Kodikara, J. T. I. A. S. (2019) ‘Review of soil compaction: History and recent developments’, *Elsievier*, pp. 1–11.

Küppers, M. and Vincent, J. (2011) ‘Impacts and formation of regolith’.

Laila A. Rahmatian1, 2 and Philip T. Metzger, P. D. . and 1School (2010) ‘Soil Test Apparatus for Lunar Surfaces’, *Earth and Space 2010*, pp. 239–253.

Mckay, D. S. *et al.* (1994) ‘JSC-1 : A New Lunar Soil Simulant’, pp. 857–866.

Meurisse, A. *et al.* (2018) ‘Solar 3D printing of lunar regolith’, *Acta Astronautica*, 152(June), pp. 800–810.

Miriam Kramer (2014) The Future of Moon Exploration, Lunar Colonies and Humanity, Spaceflight. Available at: https://www.space.com/26584-future-of-moon-exploration.html (Accessed: 23 March 2018).

Mpagazehe, J. N. *et al.* (2014) ‘An experimental study of lunar dust erosive wear potential using the JSC-1AF lunar dust simulant’, *Wear*, 316(1–2), pp. 79–91. doi: 10.1016/j.wear.2014.04.018.

Mueller, R. P. *et al.* (2018) ‘Additive Construction using Basalt Regolith Fines’.

Oravec, H. A., Zeng, X. and Asnani, V. M. (2010) ‘Design and characterization of GRC-1: A soil for lunar terramechanics testing in Earth-ambient conditions’, *Journal of Terramechanics*, 47(6), pp. 361–377. doi: 10.1016/j.jterra.2010.04.006.

Peter Christoforou (2014) The Moon: Past, Present and the Future. Available at: http://www.astronomytrek.com/the-moon-past-present-and-the-future/.

Reis, S. (2014) ‘Characterization and Glass Formation of JSC1 Lunar and Martian Soil ¨ ssbauer and EPR spectra for glasses and glass-ceramics prepared from simulated compositions of Lunar and Martian soils’, (August). doi: 10.1063/1.2845057.

Ruess, F., Schaenzlin, J. and Benaroya, H. (2006) ‘Structural Design of a Lunar Habitat’, *Journal of Aerospace Engineering*, 19(3), pp. 133–157. doi: 10.1061/(ASCE)0893-1321(2006)19:3(133).

Satyendra (2013) *Factors Influencing Sintering Process*. Available at: http://ispatguru.com/factors-influencing-sintering-process/.

Sibille, L. *et al.* (2006) ‘Lunar Regolith Simulant Materials: Recommendations for Standardization, Production, and Usage’, *NASA Technical Paper*, (September 2006), p. 118. doi: 10.4028/www.scientific.net/AMM.419.67.

Sibille, L. (2013) ‘Lunar Simulants, Analogues, and Standards: Needs and Realities for Mission Technologies Development’, p. 28.

Soil Compaction Theory Compaction (no date). Available at: ttps://bmsit.ac.in/system/study_materials/documents/000/000/022/original/compaction.pdf?1477115557.

Spudis, P. D. (2011) ‘The Moon: Point of Entry to Cislunar Space’, *Toward a theory of spacepower: Selected essays*, pp. 241–251.

Stoeser, D. B., Wilson, S. A. and Rickman, D. L. (2010) ‘Preliminary Geological Findings on the BP-1 Simulant’, *Nasa Tm*, (2010–216444), p. 24p.

Suescun-Florez, E. *et al.* (2015) 'Geotechnical Properties of BP-1 Lunar Regolith Simulant', *Journal of Aerospace Engineering*, 28(5), p. 04014124. doi: 10.1061/(ASCE)AS.1943-5525.0000462.

Taylor, L. A. *et al.* (2001) 'Lunar mare soils: Space weathering and the major effects of surface-correlated nanophase Fe', *Journal of Geophysical Research E: Planets*, 106(E11), pp. 27985–27999. doi: 10.1029/2000JE001402.

Wilhelm, S. and Curbach, M. (2014) 'Review of possible mineral materials and production techniques for a building material on the moon', *Structural Concrete*, 15(3), pp. 419–428. doi: 10.1002/suco.201300088.

Zheng, Y. *et al.* (2009) 'CAS-1 lunar soil simulant', *Advances in Space Research*. COSPAR, 43(3), pp. 448–454. doi: 10.1016/j.asr.2008.07.006.

Apollo program https://airandspace.si.edu/explore-and-learn/topics/apollo/apollo-program/landing-missions/apollo11-landing-site.cfm

APPENDIXES

APPENDIX 1 MATLAB CODE

Table of Computed data

Sample number µm	Mass (grams)	Height 1	Height 2 (mm)	Height 3	Average Height (mm)	Diameter 1	Diameter 2	Diameter 3	Average Diameter
38A	18.57	12.49	11.31	11.49	11.76	31.00	31.00	31.09	31.00
38B	18.65	12.47	11.40	11.25	11.70	30.90	30.70	30.80	30.80
38C	18.91	12.45	11.24	11.03	11.57	30.87	30.86	30.97	30.90
38D	18.08	12.48	11.28	11.24	11.67	31.08	31.11	31.05	31.08
106A	19.33	12.13	11.35	11.49	11.70	30.08	30.05	30.09	30.08
106B	19.41	12.48	11.46	11.25	11.65	31.01	31.02	31.01	31.01
106 C	19.24	12.07	11.45	11.03	11.51	31.00	31.01	31.06	31.01
106D	18.28	12.25	11.42	11.24	11.64	31.19	31.16	31.18	31.18
212A	19.45	12.00	11.51	11.30	11.60	30.01	30.01	30.02	30.01
212B	19.52	12.01	11.42	11.31	11.58	31.00	31.03	31.01	31.01
212 C	19.38	11.49	11.33	11.49	11.43	31.18	31.17	31.18	31.18
212D	19.35	11.50	11.32	11.50	11.44	31.00	31.07	31.00	31.00
Unsieved A	19.31	11.05	11.43	11.05	11.18	31.02	31.00	31.02	31.01
Unsieved B	19.34	12.34	11.21	11.34	11.63	31.07	31.06	31.09	31.08
Unsieved C	19.32	11.26	11.35	11.26	11.29	31.01	31.01	31.02	31.01
Unsieved D	19.27	11.25	11.41	11.25	11.30	30.08	30.11	30.05	30.80

Sample physical dimension statistics for the porosity set of different grain size

Test no µm	Load 0.2 mm(KN)	Load initial failure	Load Maximum failure (KN)	Deflection initial	Deflection 0.2mm	Deflection final(mm)
38A		0.00	61.8	0.00	0.00	1.24
38B		3.90	38.8	1.00	0.00	1.04
38C		0.00	51.0	0.00	0.00	1.02
38D		0.00	47.5	0.00	0.00	1.20
106A		4.15	44.1	1.24	0.48	1.29
106B		0.00	60.0	0.00	0.00	1.21
106 C		2.70	39.8	1.00	0.00	1.09
106D		0.00	36.4	0.00	0.00	1.24
212A			28.3	0.00	0.00	1.00
212B			25.1	0.00	0.00	1.01
212D			48.9	0.00	0.00	1.10
Unsieved A		0.00	41.9	0.00	0.00	1.23
Unsieved B		3.91	41.4	0.90	0.00	1.02
Unsieved C		0.00	30.5	0.00	0.00	1.08
Unsieved D		0.00	62.3	0.00	0.00	1.24

Table of computed data show the sample physical dimension statistics initial and maximum load failure for the porosity set of different grain size.

Test Number	Mass (grams)	Height initial	Height 0.2(mm)	Height initial Failure	Height Maximum (mm)	Load initial Failure 0.2KN	Load Maximum Failure KN	Deflection maximum
38A	18.570	12.49	11.31	11.49	11.48	0.00	61.8	1.24
38B	18.650	12.47	11.40	11.25	11.24	3.90	38.8	1.04
38C	18.913	12.45	11.24	11.33	11.29	0.00	51.0	1.02
38D	18.080	12.48	11.28	11.25	11.24	0.00	47.5	1.20
106A	19.333	12.13	12.13	11.49	11.47	4.15	44.1	1.29
106B	19.417	12.48	12.48	11.25	11.24		60.0	1.21
106 C	19.240	12.07	12.07	11.43	11.44	2.70	39.8	1.09
106D	18.283	12.25	12.25	11.24	11.22		36.4	1.24
212A	19.450	12.00	11.51	11.49	11.48	0.00	28.3	1.00
212B	19.527	12.01	11.42	11.25	11.23	0.00	25.1	1.01
212C	19.383	11.49	11.33	11.33	11.32	0.00	28.2	0.98
212D	19.350	11.50	11.32	11.24	11.21	0.00	48.9	1.10
Unsieved A	19.313	11.45	11.43	11.45	11.43	0.00	41.9	1.23
Unsieved B	19.340	12.34	11.21	11.34	11.31	3.91	41.4	1.02
Unsieved C	19.317	11.26	11.35	11.26	11.23	0.00	30.5	1.08
Unsieved D	19.273	11.25	11.41	11.25	11.24	0.00	62.3	1.24

A table of compressive strength values at maximum failure Means

Lowest Porosity 38µm		**Maximum Failure (MPa)**
	Mean	732.51
	STD	95.30
Low Porosity 106µm	Mean	614.27
	STD	126.97
Highest Porosity 212µm	Mean	496.35
	STD	108.68

Grain size µm	**Maximum diameter (mm)**	**Pressure Maximum (KPa)**	**Bulk Modulus Maximum (MPa)**
38A	31.00	81869	824.63
38B	30.80	52070	624.34
38C	30.90	68000	830.00
38D	31.08	62602	651.06
Mean			**732.51**
STD			**95.30**
106A	30.08	62049	583.45
106B	31.01	79433	819.28
106 C	31.01	52691	583.47
106D	31.18	47665	470.88
Mean			**614.27**
STD			**126.97**
212A	30.01	40004	480.05
212B	31.01	33230	395.14
212C	31.18	36928	432.96
212D	31.00	64780	677.24
Mean			**496.35**
STD			**108.68**
Unsieved A	31.01	55471	507.36
Unsieved B	31.08	54562	568.86
Unsieved C	31.01	40379	420.99
Unsieved D	30.80	83607	772.02
Mean			**567.31**
STD			**129.33**

High Porosity	Mean	567.30
unsieved	STD	129.33

APPENDIX 2 LOAD VERSUS DEFLECTION

```
# >o< ================================================================================ >o< #
# >o<                                  Adebayo Ogunyinka                               >o< #
# >o<                                  ~~~~~~~~~~~~~~~~~                               >o< #
# >o<                  Black Point-1 Simulant - compression test                       >o< #
# >o<                                  Graphical Illustrations                         >o< #
# >o<                                  ~~~~~~~~~~~~~~~~~~~~~~~                         >o< #
# >o<                                  R Code.                                         >o< #
# >o<                                  ~~~~~~~~~~~~~~~~~~~~~~~                         >o< #
# >o<                                  9 October 2018.                                 >o< #
# >o< ================================================================================ >o< #
```

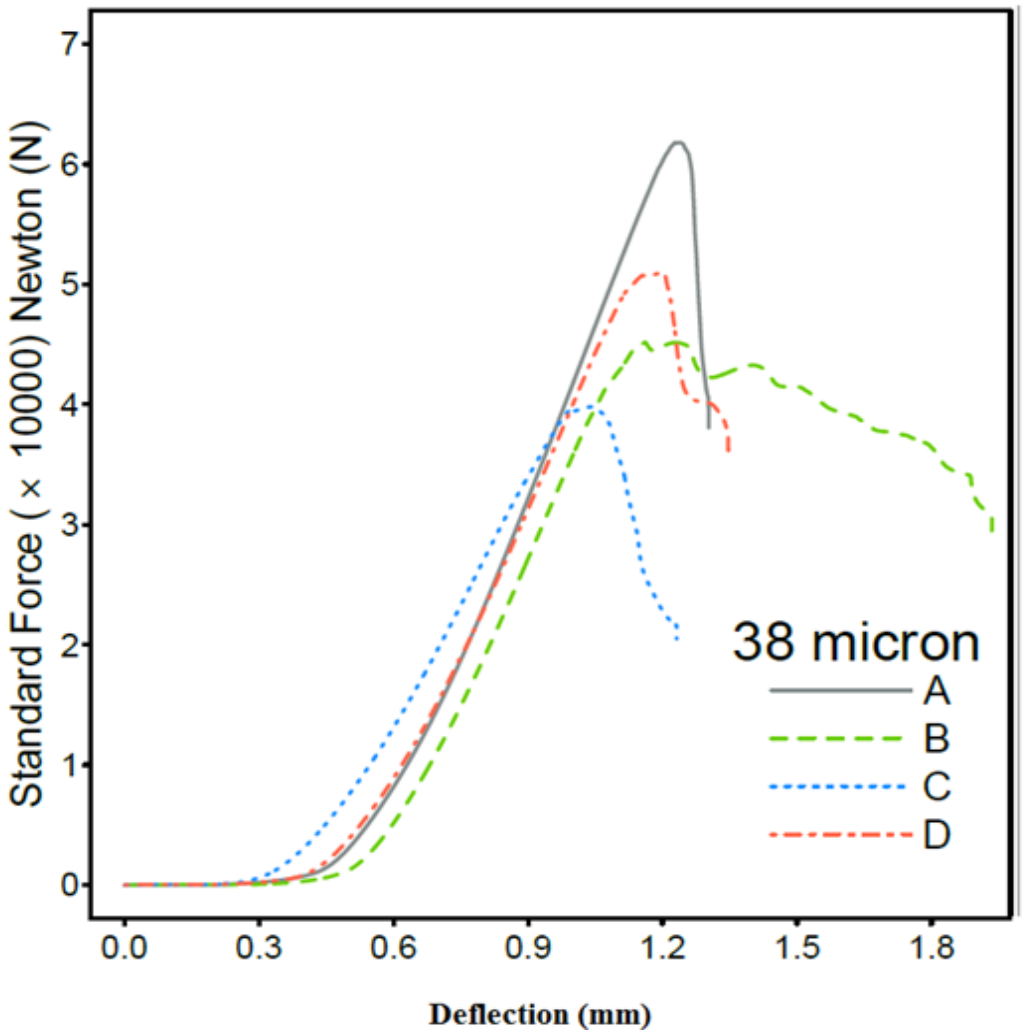

Force -deflection curve for the lowest porosity 38µm

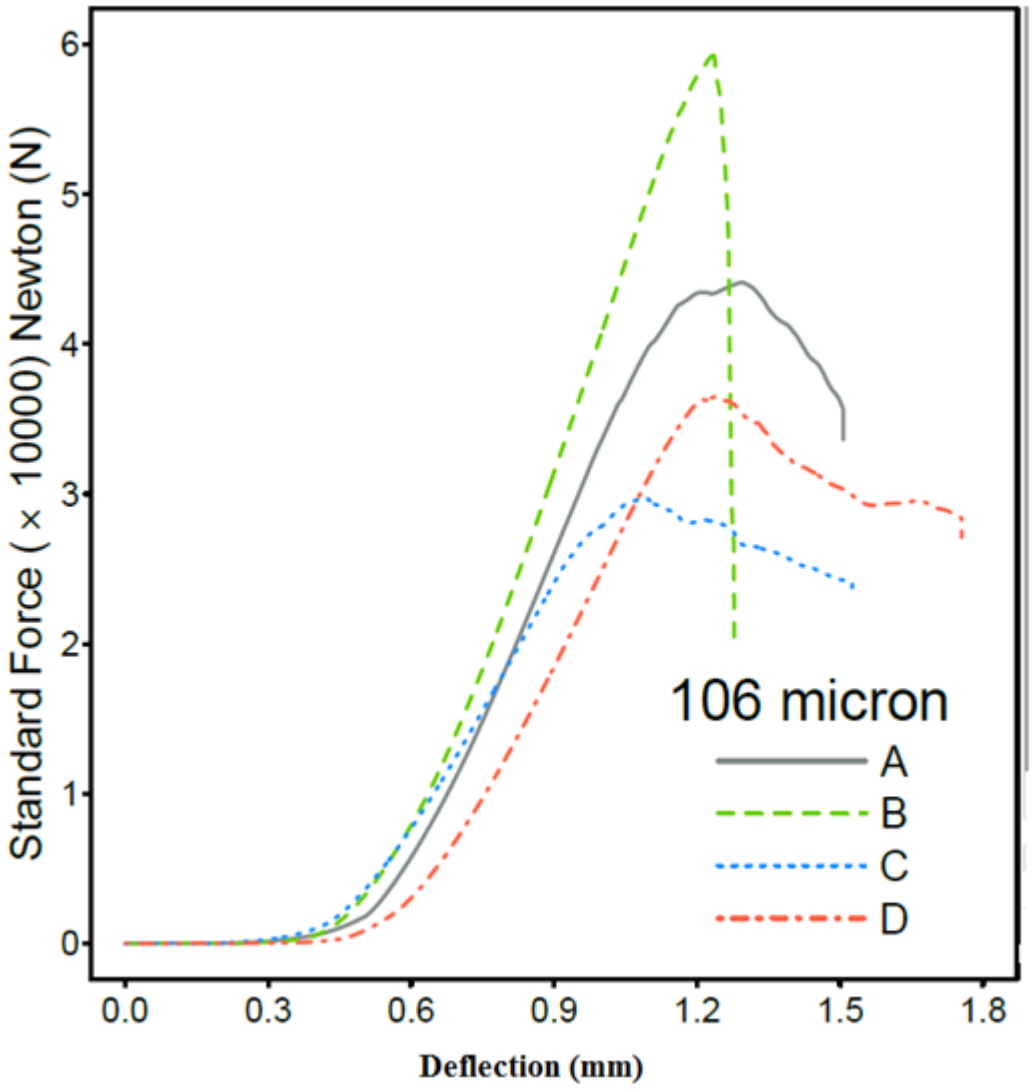

Force -deflection curve for the lower porosity106µm

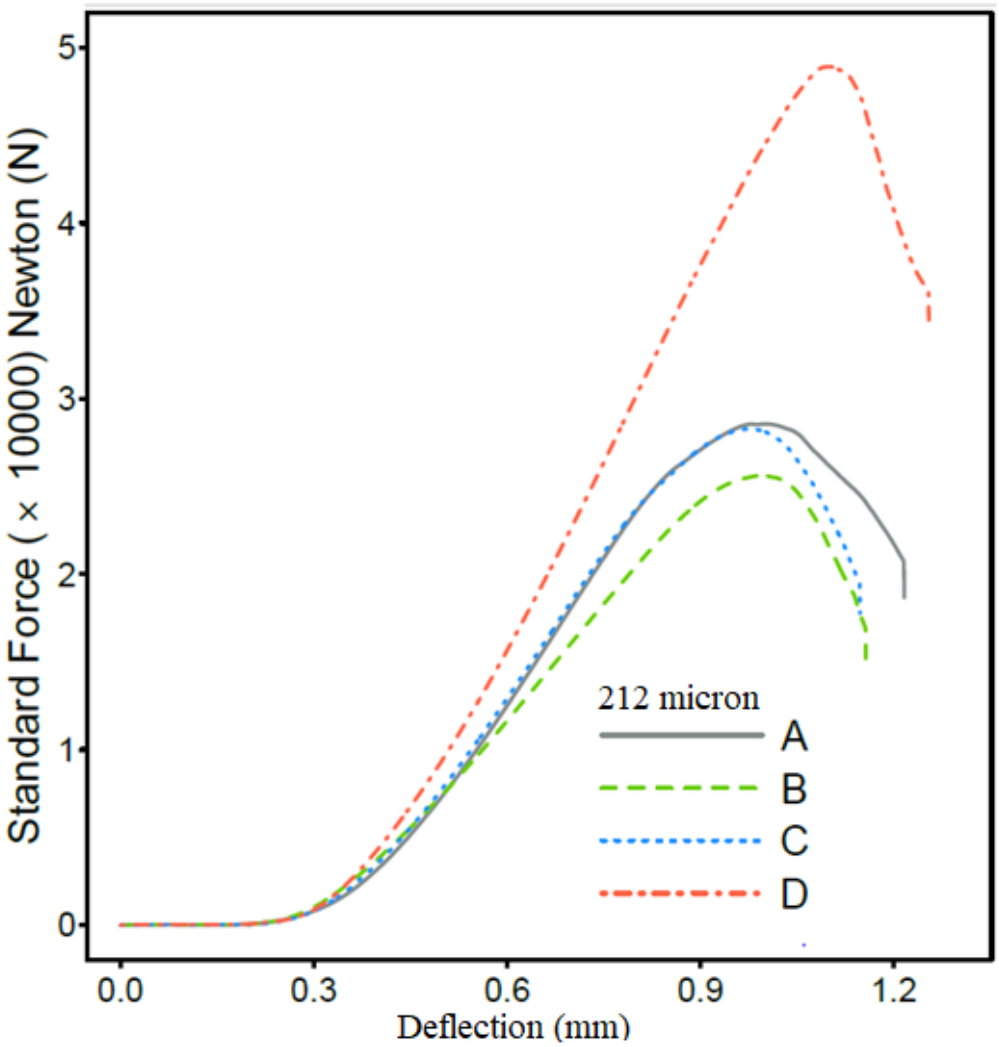

Force -deflection curve for the highest porosity 212µm

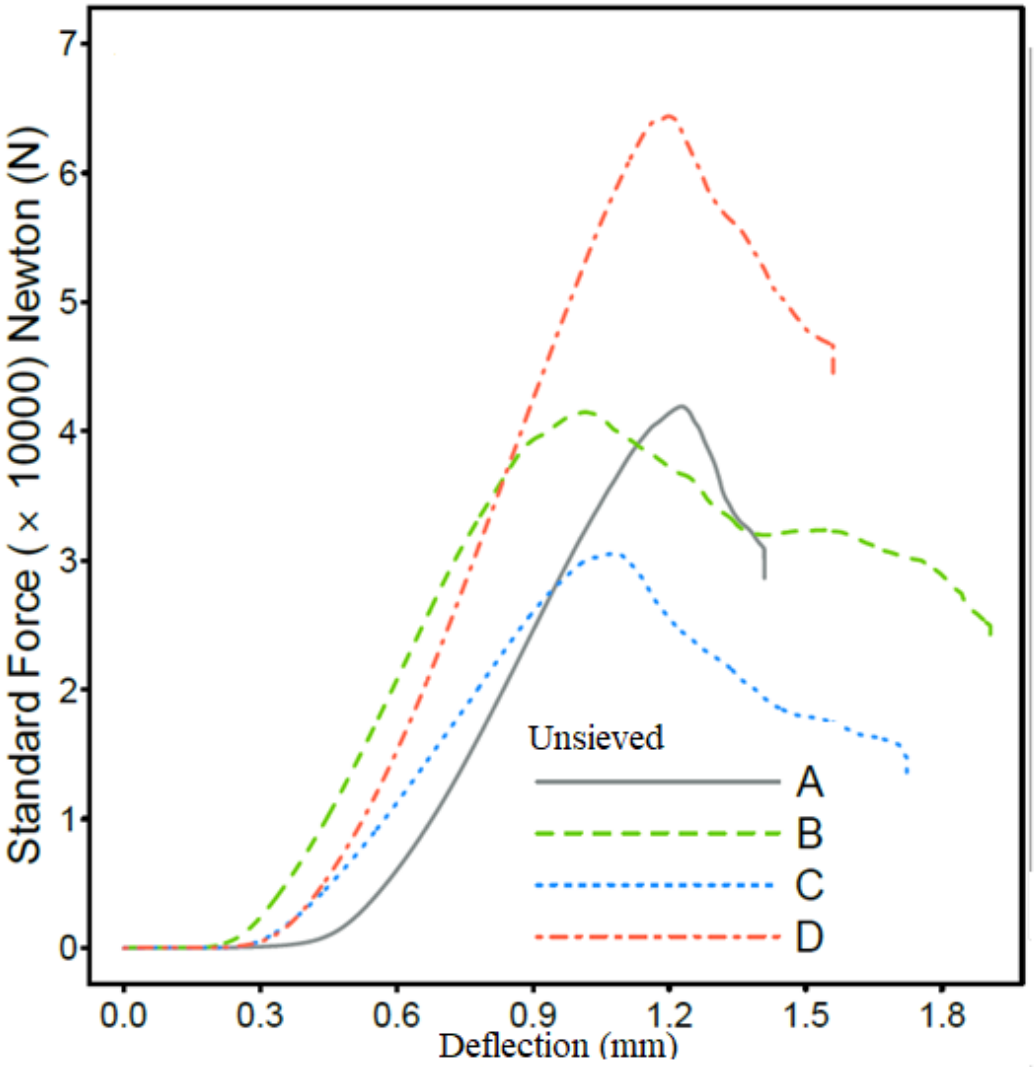

Force -deflection curve for the high porosity unsieved

APPENDIX 3 STRESS- STRAIN CURVES

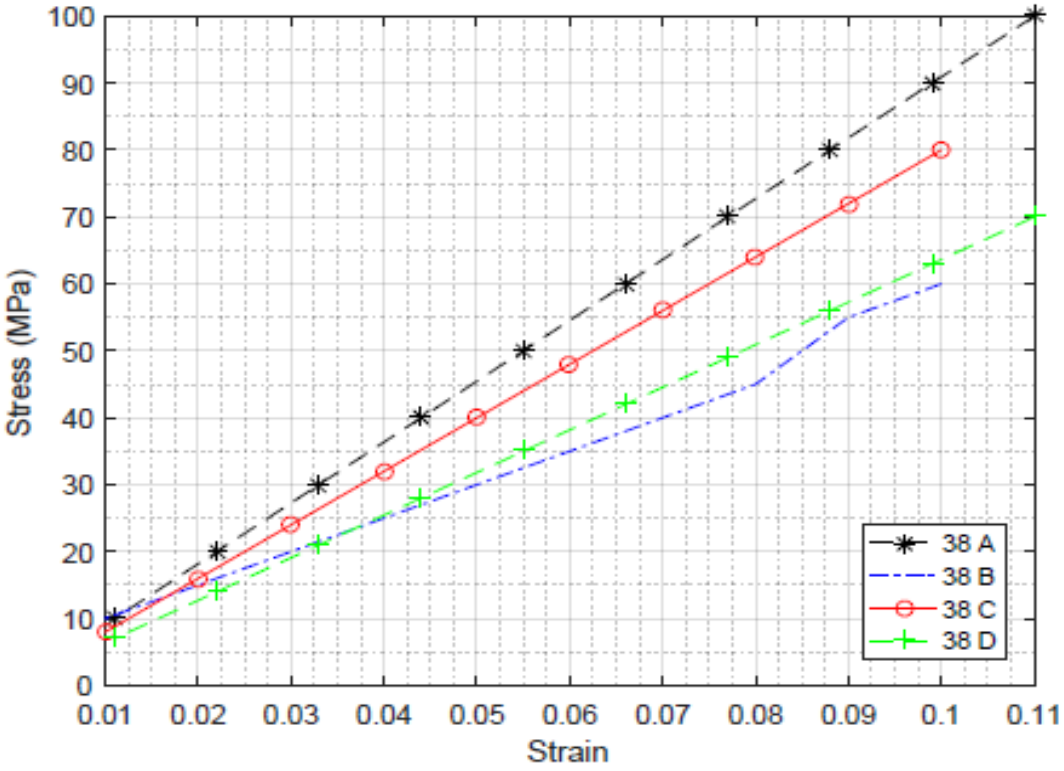

Stress -Strain graph for the lowest porosity 38µm

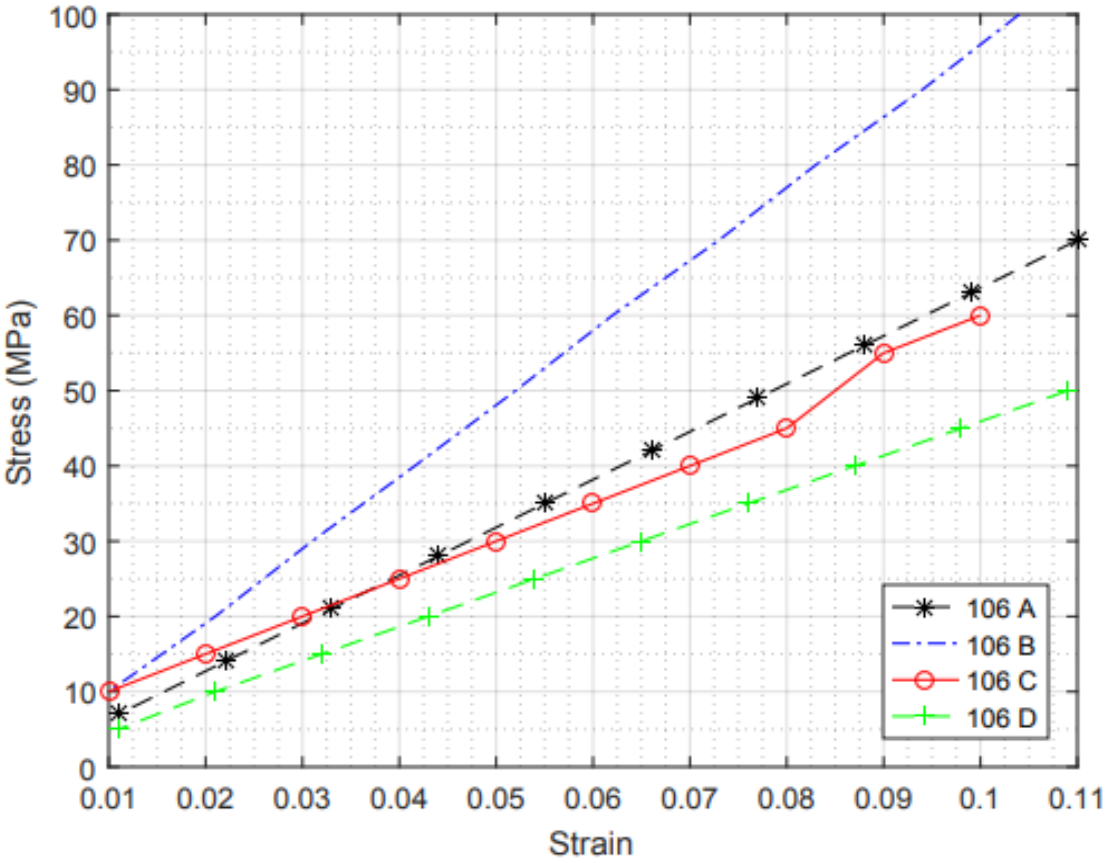

Stress -Strain graph for the lowest porosity 106µm

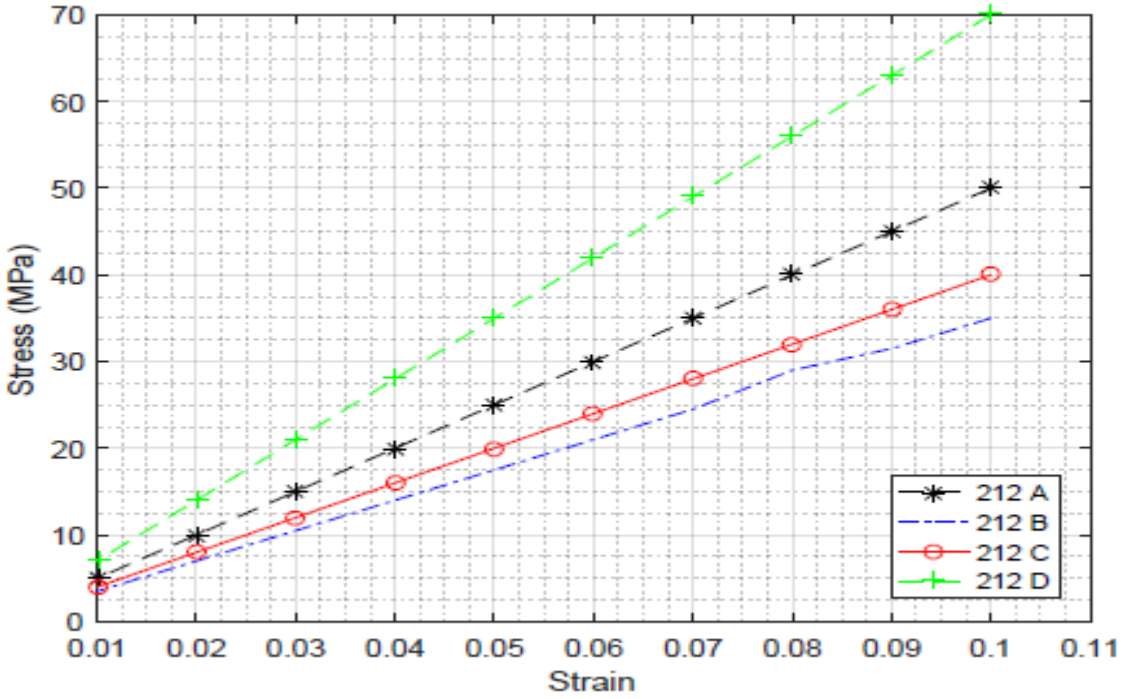

Stress -Strain graph for the high porosity 212µm.

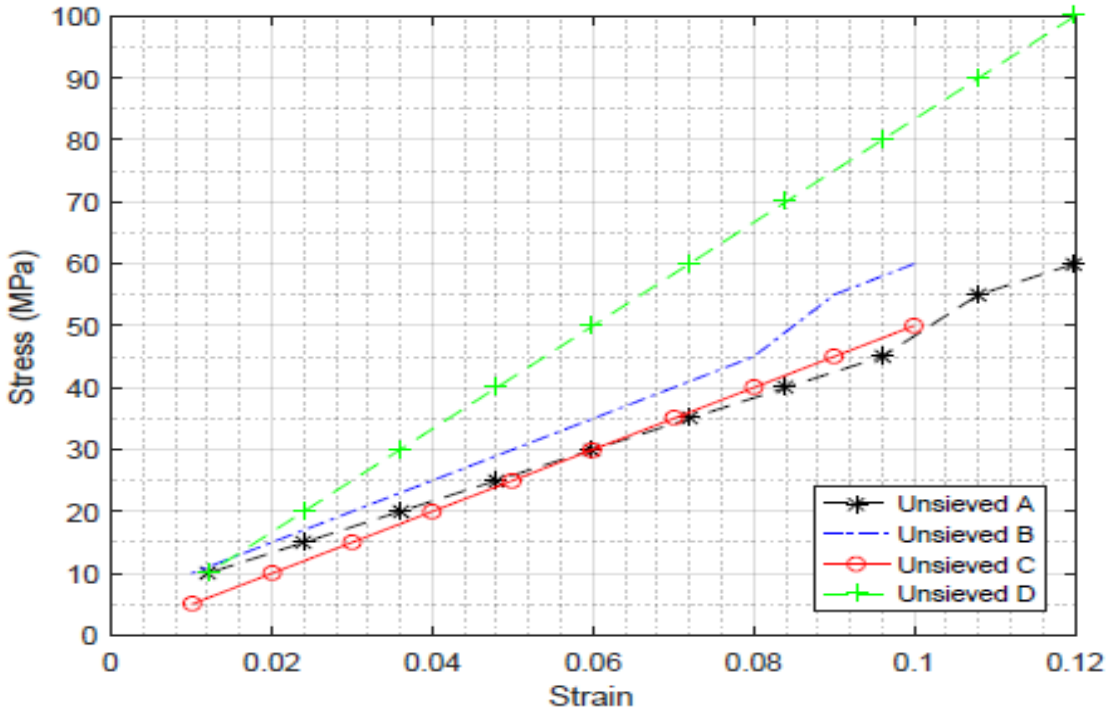

Stress -Strain graph for the high porosity unsieved

APPENDIXES

APPENDIX 4 TOUGHNESS

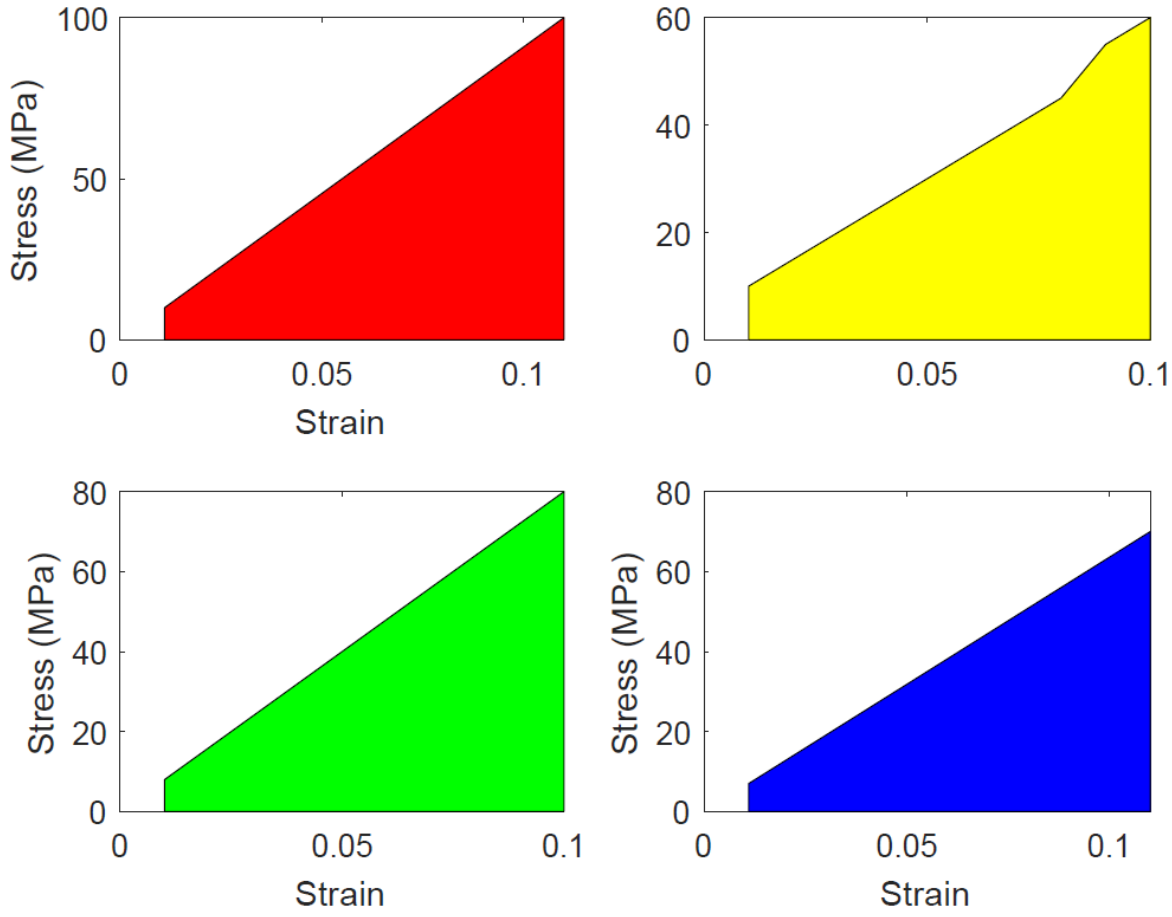

shows the area under the stress-strain 38µm curve for the lowest porosity.

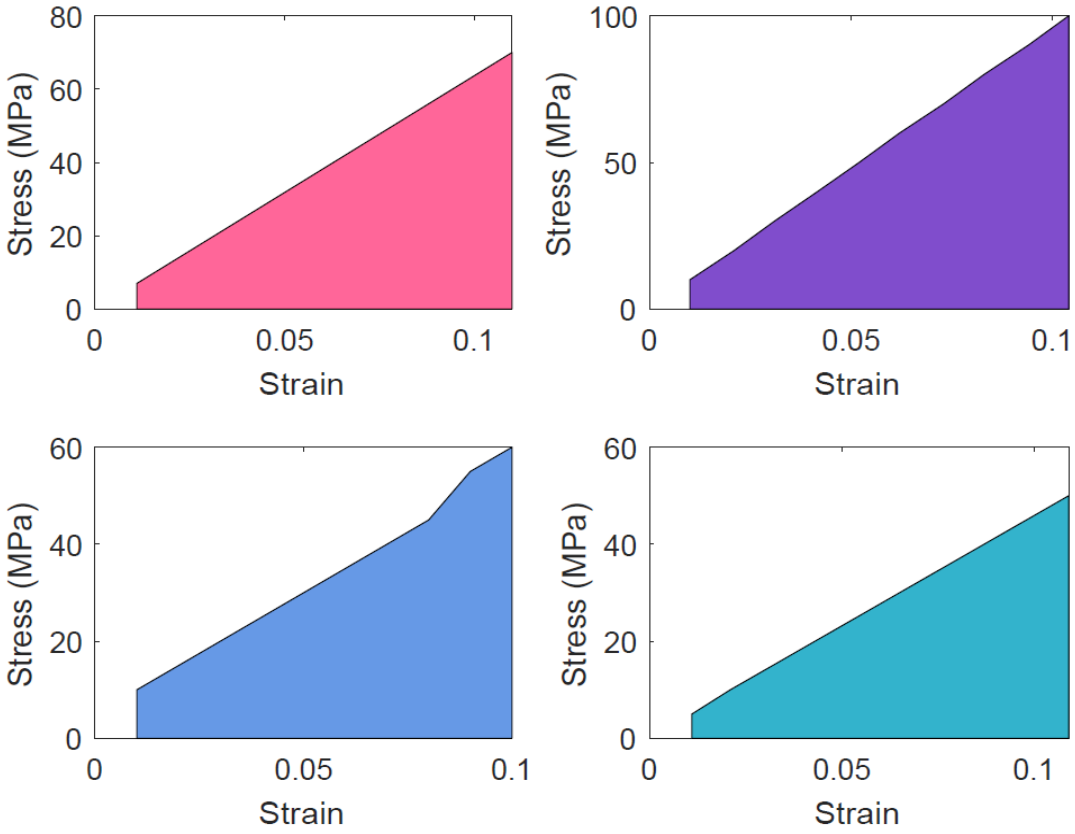

shows the area under the stress-strain curve for the low porosity 106µm

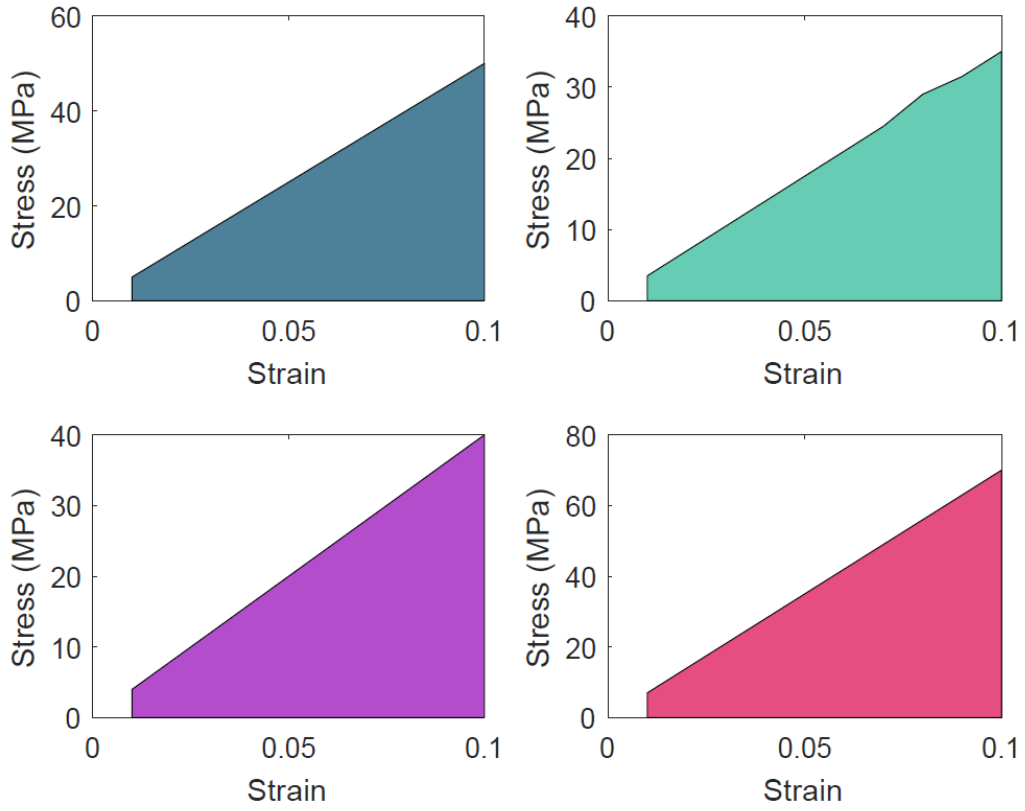

shows the area under the stress-strain curve for the largest porosity 212 µm.

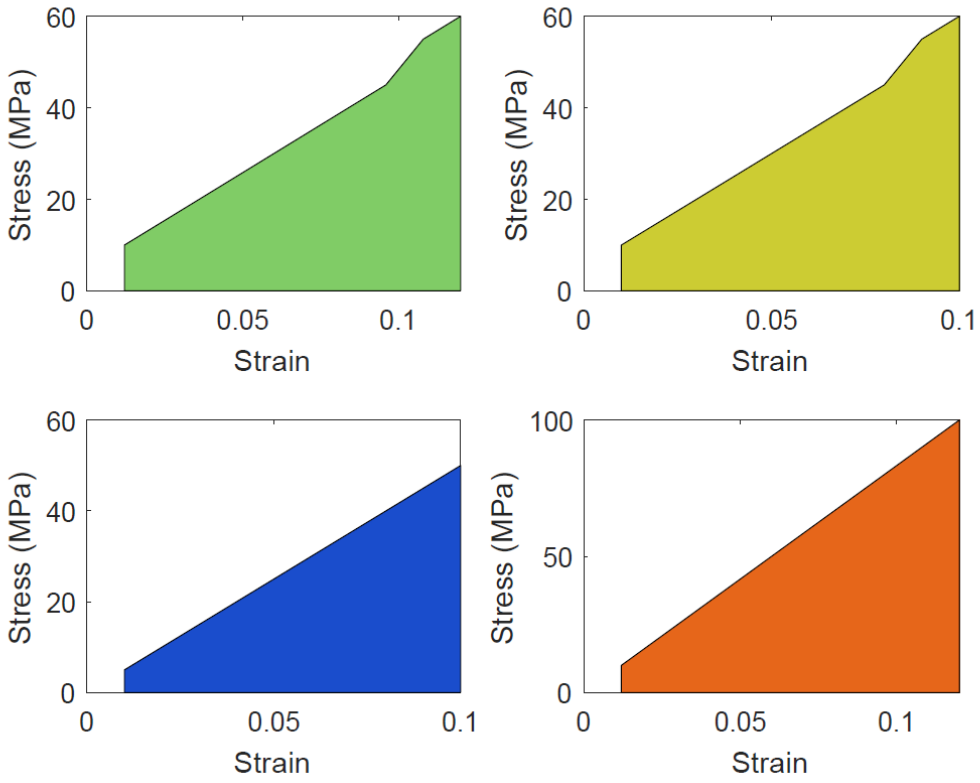

shows the area under the stress-strain curve for the high porosity unsieved

Contents

graph 38

```
figure(1)

AA = xlsread('Stress_Strain_Graph.XLS','sheet1','A2:A11');
BB = xlsread('Stress_Strain_Graph.XLS','sheet1','B2:B11');
CC = xlsread('Stress_Strain_Graph.XLS','sheet1','C2:C11');
DD = xlsread('Stress_Strain_Graph.XLS','sheet1','D2:D11');
EE = xlsread('Stress_Strain_Graph.XLS','sheet1','E2:E11');
FF = xlsread('Stress_Strain_Graph.XLS','sheet1','F2:F11');
GG = xlsread('Stress_Strain_Graph.XLS','sheet1','G2:G11');
HH = xlsread('Stress_Strain_Graph.XLS','sheet1','H2:H11');


plot(AA,BB,'k--*');
hold on
plot(CC,DD,'b-.');
```

```
hold on
plot(EE,FF,'r-o');
hold on
plot(GG,HH,'g--+');
xlabel('Strain');
ylabel('Stress (MPa)');
grid on
grid minor;
legend('38 A','38 B','38 C','38 D','Location','SouthEast');
```

graph 106

```
figure(2)

AA2 = xlsread('Stress_Strain_Graph.XLS','sheet2','A2:A11');
BB2 = xlsread('Stress_Strain_Graph.XLS','sheet2','B2:B11');
CC2 = xlsread('Stress_Strain_Graph.XLS','sheet2','C2:C11');
DD2 = xlsread('Stress_Strain_Graph.XLS','sheet2','D2:D11');
EE2 = xlsread('Stress_Strain_Graph.XLS','sheet2','E2:E11');
FF2 = xlsread('Stress_Strain_Graph.XLS','sheet2','F2:F11');
GG2 = xlsread('Stress_Strain_Graph.XLS','sheet2','G2:G11');
HH2 = xlsread('Stress_Strain_Graph.XLS','sheet2','H2:H11');


plot(AA2,BB2,'k--*');
hold on
plot(CC2,DD2,'b-.');
hold on
```

```
plot(EE2,FF2,'r-o');
hold on
plot(GG2,HH2,'g--+');
xlabel('Strain');
ylabel('Stress (MPa)');
grid on
grid minor;
legend('106 A','106 B','106 C','106 D','Location','SouthEast');
```

Graph 212

```
figure(3)



AA3 = xlsread('Stress_Strain_Graph.XLS','sheet3','A2:A11');
BB3 = xlsread('Stress_Strain_Graph.XLS','sheet3','B2:B11');
CC3 = xlsread('Stress_Strain_Graph.XLS','sheet3','C2:C11');
DD3 = xlsread('Stress_Strain_Graph.XLS','sheet3','D2:D11');
EE3 = xlsread('Stress_Strain_Graph.XLS','sheet3','E2:E11');
FF3 = xlsread('Stress_Strain_Graph.XLS','sheet3','F2:F11');
GG3 = xlsread('Stress_Strain_Graph.XLS','sheet3','G2:G11');
HH3 = xlsread('Stress_Strain_Graph.XLS','sheet3','H2:H11');


plot(AA3,BB3,'k--*');
hold on
plot(CC3,DD3,'b-.');
```

```
hold on
plot(EE3,FF3,'r-o');
hold on
plot(GG3,HH3,'g--+');
xlabel('Strain');
ylabel('Stress (MPa)');
grid on
grid minor;
legend('212 A','212 B','212 C','212 D','Location','SouthEast');
```

Graph Unsieved

```
figure (4)

AA4 = xlsread('Stress_Strain_Graph.XLS','sheet4','A2:A11');
BB4= xlsread('Stress_Strain_Graph.XLS','sheet4','B2:B11');
CC4= xlsread('Stress_Strain_Graph.XLS','sheet4','C2:C11');
DD4= xlsread('Stress_Strain_Graph.XLS','sheet4','D2:D11');
EE4= xlsread('Stress_Strain_Graph.XLS','sheet4','E2:E11');
FF4= xlsread('Stress_Strain_Graph.XLS','sheet4','F2:F11');
GG4= xlsread('Stress_Strain_Graph.XLS','sheet4','G2:G11');
HH4= xlsread('Stress_Strain_Graph.XLS','sheet4','H2:H11');


plot(AA4,BB4,'k--*');
hold on
plot(CC4,DD4,'b-.');
hold on
```

```
plot(EE4,FF4,'r-o');
hold on
plot(GG4,HH4,'g--+');
xlabel('Strain');
ylabel('Stress (MPa)');
grid on
grid minor;
legend('Unsieved A','Unsieved B','Unsieved C','Unsieved D','Location','SouthEast');
```

Linear regression for 38 _1

```
% X = 1:5;
% Y = [1 2 1.3 3.75 2.25];

%// Get total number of points
n11 = numel(AA);

% // Define relevant quantities for finding quantities
sumAAi = sum(AA);
sumBBi = sum(BB);
sumAAiBBi = sum(AA.*BB);
sumAAi2 = sum(AA.^2);
sumBBi2 = sum(BB.^2);

%// Determine slope and intercept
m11 = (sumAAi * sumBBi - n11*sumAAiBBi) / (sumAAi^2 - n11*sumAAi2);
b11 = (sumAAiBBi * sumAAi - sumBBi * sumAAi2) / (sumAAi^2 - n11*sumAAi2);
```

```
%// Display them
disp([m11 b11])
```

Linear regression for 38 _2

```
n12 = numel(CC);

% // Define relevant quantities for finding quantities
sumCCi = sum(CC);
sumDDi = sum(DD);
sumCCiDDi = sum(CC.*DD);
sumCCi2 = sum(CC.^2);
sumDDi2 = sum(DD.^2);

%// Determine slope and intercept
m12 = (sumCCi * sumDDi - n12*sumCCiDDi) / (sumCCi^2 - n12*sumCCi2);
b12 = (sumCCiDDi * sumCCi - sumDDi * sumCCi2) / (sumCCi^2 - n12*sumCCi2);

%// Display them
disp([m12 b12])
```

Linear regression for 38 _3

```
n13 = numel(EE);

% // Define relevant quantities for finding quantities
sumEEi = sum(EE);
sumFFi = sum(FF);
sumEEiFFi = sum(EE.*FF);
sumEEi2 = sum(EE.^2);
sumFFi2 = sum(FF.^2);

%// Determine slope and intercept
m13 = (sumEEi * sumFFi - n13*sumEEiFFi) / (sumEEi^2 - n13*sumEEi2);
b13 = (sumEEiFFi * sumEEi - sumFFi * sumEEi2) / (sumEEi^2 - n13*sumEEi2);

%// Display them
disp([m13 b13])
```

Linear regression for 38 _4

```
n14 = numel(GG);

% // Define relevant quantities for finding quantities
sumGGi = sum(GG);
sumHHi = sum(HH);
sumGGiHHi = sum(GG.*HH);
sumGGi2 = sum(GG.^2);
sumHHi2 = sum(HH.^2);

%// Determine slope and intercept
m14 = (sumGGi * sumHHi - n14*sumGGiHHi) / (sumGGi^2 - n14*sumGGi2);
b14 = (sumGGiHHi * sumGGi - sumHHi * sumGGi2) / (sumGGi^2 - n14*sumGGi2);

%// Display them
disp([m14 b14])
```

Linear Regression for 106 _1

X = 1:5; Y = [1 2 1.3 3.75 2.25];

```
%// Get total number of points
n21 = numel(AA2);

% // Define relevant quantities for finding quantities
sumAA2i = sum(AA2);
sumBB2i = sum(BB2);
sumAA2iBB2i = sum(AA2.*BB2);
sumAA2i2 = sum(AA2.^2);
sumBB2i2 = sum(BB2.^2);

%// Determine slope and intercept
m21 = (sumAA2i * sumBB2i - n21*sumAA2iBB2i) / (sumAA2i^2 - n21*sumAA2i2);
b21 = (sumAA2iBB2i * sumAA2i - sumBB2i * sumAA2i2) / (sumAA2i^2 - n21*sumAA2i2);

%// Display them
disp([m21 b21])
```

Linear Regression for 106 _2

```
n22 = numel(CC2);

% // Define relevant quantities for finding quantities
```

```
sumCC2i = sum(CC2);
sumDD2i = sum(DD2);
sumCC2iDD2i = sum(CC2.*DD2);
sumCC2i2 = sum(CC2.^2);
sumDD2i2 = sum(DD2.^2);

%// Determine slope and intercept
m22 = (sumCC2i * sumDD2i - n22*sumCC2iDD2i) / (sumCC2i^2 - n22*sumCC2i2);
b22 = (sumCC2iDD2i * sumCC2i - sumDD2i * sumCC2i2) / (sumCC2i^2 - n22*sumCC2i2);

%// Display them
disp([m22 b22])
```

Linear Regression for 106 _3

```
n23 = numel(EE2);

% // Define relevant quantities for finding quantities
sumEE2i = sum(EE2);
sumFF2i = sum(FF2);
sumEE2iFF2i = sum(EE2.*FF2);
sumEE2i2 = sum(EE2.^2);
sumFF2i2 = sum(FF2.^2);

%// Determine slope and intercept
m23 = (sumEE2i * sumFF2i - n23*sumEE2iFF2i) / (sumEE2i^2 - n23*sumEE2i2);
b23 = (sumEE2iFF2i * sumEE2i - sumFF2i * sumEE2i2) / (sumEE2i^2 - n23*sumEE2i2);

%// Display them
disp([m23 b23])
```

Linear Regression for 106 _4

```
n24 = numel(GG2);

% // Define relevant quantities for finding quantities
sumGG2i = sum(GG2);
sumHH2i = sum(HH2);
sumGG2iHH2i = sum(GG2.*HH2);
sumGG2i2 = sum(GG2.^2);
sumHH2i2 = sum(HH2.^2);

%// Determine slope and intercept
m24 = (sumGG2i * sumHH2i - n24*sumGG2iHH2i) / (sumGG2i^2 - n24*sumGG2i2);
b24 = (sumGG2iHH2i * sumGG2i - sumHH2i * sumGG2i2) / (sumGG2i^2 - n24*sumGG2i2);
```

```
%// Display them
disp([m24 b24])
```

Linear Regression for 212 _1

X = 1:5; Y = [1 2 1.3 3.75 2.25];

```
%// Get total number of points
n31 = numel(AA3);

% // Define relevant quantities for finding quantities
sumAA3i = sum(AA3);
sumBB3i = sum(BB3);
sumAA3iBB3i = sum(AA3.*BB3);
sumAA3i2 = sum(AA3.^2);
sumBB3i2 = sum(BB3.^2);

%// Determine slope and intercept
m31 = (sumAA3i * sumBB3i - n31*sumAA3iBB3i) / (sumAA3i^2 - n31*sumAA3i2);
b31 = (sumAA3iBB3i * sumAA3i - sumBB3i * sumAA3i2) / (sumAA3i^2 - n31*sumAA3i2);

%// Display them
disp([m31 b31])
```

%% Linear Regression for 212 _2

```
n32 = numel(CC3);

% // Define relevant quantities for finding quantities
sumCC3i = sum(CC3);
sumDD3i = sum(DD3);
sumCC3iDD3i = sum(CC3.*DD3);
sumCC3i2 = sum(CC3.^2);
sumDD3i2 = sum(DD3.^2);

%// Determine slope and intercept
m32 = (sumCC3i * sumDD3i - n32*sumCC3iDD3i) / (sumCC3i^2 - n32*sumCC3i2);
b32 = (sumCC3iDD3i * sumCC3i - sumDD3i * sumCC3i2) / (sumCC3i^2 - n32*sumCC3i2);

%// Display them
disp([m32 b32])
```

Linear Regression for 212 _3

```
n33 = numel(EE3);

% // Define relevant quantities for finding quantities
sumEE3i = sum(EE3);
sumFF3i = sum(FF3);
sumEE3iFF3i = sum(EE3.*FF3);
sumEE3i2 = sum(EE3.^2);
sumFF3i2 = sum(FF3.^2);

%// Determine slope and intercept
m33 = (sumEE3i * sumFF3i - n33*sumEE3iFF3i) / (sumEE3i^2 - n33*sumEE3i2);
b33 = (sumEE3iFF3i * sumEE3i - sumFF3i * sumEE3i2) / (sumEE3i^2 - n33*sumEE3i2);

%// Display them
disp([m33 b33])
```

Linear Regression for 212 _4

```
n34 = numel(GG3);

% // Define relevant quantities for finding quantities
sumGG3i = sum(GG3);
sumHH3i = sum(HH3);
sumGG3iHH3i = sum(GG3.*HH3);
sumGG3i2 = sum(GG3.^2);
sumHH3i2 = sum(HH3.^2);

%// Determine slope and intercept
m34 = (sumGG3i * sumHH3i - n34*sumGG3iHH3i) / (sumGG3i^2 - n34*sumGG3i2);
b34 = (sumGG3iHH3i * sumGG3i - sumHH3i * sumGG3i2) / (sumGG3i^2 - n34*sumGG3i2);

%// Display them
disp([m34 b34])
```

Linear regression for Unsieved _1

```
% X = 1:5;
% Y = [1 2 1.3 3.75 2.25];
```

```
%// Get total number of points
n41 = numel(AA4);

% // Define relevant quantities for finding quantities
sumAA4i = sum(AA4);
sumBB4i = sum(BB4);
sumAA4iBB4i = sum(AA4.*BB4);
sumAA4i2 = sum(AA4.^2);
sumBB4i2 = sum(BB4.^2);

%// Determine slope and intercept
m41 = (sumAA4i * sumBB4i - n41*sumAA4iBB4i) / (sumAA4i^2 - n41*sumAA4i2);
b41 = (sumAA4iBB4i * sumAA4i - sumBB4i * sumAA4i2) / (sumAA4i^2 - n41*sumAA4i2);

%// Display them
disp([m41 b41])
```

Linear regression for Unsieved_2

```
n42 = numel(CC4);

% // Define relevant quantities for finding quantities
sumCC4i = sum(CC4);
sumDD4i = sum(DD4);
sumCC4iDD4i = sum(CC4.*DD4);
sumCC4i2 = sum(CC4.^2);
sumDD4i2 = sum(DD4.^2);

%// Determine slope and intercept
m42 = (sumCC4i * sumDD4i - n42*sumCC4iDD4i) / (sumCC4i^2 - n42*sumCC4i2);
b42 = (sumCC4iDD4i * sumCC4i - sumDD4i * sumCC4i2) / (sumCC4i^2 - n42*sumCC4i2);

%// Display them
disp([m42 b42])
```

Linear regression for Unsieved_3

```
n43 = numel(EE4);

% // Define relevant quantities for finding quantities
sumEE4i = sum(EE4);
sumFF4i = sum(FF4);
sumEE4iFF4i = sum(EE4.*FF4);
sumEE4i2 = sum(EE4.^2);
```

```
sumFF4i2 = sum(FF4.^2);

%// Determine slope and intercept
m43 = (sumEE4i * sumFF4i - n43*sumEE4iFF4i) / (sumEE4i^2 - n43*sumEE4i2);
b43 = (sumEE4iFF4i * sumEE4i - sumFF4i * sumEE4i2) / (sumEE4i^2 - n43*sumEE4i2);

%// Display them
disp([m43 b43])
```

Linear regression for Unsieved _4

```
n44 = numel(GG4);

% // Define relevant quantities for finding quantities
sumGG4i = sum(GG4);
sumHH4i = sum(HH4);
sumGG4iHH4i = sum(GG4.*HH4);
sumGG4i2 = sum(GG4.^2);
sumHH4i2 = sum(HH4.^2);

%// Determine slope and intercept
m44 = (sumGG4i * sumHH4i - n44*sumGG4iHH4i) / (sumGG4i^2 - n44*sumGG4i2);
b44 = (sumGG4iHH4i * sumGG4i - sumHH4i * sumGG4i2) / (sumGG4i^2 - n44*sumGG4i2);

%// Display them
disp([m44 b44])
```

Calculating Toughness of the Samples -38

```
figure(5)

subplot(2,2,1);
area(AA,BB,'Facecolor','r');
xlim([0,max(AA)]);
xlabel('Strain');
ylabel('Stress (MPa)');
subplot(2,2,2);
area(CC,DD,'Facecolor','y');
xlim([0,max(CC)]);

subplot(2,2,3);
area(EE,FF,'Facecolor','g');
xlim([0,max(EE)]);
xlabel('Strain');
ylabel('Stress (MPa)');
```

```
xlabel('Strain');
ylabel('Stress (MPa)');

subplot(2,2,4);
area(GG,HH,'Facecolor','b');
xlim([0,max(GG)])
xlabel('Strain');
ylabel('Stress (MPa)');
```

Calculating Toughness of the Samples -106

```
figure (6)

subplot(2,2,1);
area(AA2,BB2,'Facecolor',[1 0.4 0.6]);
xlim([0,max(AA2)]);
xlabel('Strain');
ylabel('Stress (MPa)');

subplot(2,2,2);
area(CC2,DD2,'Facecolor',[0.5 0.3 0.8]);
xlim([0,max(CC2)]);
xlabel('Strain');
ylabel('Stress (MPa)');


subplot(2,2,3);
area(EE2,FF2,'Facecolor',[0.4 0.6 0.9]);
```

```
xlim([0,max(EE2)]);
xlabel('Strain');
ylabel('Stress (MPa)');
xlabel('Strain');
ylabel('Stress (MPa)');

subplot(2,2,4);
area(GG2,HH2,'Facecolor',[0.2 0.7 0.8]);
xlim([0,max(GG2)])
xlabel('Strain');
ylabel('Stress (MPa)');
```

% Calculating Toughness of the Samples -212

```
 figure(7)
subplot(2,2,1);
area(AA3,BB3,'Facecolor',[0.3 0.5 0.6]);
xlim([0,max(AA3)]);
xlabel('Strain');
ylabel('Stress (MPa)');

subplot(2,2,2);
area(CC3,DD3,'Facecolor',[0.4 0.8 0.7]);
xlim([0,max(CC3)]);
xlabel('Strain');
ylabel('Stress (MPa)');
```

```
subplot(2,2,3);
area(EE3,FF3,'Facecolor',[0.7 0.3 0.8]);
xlim([0,max(EE3)]);
xlabel('Strain');
ylabel('Stress (MPa)');
xlabel('Strain');
ylabel('Stress (MPa)');

subplot(2,2,4);
area(GG3,HH3,'Facecolor',[0.9 0.3 0.5]);
xlim([0,max(GG3)])
xlabel('Strain');
ylabel('Stress (MPa)');
```

%% Calculating Toughness of the Samples - Unsieved

```
figure (8)

subplot(2,2,1);
area(AA4,BB4,'Facecolor',[0.5 0.8 0.4]);
xlim([0,max(AA4)]);
xlabel('Strain');
ylabel('Stress (MPa)');

subplot(2,2,2);
area(CC4,DD4,'Facecolor',[0.8 0.8 0.2]);
xlim([0,max(CC4)]);
xlabel('Strain');
```

```
ylabel('Stress (MPa)');


subplot(2,2,3);
area(EE4,FF4,'Facecolor',[0.1 0.3 0.8]);
xlim([0,max(EE4)]);
xlabel('Strain');
ylabel('Stress (MPa)');
xlabel('Strain');
ylabel('Stress (MPa)');

subplot(2,2,4);
area(GG4,HH4,'Facecolor',[0.9 0.4 0.1]);
xlim([0,max(GG4)])
xlabel('Strain');
ylabel('Stress (MPa)');
```

Toughness

```
Toughness = zeros(4,4);
Toughness(1,1)=trapz(sort(BB),sort(AA));
Toughness(1,2)=trapz(sort(CC),sort(DD));
Toughness(1,3)=trapz(sort(EE),sort(FF));
Toughness(1,4)=trapz(sort(GG),sort(HH));

Toughness(2,1)=trapz(sort(AA2),sort(BB2));
Toughness(2,2)=trapz(sort(CC2),sort(DD2));
Toughness(2,3)=trapz(sort(EE2),sort(FF2));
```

```
Toughness(2,4)=trapz(sort(GG2),sort(HH2));

Toughness(3,1)=trapz(sort(AA3),sort(BB3));
Toughness(3,2)=trapz(sort(CC3),sort(DD3));
Toughness(3,3)=trapz(sort(EE3),sort(FF3));
Toughness(3,4)=trapz(sort(GG3),sort(HH3));

Toughness(4,1)=trapz(sort(AA4),sort(BB4));
Toughness(4,2)=trapz(sort(CC4),sort(DD4));
Toughness(4,3)=trapz(sort(EE4),sort(FF4));
Toughness(4,4)=trapz(sort(GG4),sort(HH4));

%disp('Toughness is =',Toughness);
Toughness
```